Light

As You Have Never

Seen It Before

The STEM Approach
Volume 3

by

David L Johnson

Table of Contents

February 2025

Introduction

Snell's Law, developed around 1600, provided the equations that link the angles of incidence and refraction to the refractive index of transparent media. The **Fresnel equations**, which describe the s- and p-polarisation ratios of refracted and reflected light, were developed in the 1820's, but it wasn't until the development of **Maxwell's Equations** in the 1860's that the electromagnetic characteristics of light became well defined.

From the earliest studies of light, there has been a debate as to whether light rays consist of corpuscles (particles) or waves and, by 1900, the wave argument was winning. However, when in the early 1900's, Albert Einstein attributed the **photoelectric effect** to light particles that represent a fixed quantum of energy, later to be called **photons**, the particle side of the wave-particle debate was re-invigorated.

Present day **Conventional Science** (**CS**) generally acknowledges that EMR consists of **photons**, but debate has continued as to whether photons are particles or have a wave-like form. Photons appear to act as a particle when considering their interaction with other material (i.e. photoelectron emission from metal, electron scattering etc.), whereas they appear to act wave-like in terms of propagation, refraction and interference. EMR, encompassing visible light, is considered to have **wave–particle duality**, with photons conveniently considered particles in some situations, and as electromagnetic wave in others; and with the wave equations of Quantum Mechanics supporting such duality.

Electromagnetic Radiation (**EMR**) presents as synchronized sinusoidal oscillations of electric and magnetic fields that travel in a vacuum at a speed of 300,000,000 metres/second (rounded). The EMR spectrum covers wavelengths that range from less than 0.1 angstrom for Gamma rays to more than 1 km for radio waves, encompassing the wavelengths of visible light in the (approximate) range of 400 nm (violet) to 700 nm (red). A graphic of the full EMR spectrum in terms of wavelength and frequency can be found using this link.

Phenomena such as the photoelectric effect and electron scattering indicate that EMR can impart kinetic energy. Thus, although they are often considered massless, photons must have at least a mass equivalence, but currently very little is known about the exact nature of photons. The term 'photon' implies a quantity (or quantum) of EMR that carries energy proportional to the frequency of the EMR but, although a conceptually convenient and useful term when discussing EMR, the photon concept remains a nebulous entity.

It is fair to say that typical explanations of EMR emission are complicated, confused and confusing. In simplistic terms, the **Orbit Nuclear Atomic Model** (ONAM) approach contends that EMR emission is produced by excited orbital electrons jumping to a lower orbit; and absorbing energy by jumping back out again: the frequency and energy of the emitted EMR dependent upon the energy difference between fixed orbitals. However, there is no explanation of how the energy associated with an electron's inward jump translates into EMR; or vice versa for EMR absorption.

Another problem is the reason why, in an energised environment, electrons would suddenly jump to a lower orbit, so emitting EMR: it would seem more likely that the electrons would simply get kinetically excited and move to a higher energy orbit and stay there; or leave the atom completely (as does happen), so ionising the atom in the process.

The STEM approach provides some alternative explanations and answers for EMR emission and absorption. But first, as a warmup primer, the next chapter will overview the topic of manmade micro and radio waves: a more complete coverage of this topic can be found in the STEM Volume 1: Electricity and the Duplicit Electron paper.

This paper is Volume 3 of a three volume series related to STEM (Spin Torus Energy Model). Volume 1 addresses Electricity and the Duplicit Electron, and Volume 2 Atomic Structure. This volume develops a **physical model** for electromagnetic radiation (**EMR**) and applies it to provide detailed explanations for light-related behaviour (reflection, refraction and the photoelectric effect), the various light forms (plane, circularly and elliptically polarised light, and optic vortex light), and addresses the differences between photonic and non-photonic EMR.

The original version of this paper, 'The STEM Approach Volume 3: The Nature of Light Based Upon a Physical Model for EMR' has been substantially re-written and, because it represents a major re-write, has been renamed.

In many ways the simplicity, completeness and consistency of the STEM explanation of EMR, and of light in particular, is an endorsement of STEM's approach to atomic structure, electromagnetic fields, the electron and electricity, as addresses in the STEM Volume 1 and 2 papers, because it brings all these aspects together. Let there be light.

Micro and Radio Waves

Micro and radio waves have frequencies less than 300 GHz corresponding to wavelengths from 1 millimetre upwards. Radio and micro waves can be manmade or result from natural sources (mainly from Space). Manmade micro and radio waves are generated by circuitry consisting of a tuneable capacitor and inductor loop circuit (i.e. an LC circuit), that delivers a high-frequency AC waveform (a 'pure capacitance' waveform) in the radio/micro wave frequency range. Circuitry can also be provided to produce a range of frequency encodings, which can be fed to a transmitter antenna to generate radio/micro wave signals.

In order to understand how manmade **micro and radio waves** (which, henceforth in this chapter, will simply be referred to as '**radio waves**') are generated, it is necessary to understand the nature and composition of an electric field.

An electric field is depicted **by electric field lines** (or electric **lines of force**) which, by convention, show field lines originating from a monopole positive charge and inwards towards a monopole negative charge such as in figure 1b. Positive and negative charges attract, with the electric field lines connecting as in shown in figure 1a.
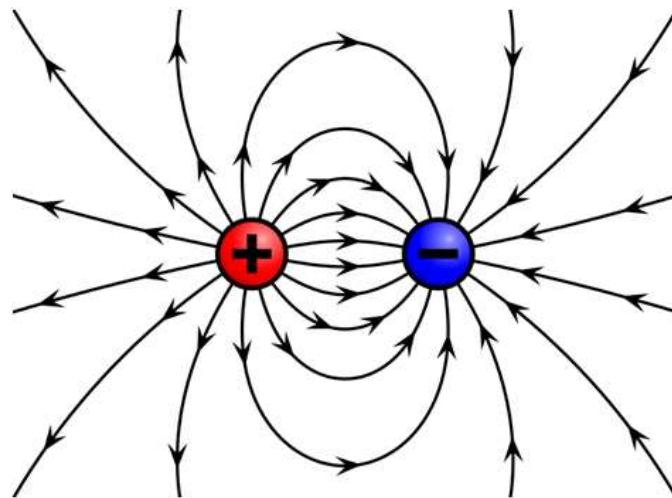

Figure 1a: Conventional Electric Field Lines (attraction)

Should a pair of metal **probes** is attached to the opposite terminals of a DC power source, they approximate a pair of positive and a negative monopole electric charges. The electric field causes attraction between the probes, which is particularly noticeable when they are brought quite close together. Figure 1c shows the STEM representation of the electric field generated between the probe tips.
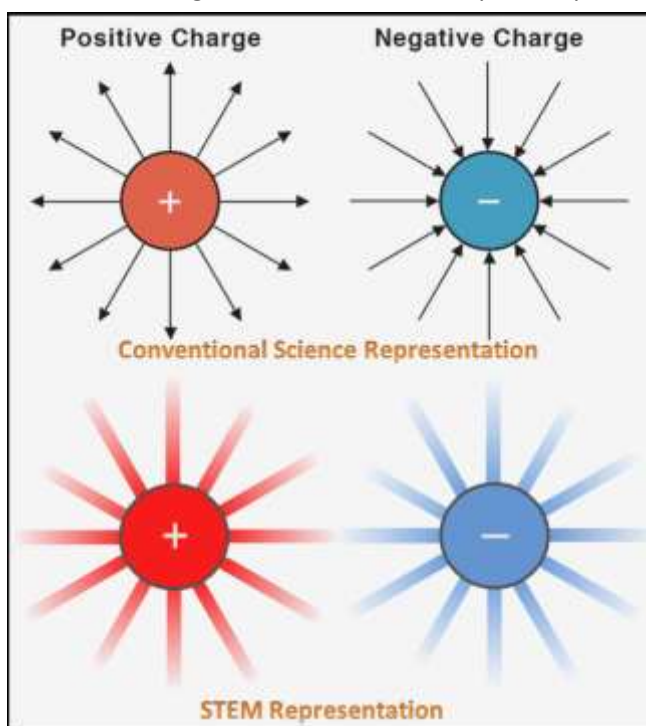

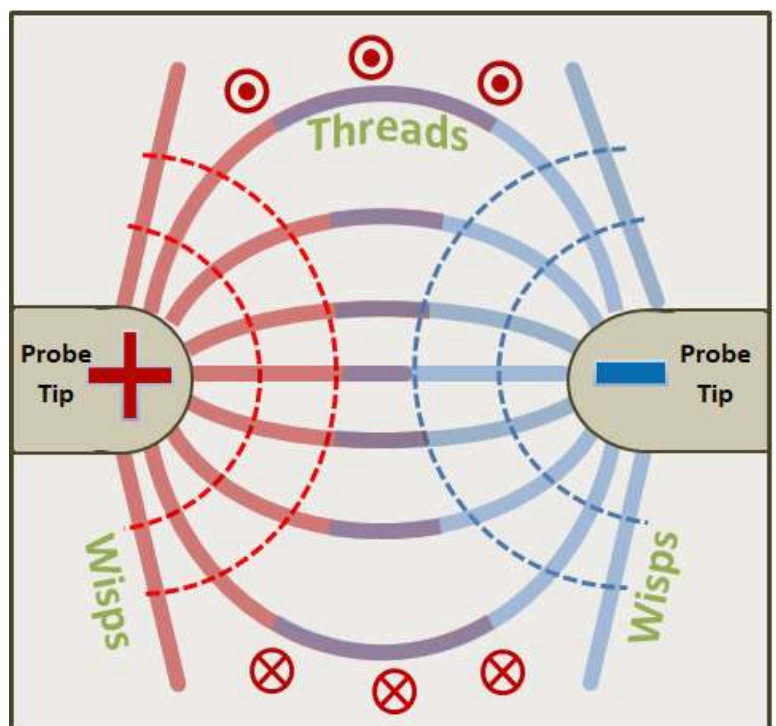*Figure 1b: Monopole Charge Electric Field Lines*

Figure 1c: STEM Electric Charge across Probe Tips

There are two main differences between the CS and STEM representations. Firstly, with the STEM approach there is no net flow of field energy between a pair of electric charges, as indicated by there being no directional arrows associated with the field lines in figure 1c. Secondly, with the STEM approach there is a circular flow of field-energy around each field line, the net effect of which is a mild **circular magnetic field** around the gap between the probe-tips: the arrowheads indicate a flow out of the page, and the arrow-quills a flow into the page.

The electric field associated with electric charge consists of **energen** (see the STEM Volume 1: Electricity and the Duplicit Electron paper for more detail). STEM introduces two new terms related to electric field lines: **threads** and **wisps**. Wisps represent the energen-based electric field from emanating from an electric charge, shown as red from a positive charge and blue from a negative charge as in figure 1b. Threads are somewhat similar to CS's field lines of force, but represent the locus of the tangents to the electric field's circular magnetic field.

 A **dipole antenna** is commonly used to generate radio waves. It consists of two vertical metal feeder rods (as shown in figure 1d) connected to a high frequency AC circuit that reverses the polarity of their electric poles on each cycle.
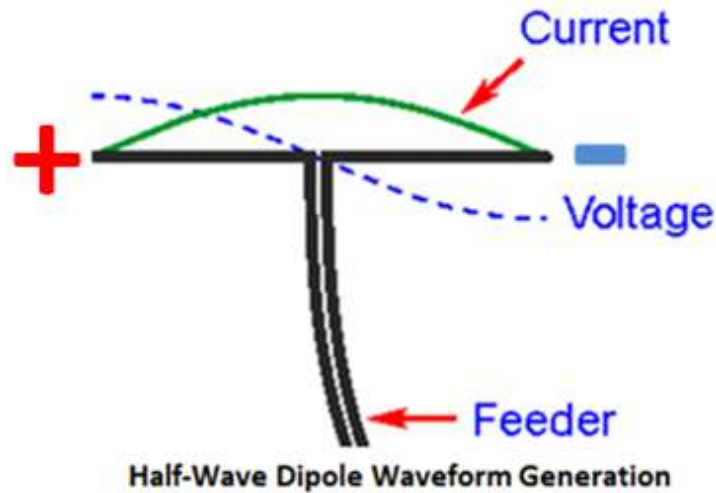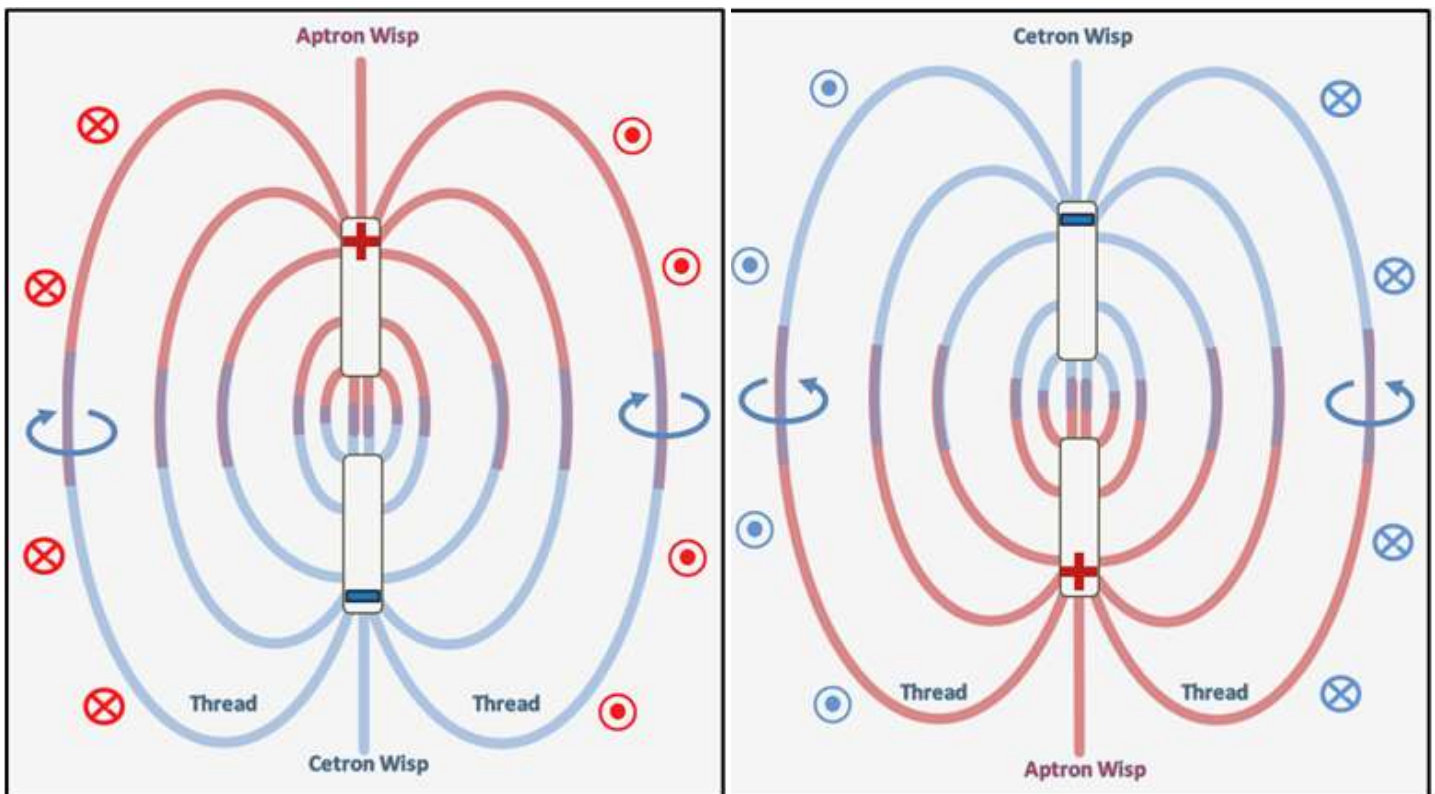

Figure 1d: Half Dipole Antenna Current-Voltage Profiles

Note that in figures 2a and 2b, the poles of a dipole antenna face away from each other whereas, to demonstrate electric charge attraction, oppositely charged electric poles are placed to face each other in close proximity as in figures 1c. This is significant, because many threads connecting the poles are stretched across the entire outer extent of the antenna rods, with a toroidal-shaped circular magnetic field moving around the antenna.


Figure 2: Electric Field Patterns Generated by a Dipole Antenna

When the uppermost pole of a dipole antenna becomes positive, an electric field forms with its circular magnetic field being represented by the threads and wisps as shown in figure 2a. Upon pole reversal by the next AC cycle, the electric field is reversed as indicated by a reversal of the circular magnetic field direction in figure 2b.

Figure 3 has screen shots of this excellent Wikipedia animated gif, which is a simulation of an oscillating **hypothetical electric dipole antenna**, assuming that the antenna impedance is well matched to that of the AC source. The central electric field (red) of figure 3a corresponds to that of figure 2a. When the electric field is suddenly reversed (to the figure 2b polarity), the concentration of 'old' field-energy (red) detaches, with the 'new' electric field (blue) rapidly and unceremoniously pushing it outwards and away from the dipole, as shown in figure 3b.
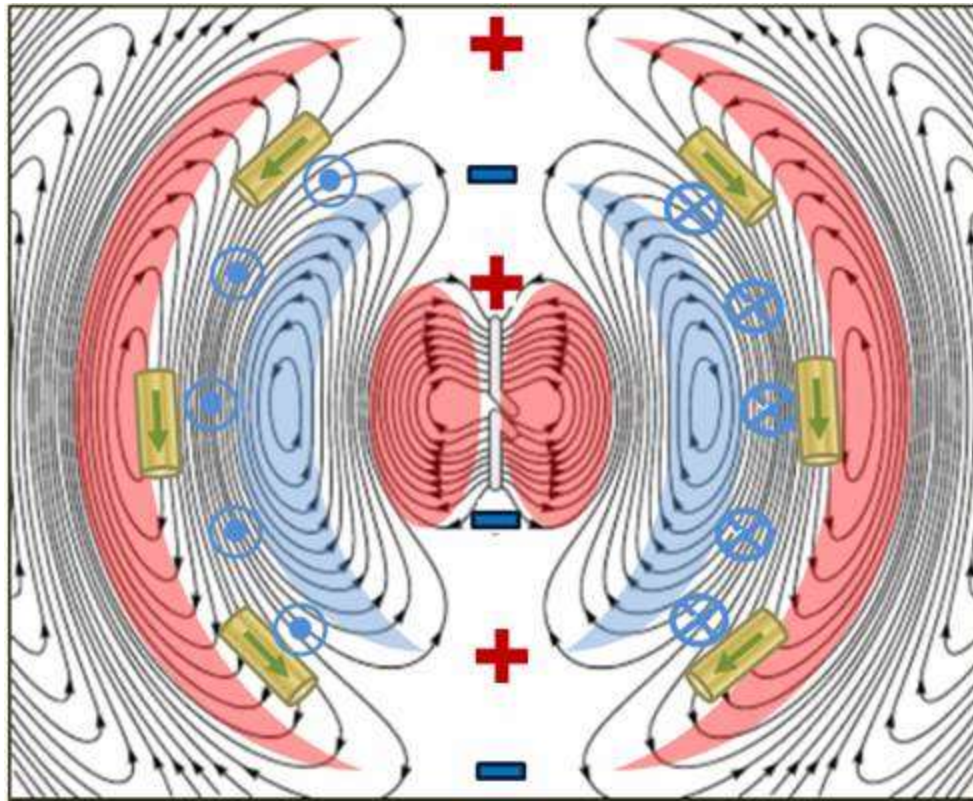
a) Dipole Anrena Emmisions (Positive Pole Upmost)
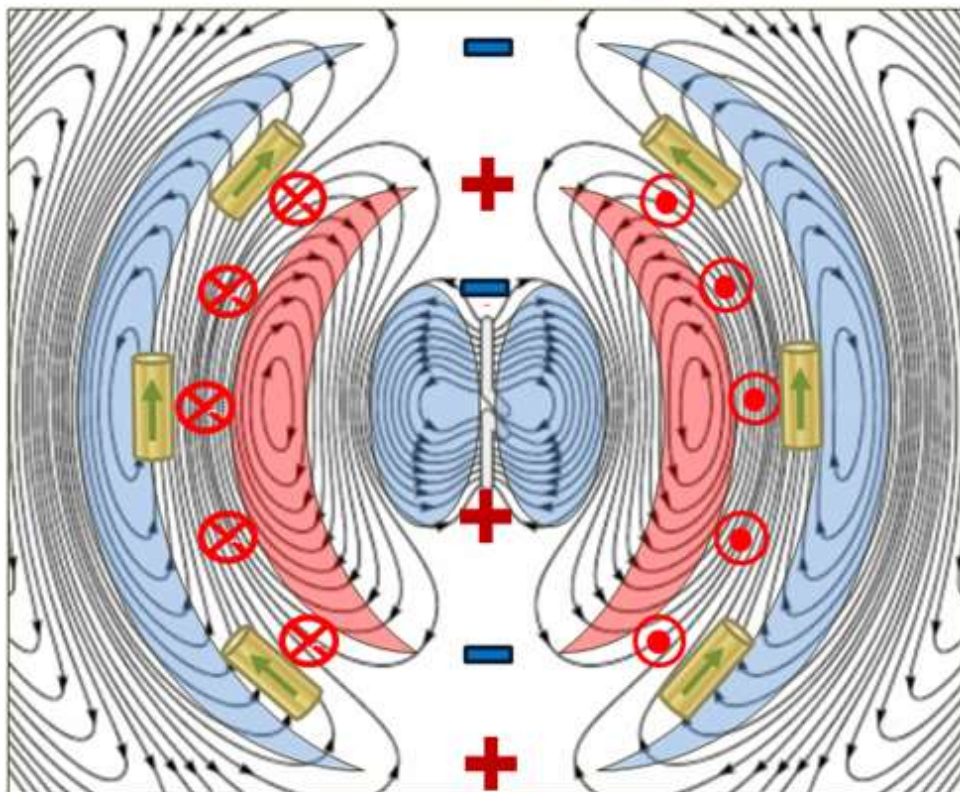
b) Dipole Anrena Emmisions (Negative Pole Upmost)

Figure 3: Radio Wave Energy-Field Patterns for a Dipole Antenna

Figure 3 and the Wikipedia animated gif show a cross section through a dipole antenna highlighting the field-energy patterns being generated. They clearly show how the field-energy of each successive detached concentration of field energy (an energy **peak** or **crest**) moves away from the dipole antenna with the form of an expanding partial-torus. Each adjacent crest is highlighted by the red and blue bands and, because each crest is detached electric field energy generated by the dipole antenna, there is no field-energy flow around each crest as suggested by the arrowed flowlines. However, each crest does have a **circular magnetic field** (as highlighted by the arrow tip and quill icons), which is analogous to the circular magnetic field around a wire conductor carrying electric current.

To re-iterate: because there is no flow of field-energy around each crest and thus **flowlines**, which suggest energy-field flow around each crest (as in figure 3) are very misleading. These lines represent **isoclines** that map the field-energy concentrations of each crest and trough within the radio waves: they are analogous to pressure isoclines in a weather map or elevation isoclines in a topographical map. Thus, the arrows within the isoclines should be removed from the diagram to be technically correct. The only field energy flow within each expanding crest is that of the weak circular magnetic field, and its flow direction is tangential to the outwardly expanding doughnut crests as indicated by the arrow-tip-and arrow-quill icons of figures 2 and 3.

The **directional flowlines** as in figure 3, the animation and the video, and in many other graphics representing electric fields and radio signals, are simply incorrect and misleading; thus, all such directional arrowheads should be removed.

The direction of the circular magnetic field within each crest can be determined using **Fleming's Fist Rule**. Should you assume that electric current moves from a positive to negative terminal then you are looking at the movement of positive charge carriers (CCs) and the right-hand version of the Fleming Fist Rule applies. Should you assume that electric current moves from a negative to positive terminal then you are looking at the movement of negative CCs and the left-hand version of the Fleming Fist Rule applies. Either way, you will find that circular direction of the circular magnetic field corresponds to that indicated by the arrow-tip-and arrow-quill icons of figure 3.

Each crest has arbitrarily been coloured red or blue in figure 3, but that is not meant to imply any positive or negative charge characteristic: each crest is an expanding concentration of field energy that has the flow pattern of a circular magnetic field; and that circular flow direction reverses for each adjacent crest. The '**+**' and '**-**' symbols associated with each crest in figure 3 indicate the polarity of the dipole at the time at which it was generated.

The **brown-coloured cylinders** in figure 3 represent sections of a wire conductor that act as a signal-pickup **aerial**. Assuming each wire is orientated parallel to the advancing crest, as each crest arrives, it represents a vertically up or down magnetic field whose flux is moving through it, which **induces** an electric current in the direction indicated. For the next crest, the direction of the magnetic flux is reversed, so inducing a current in the opposite direction. The **alternating current** (**AC**) so generated will be synchronous to the radio wave frequency as dictated by the rate of pole switching in the source dipole antenna. The received signal may be amplified and fed to an electromagnetically driven diaphragm for **analogue sound** or to a **digital decoder** for digitised sound, pictures and/or messages.

Manmade non-photonic EMR is generated by an oscillating current applied across a transmission antenna: it spans the frequency range of **10** to **10^{12}** Hz, covering radar, microwave, television signal and radio wave ranges. Not all radio wave emissions are manmade: they are also created by lightning on Saturn and from plasma by many astronomical bodies (e.g. the Sun, pulsars, nebulas etc.), and targeted by radio astronomers. EMR generated by atoms (**photonic EMR**) is subtly different to manmade (and Nature-made) radio waves. We will consider how in the next chapter.

Atomic Orbits and EMR Generation

Conventional Science (**CS**) supports both shell shaped and 'spdf' shaped electron orbits, with the outer or conduction band electrons moving under the influence of an applied EMF to form an electric current within a conductor. CS also contends that photons are generated by electrons jumping from a higher to a lower energy-orbit, and that when photons are absorbed they cause electrons to jump outwards to a higher-energy orbit. Electromagnetic radiation (EMR) is defined in terms of **photons**, which are considered to display both particle and wave-like characteristics. Although CS does not provide a definitive definition or structure for a photon, its frequency (**f**) is related to the energy (**E**) via **Planck's constant** (**h**) as **E=hf**.

Both CS and STEM agree that for an electric current, electrons act as **negative charge carriers** (**CC**), although STEM calls a CS electron a **cetron electron**. For **positive CC**, needed to explain electric current in semiconductors and the Hall effect, CS invokes the use of static temporal cations called 'positive holes', whereas STEM uses an electron-like particle called an **aptron electron**, which is analogous to the electron's antiparticle, the **positron**.

Another difference is that STEM considers that atomic nuclei generate negative and positive electromagnetic fields capable of supporting orbits of negative CC (cetron electrons) and positive CC (aptron electrons) respectively. Such orbits are considered **planar** above and/or below the nucleus rather than totally encircling it, and are called **ionic orbits**. *Note that, for the discussion throughout this paper related to the STEM approach to EMR emission, the terms 'orbit electron' and 'electron' are treated as being generic, and apply equally to both cetron and aptron electrons.*

As already mentioned in the previous chapter, STEM distinguishes between **photonic** and **non-photonic** EMR. Apart from the fact that non-photonic EMR is largely manmade and that the term 'photon' is not used in conjunction non-photonic EMR, there are other clues that structurally these forms of EMR are subtly different to each other. For instance, whereas photonic EMR is 'naturally' generated when an orbital electron moves to a lower energy level within an atom, manmade non-photonic EMR is generated by high-frequency AC electricity. In addition, as can be seen in figure 4a, radio waves can penetrate Earth's atmosphere and other structures that most other types photonic EMR cannot or do so only sporadically.
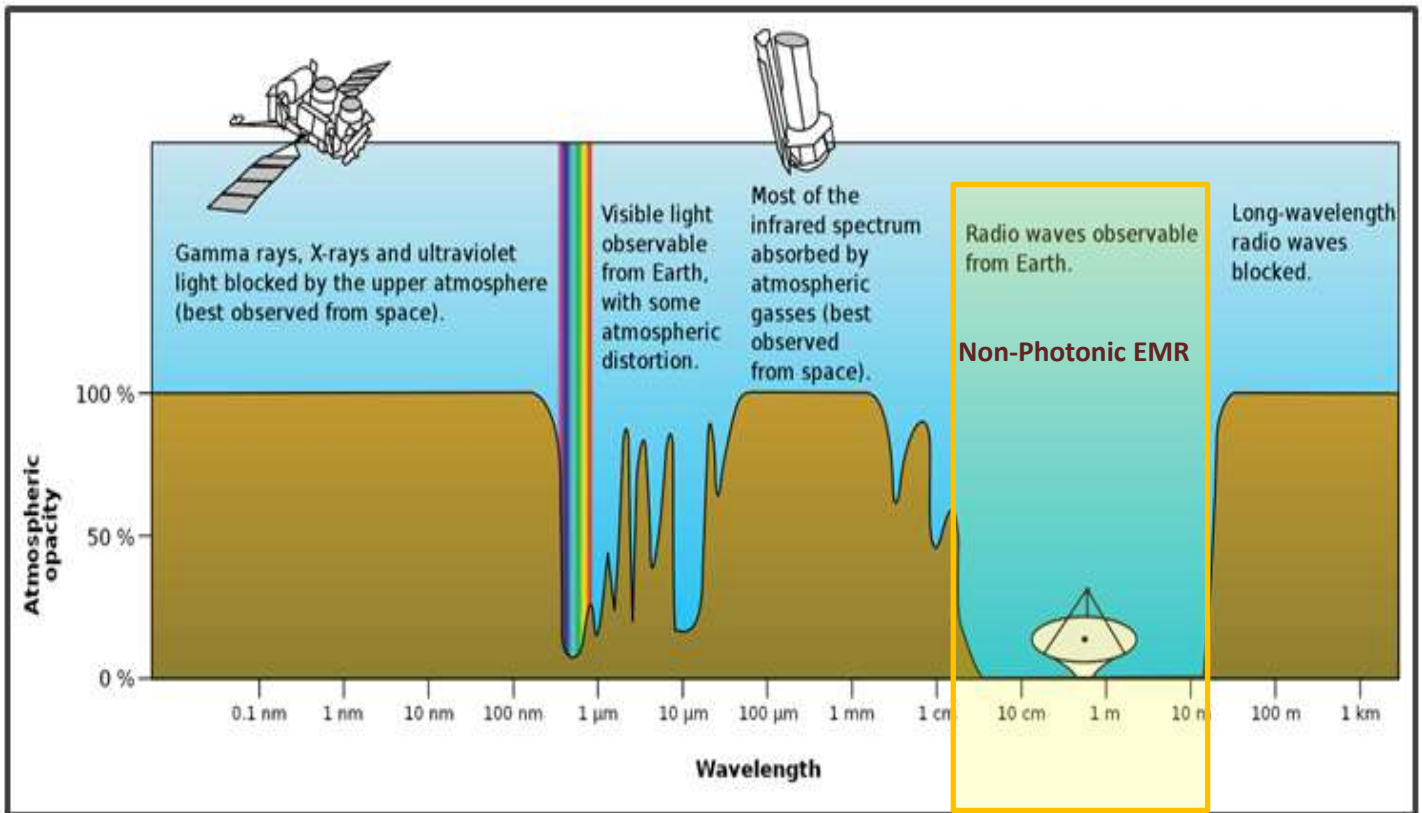
Both the CS and STEM approaches thus associate energy levels with electron orbits and consider that EMR emission and absorption is related to electrons moving to different orbits. An essential difference, however, is that CS defines fixed orbits and associated energy levels for each type of atom. STEM, on the other hand, considers that, due to the structure of its nucleus, the electromagnetic field supporting ionic orbits is unique to each specific atom type, with the location of ionic orbits being **dynamically determined** by the energisation level of the ionic electromagnetic field. When the energisation-level of an atom increases there are corresponding changes to its ionic EM field shape and strength. Such change causes the velocity of otherwise stable ionic orbital electrons to be too slow to maintain their radial location, so they are destabilised and move inwards, increasing in speed until it dynamically matches that of a lower energy orbital within the newly established EM ionic field regime. The electron emits EMR during its transition and while adjustments are made to its speed and radial location to establish a new stable orbital.

CS correctly claims that a photon of EMR energy is emitted when an orbital electron jumps to a lower energy/orbital level (e.g. hydrogen emission of blue light with a jump from level 4 to 2), but fails to provide an explanation of how or why that energy emission is electromagnetic in nature. STEM, on the other hand, develops a physical model that is more pragmatic than mathematical. STEM contends that photonic EMR is derived from rapid flipping and detachment of an electron's energy field, which is analogous to the detachment of the electromagnetic field across an aerial as for manmade non-photonic EMR, but produces a different structure from the field energy so released.

So, exactly how does such a flip/tumble action of an ionic electron generate EMR, and what is the structure and characteristics of the photonic EMR so generated? As discussed in the previous chapter, the switching of the polarity across a dipole antenna causes field-energy to be cut off or detached from the antenna to generate radio waves (**non-photonic EMR**). Similarly, each sudden 360° flip of the **energy-core** of an ionic electron causes its energy-field to become detached and to move away from its energy-core as **photonic EMR** (e.g. visible light).
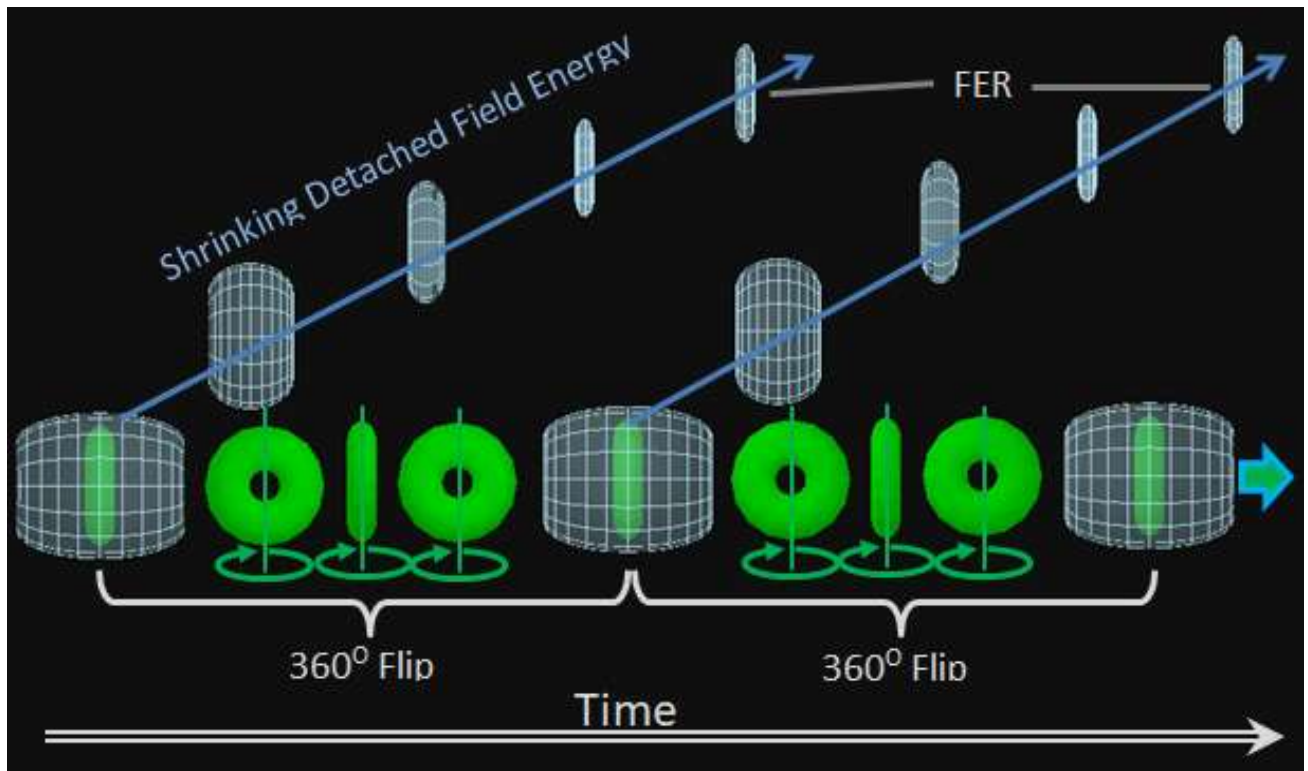

Figure 4b: FER Generation from a Cetron Electron

When the energy core of an orbiting ionic electron undergoes a sudden 360° flip (or spin-around) about an axis that is 90° to its direction of travel, its energy field becomes detached quickly shrinks or compacts into a relatively thin toroidal ringlet of energen called a **F**ield **E**nergy **R**ing (**FER**). The detached FER corresponding to each flip of the orbiting ionic electron flies off tangentially at the point that the electron flips, and away from the source atom. Should the ionic electron continue to flip, the FER so produced all contain the same amount of energen (derived from the electron's energy field) and form into a **single helix** structure (see figure 4c) as they exit the atom as **light ray**. The mechanics and related statistics associated with light ray generation process are described in far more detail in the [Light Rays and Light Beams](#) chapter.

The energen flow within a FER is considered to be purely toroidal, with any potential poloidal flow component being nil or, at very least, below the level of detection. Having only toroidal flow, FER are non-chiral. This means that an e-FER that is flipped 180° looks and is the same as a p-FER whereas, should a cetron electron be flipped 180°, it still remains chirally different to an aptron electron (i.e. a positron). It is also worth noting that FER structure is different to that of [vortex rings](#): the latter only have a poloidal flow component whereas FER are considered to only have toroidal flow component.

Dependent upon the chirality and strength of an ionic EM field, it can support one or two orbital cetron electrons, or it can support one or two orbital aptron electrons. The helix structure of photonic light rays, which are derived from cetron electrons, have **left-handed chirality** (as shown in figure 4b and left in figure 4c), whereas those derived from aptron electrons have **right-handed chirality** (as shown right in figure 4c).

Once free from the influence of the EM field of the parent atom, moving in a non-rotational single helix formation, the spin axis of each FER is orthogonal to their combined direction of travel, as evident from the top graphic of figure 4d. The FER orientation and spin can be thought of as small tyre-like concentrations of energen whose rotational spin causes them to roll along a hypothetical hollow central helix cylinder as shown in figure 4c.

When one looks at an oncoming photonic EMR, the FER arrival sequence (A→B→ C→D or order **1**, **2**, **3** in figure 4d) of a left-handed helix EMR is **counter-clockwise**, and that of a right-handed helix is **clockwise** (A→D→ C→B or order **1**, **2, 3**). This order, plus the points A, B, C and D around the helix circumference, is quite important when considering the polarisation effect of photonic EMR from refraction and reflection (see the [Light Refraction, Reflection and Polarisation](#) chapter).

The **wavelength** of EMR is defined by the wavelength (**λ**) of the helix spiral (see figure 4c) and, with each FER containing approximately the same amount of energen, the energy of a photonic EMR emission is dictated by the FER packing density within the helix and the diameter of the helix. For more energised atoms, the electron flip-rate increases, resulting in increased FER packing density. Differences of FER frequency and associated helix diameter help to explain changes to refractive index with EMR frequency (see the Chromatic Dispersion of Light chapter).
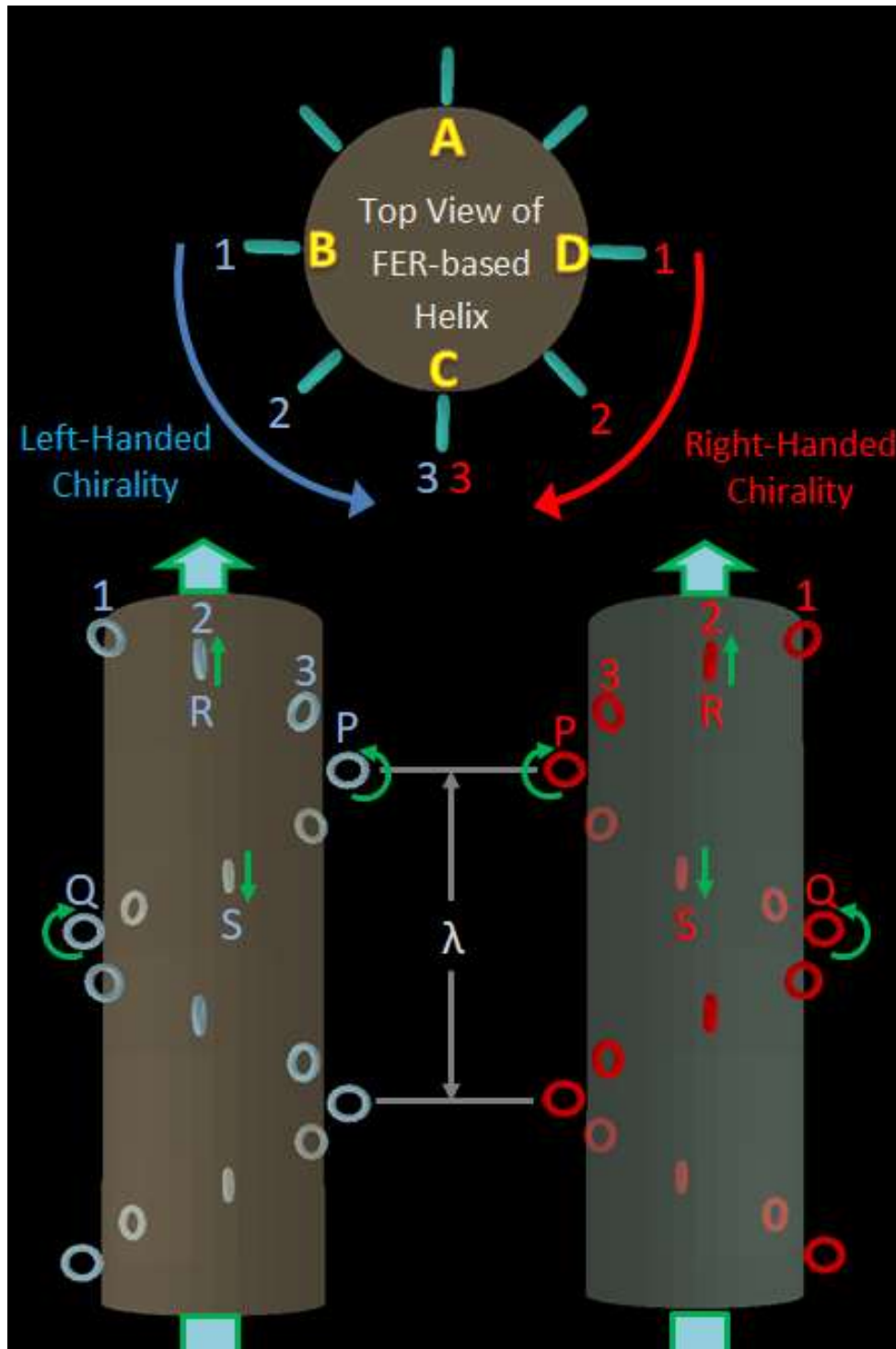

Figure 4c: Left and Right Handed Helix Structure of Photonic EMR

Should two cetron or two aptron electrons be generating EMR from the same ionic EM field, then it is possible that LH or RH double-helix rays (LH show right) might be generated, with each spiral offset by 180° (assuming that an ionic electron pair would be on opposite sides of an orbital). Although it is unlikely that both electrons would re-locate and spin synchronously, it is feasible that double helix rays could be generated from the single atom. The energy content of the double helix forms would be double that of a comparable single helix form, but in other respects would act the same as a single helix. Further research is required to determine whether double helix rays are generated naturally from single atoms and what the ratio of single to double helix rays might be. Certainly, from the STEM perspective, the single and the double helix forms can exist together with both left and right-handed chirality, and do not represent mutually exclusive alternatives.
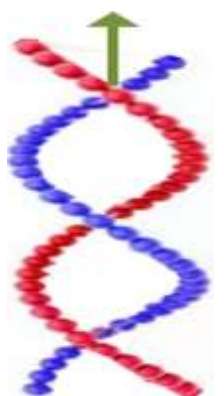
Special Note. Influenced by the double-helix CEWL model of EMR (see Donald Bowen's 2023 paper 'Capacitance and Size of the Electron Based on the CEWL Model') and the beautiful symmetry of the DNA double-helix, previous versions of this paper contended that all photonic EMR emissions had a **double-helix** structure. Unfortunately, despite a considerable amount of modelling, no satisfactory feasible explanation for the double helix model could be found when only one orbital electron is involved. Hence the default structure is the **single-helix** model associated with photonic EMR from a single orbital electron.

CEWL Model
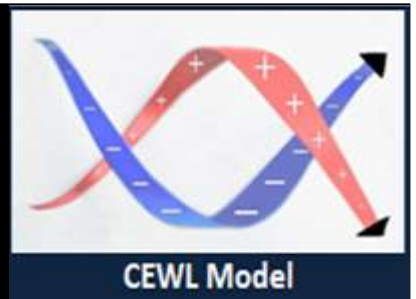
With the electric (**E**) and magnetic (**B**) fields of EMR being orthogonal, a plot of their strength within a EMR produces a pair of synchronous orthogonal sinusoidal E-B curves such as shown bottom in figure 4d. CS attributes this electromagnetic footprint to **electromagnetic waves**, whereas STEM contends that they result from the FER-based helix structure of photonic EMR.
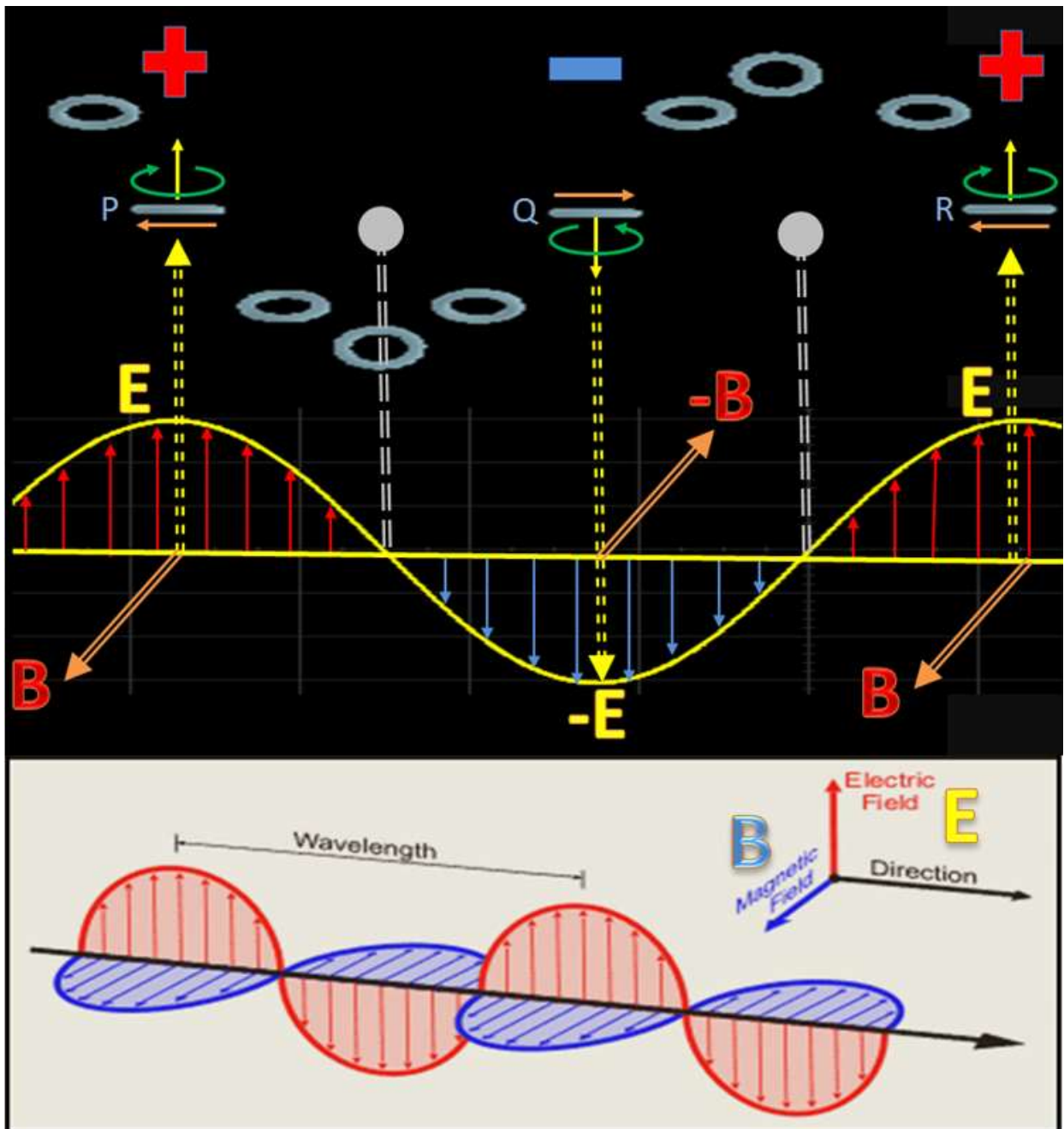
Figure 4d: Electromagnetic Fields Generated by Left-Handed Single Helix EMR Structure

Referring to the representation of a helix ray of EMR in figure 4d, the FER labelled **Q** is closer to the viewer than those labelled **P** and **R** which they are on the opposite side of the ray's helix structure. Although these three FER have the same orientation, because they are on opposite sides of the helix, the spin direction of FER **Q** (as indicated by the **green circular arrows**) are opposite to the FER at P and R. When viewed from above, the circular spin of FER **Q** presents as an **electric field** of strength **-E**, whereas that of **P** and **R** is in the opposite direction, and thus represents an electric field of strength **+E**.

Similarly, the **magnetic field** is defined by the tangential flow rate indicated by the orange arrow, which is measured in direction orthogonal to the FER spin direction. For the FER **Q** the magnetic field points right corresponding to a magnetic field of strength **-B**. Similarly, the tangential flow direction for FER **P** and **R** is in the opposite direction, and thus represents a magnetic field strength of **+B**.

A useful technique to ascertain the spin direction of FER within the light ray's helix is to consider that the FER are analogous to a tyre rolling along e outer surface of the cylinder inside the helix. This technique works equally well for left and right-handed helices.

The electric (**E**) and magnetic (**B**) field strengths of all FER in an EMR helical spire are identical, but due to their different orientation as determined by their location within the FER helix, their effective field strength components in the orthogonal directions defined with respect to the orientation of FER **Q,** produce the typical sinusoidal E-B curves as shown. Furthermore, it does not matter where those orthogonal field-strengths are measured around the EMR's direction of travel, the electromagnetic field-strength plot produced would be the same in terms of amplitude and wavelength, only varying in a difference of phase.

Although FER each contain only a relatively small amount of energen, in large numbers such as when multiple rays travel together as a beam of light, they are able to generate detectable levels of <u>radiation pressure</u>. Consequently, FER can be considered to represent discrete particles that move in wave-like formations, that of an EMR helix, so acquiring and displaying particle-wave duality characteristics. Or, put another way, with the STEM's helix structure of photonic EMR, observed particle-wave duality characteristics would be expected rather than appearing enigmatic.

Both CS and STEM contend that photonic EMR emissions are generated by electrons moving to different lower-level orbits, although both the processes involved and the nature of the energy levels involved are different. For the CS approach, the energy levels are fixed, defined in terms of orbital shell energy levels, with the unique emission spectra associated with each atom type (see figure 4e) resulting from jumps between **fixed orbitals**. STEM, on the other hand, contends that the energy levels of **ionic orbitals dynamically change** in response to an atom's energisation level, with the FER of EMR being generated by the flip-action of electrons relocating to a new lower-energy orbit location.
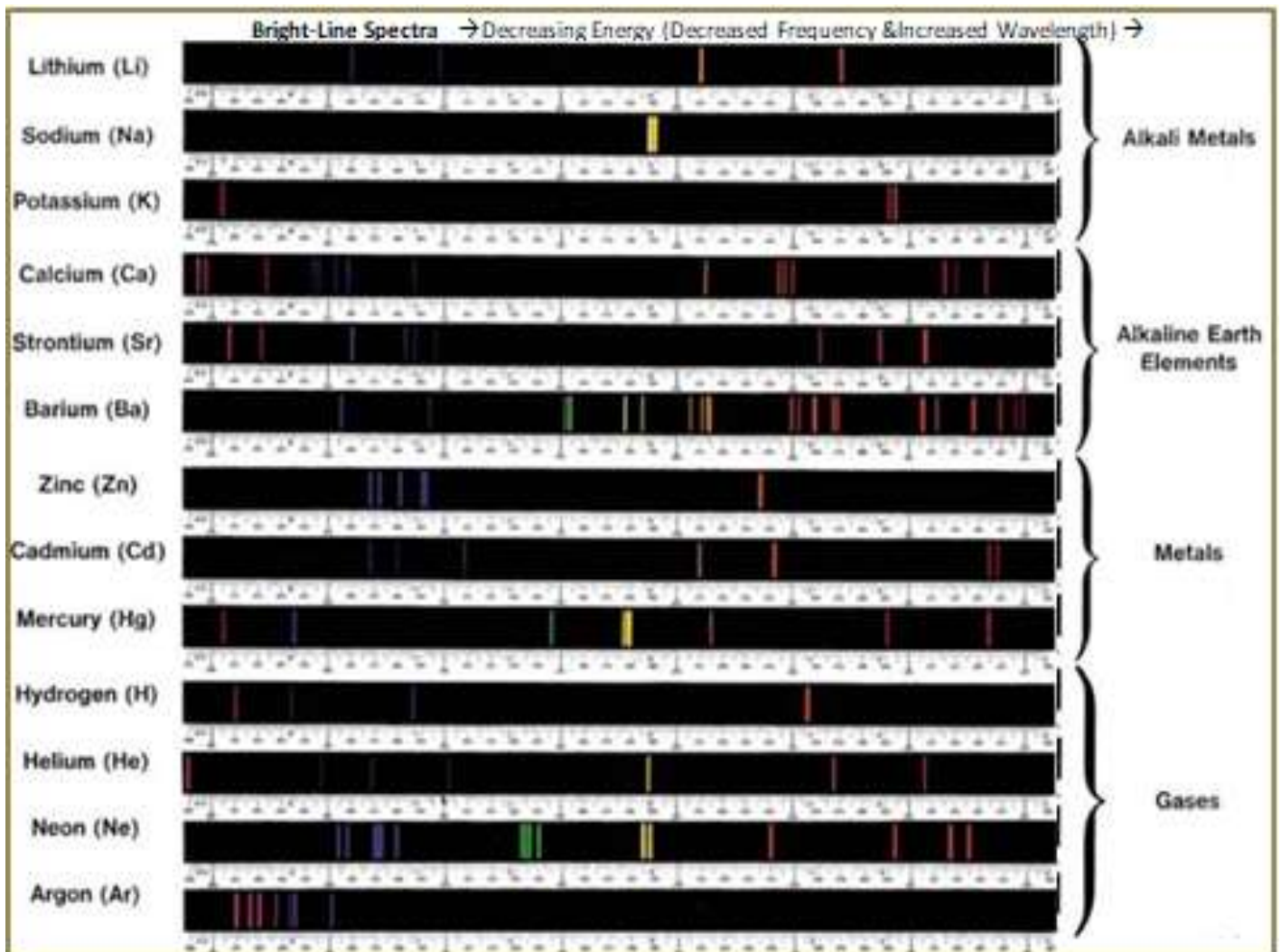

Figure 4e: Emission Spectra of Elements by Element-Group

The **electric field** component of an ionic EM field is determined by field's **toroidal flow** direction: its strength is determined by the density of field energy and its angular velocity (ω). The **magnetic field** is determined by field's **poloidal flow** component: its strength is similarly determined by the density of field energy and its linear velocity. Although the speed of an orbital electron is significantly lower than the toroidal component of the ionic EM field energy, its speed is influenced by, and ultimately controlled by that component of the field energy.

Only at certain locations within an ionic EM field, referred to as quantum '**sweet-points**', the velocity of the electron match the required velocity to establish a stable orbit. Such 'sweet-points' represent **potential electron orbits** that are dynamically determined by the structure (i.e. the geometry) of the nucleus, which is unique for each type of atom in the Periodic Table, and the energisation level of the atom's ionic electromagnetic field.

The location of quantum 'sweet-points' (i.e. orbit locations) within an ionic electromagnetic field is determined by the strength of the **magnetic component** (i.e. the poloidal component), which generates an inwardly directed **motor force** (see figure 4f) on the orbiting electron that counters the electron's inertia as dictated by its mass and velocity.

Once in a stable orbit, an electron is reasonably unresponsive to small changes in the strength of the ionic EM field, which may cause small shifts of location but without generating significant photonic EMR emission. However, for significant changes of the ionic EM field, so called 'quantum' changes, the 'sweet-points' change as does the electron's speed and location in response.

Whenever an electron moves laterally inwards (energisation decrease) or outwards (energisation increase) through an atom's ionic EM field, it encounters energen flow differentials that cause it to do a 360° flip around an axis parallel to its tangential direction of travel, rapidly and continually which, STEM claims, causes the generation of **photonic EMR**.

The mechanics and related statistics associated with photonic EMR emission are described in far more detail in the [Refractive Index and the Changing Speed of Light](#) chapter with reference to for the light ray generation process and the implications of light travelling through a range of different media.
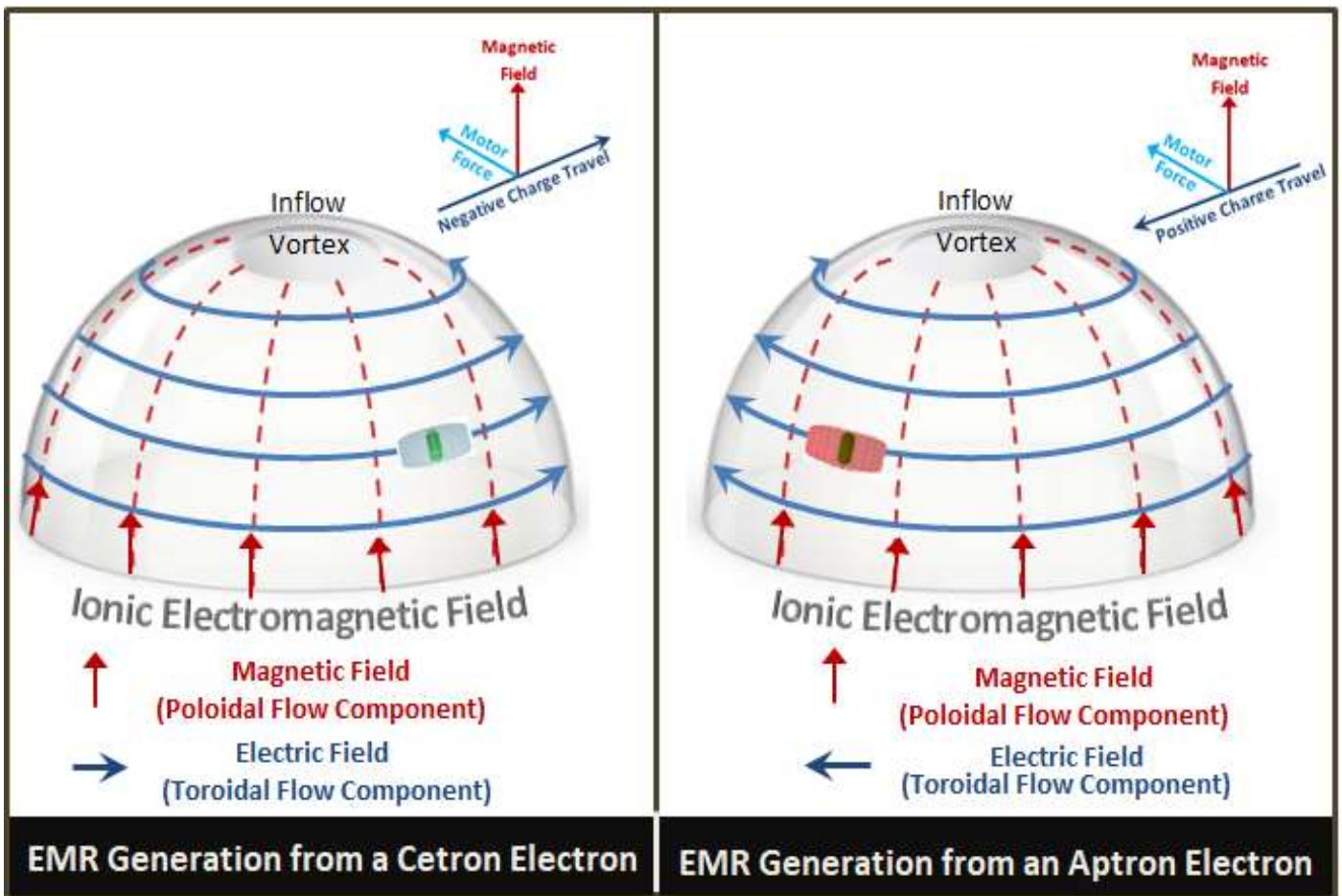
Figure 4f: Ionic Cetron and Aptron Electron Orbitals

Let us now discuss absorption and re-emission in terms of photonic EMR in the **frequency range of light**. Figure 4g lists the frequency and wavelength for the various colours in the white light emission spectrum.

Figure 4h shows an idealised representation of the spectrum associated with direct sunlight; the absorption spectrum after the light passes though cloud; and the re-emission of light from the energy in the cloud of that absorbed light.

color	wavelength interval	frequency interval
red	~ 625-740 nm	~ 480-405 THz
orange	~ 590-625 nm	~ 510-480 THz
yellow	~ 565-590 nm	~ 530-510 THz
green	~ 500-565 nm	~ 600-530 THz
cyan	~ 485-500 nm	~ 620-600 THz
blue	~ 440-485 nm	~ 680-620 THz
violet	~ 380-440 nm	~ 790-680 THz

Continuous spectrum

Designed for monitors with gamma 1.5.
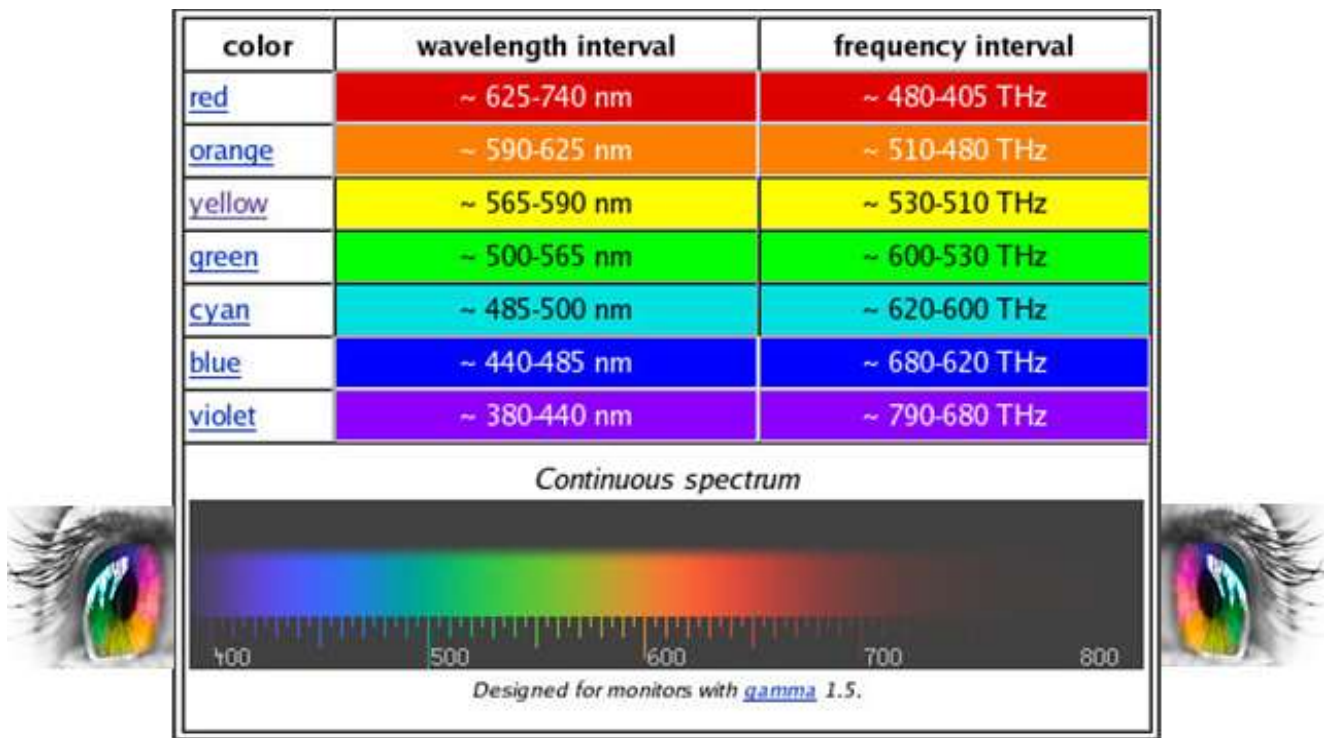
Figure 4g: Frequency and Wavelength of Colours for Visible Light EMR

Direct sunlight is referred to as is termed 'white light'. It consists of multiple light rays having full range of frequencies of visible light (and a little wider) that combine to produce a continuous rainbow-like spectrum. However, when white light passes through cloud, the water, dust and atmospheric gases can absorb certain frequencies, resulting in black lines (or absorption-bars) within the associated **absorption spectrum**, as in figure 4h.
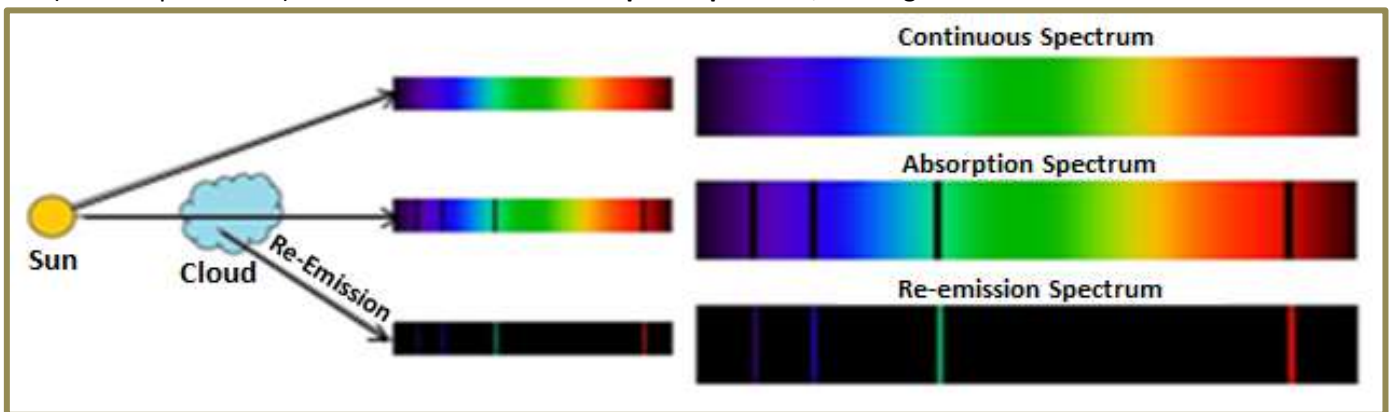

Figure 4h: Emission and subsequent Absorption and Re-Emission Spectra

When an **incident ray** strikes a particle within the cloud, its FER energy is partly scattered and partly **absorbed** by the CES within the atom's nucleus (NOT by the fast moving ionic orbital electron itself), with the increased energisation level being reflected by a slight increase of the strength of the atom's ionic EM field.

Most absorbed frequencies are **re-emitted** as an EMR ray of a slightly lower frequency. The absorbed energy increases the strength of the ionic EM field, which means that the electron, previously in a stable orbital, is now moving too slow to stay in that orbital radial location, with the now increased motor force making it move inwards. There are two main scenarios as represented in figure 4i.

The first scenario relates to electron pathways A→B→C. Within each dynamic orbital, there are associated **tolerance limits**. The increased energisation of the ionic EM field results in a new optimal orbit (the solid yellow circle) such that the old orbital lies within its tolerance limits. The orbiting electron at location A experiences increase inwards **motor force** due to increased magnetic field flux (see inserts in figure 4f), which cause it to accelerate and move inwards and, because of the increased strength of the toroidal flow component of the ionic EM field, it gains speed and starts to rapidly flip. However, it invariably overshoots the new optimal orbital and end up at location B within the tolerance limits of the optimal orbit. However, being unstable at B (the motor forces are now too strong), the electron would start to gradually work its way towards the optimal orbital and stability, generating photonic EMR as it goes. However, by emitting EMR, the flipping electron is effectively helping to de-energise the atom to the extent that it ends up in a stable orbital at point C, slightly outside but quite close to its original orbital (hence the reduction in frequency of the re-emitted EMR). This first scenario emphasises the dynamics between energisation level and the potential orbitals.

The second scenario relates to electron pathways P→Q→R. Here the energisation of the ionic EM field from the incident EMR is sufficient to make the orbital electron (at location **P**) move to and settle into a new stable orbital with a smaller radius at location **Q**, possibly accompanied by some spinning but with minimal EMR emission. This has the effect of increasing the kinetic energy of the orbital electron, which represents potential energy stored within the new smaller-radius orbital. The stored potential energy may later be released as **re-emission EMR** should the cloud cool down, which causes the ionic EM field of the atom to become de-energised, so that there is a reduction of the inner motor force. Consequently, the electron is destabilised and starts to move back outwards, flipping and emitting EMR as it goes (as represented by the dashed path Q→R in figure 4i), until it reaches a stable new orbital very close to the radial location of the original orbit.
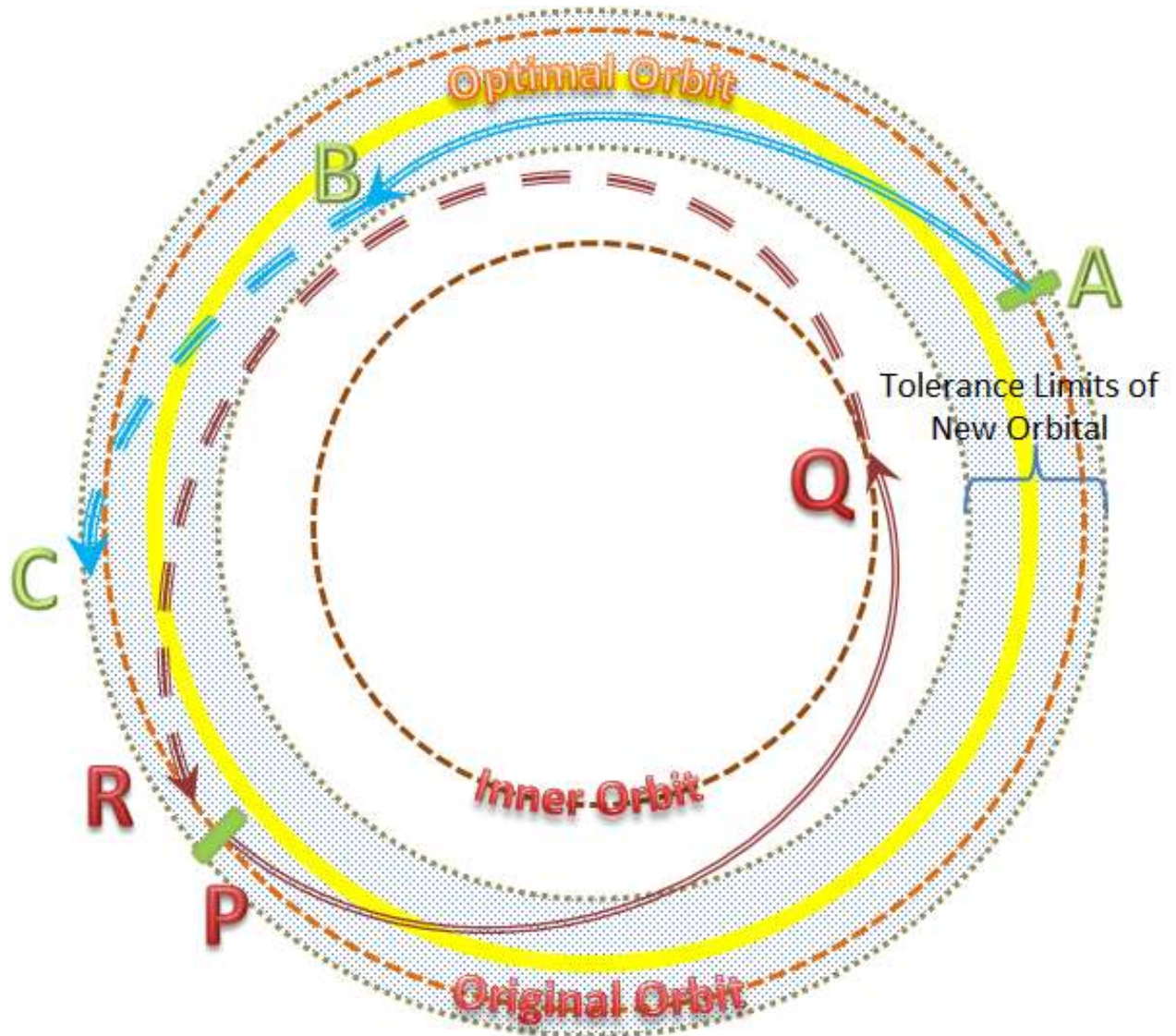

Figure 4i: EMR Absorption, Emission and Re-Emission Transformations

The Refractive Index and the Changing Speed of Light chapter provides a more detailed description of how FER helices are generated and affected by different carrier media. Although there are differences in terms of the way in which photonic and non-photonic EMR are generated, both forms consist of the same material (energen in the form of EM field energy) but have distinctly different structures and behavioural characteristics.

 For example, photonic EMR can be reflected, refracted and/or scattered by atoms within a transparent medium; or reflected and/or absorbed by non-transparent media. Non-photonic EMR, on the other hand, is only disrupted by significant electromagnetic disturbances or metallic surfaces (e.g. a Faraday cage or electromagnetic shielding). Otherwise, it can pass through many materials (e.g. the walls of houses, pockets, purses etc.) and (with reliable Telcos) remain intact, apart from minor loss of fidelity related to minor field-energy absorption and near-filed deflection by atoms. Another difference is that, although there is some frequency overlap between photonic infrared EMR and non-photonic microwave EMR, only microwave frequency can be tuned to the resonant frequency of the ionic electron orbit(s) of atoms so that the energy levels and the magnetic moment of the atoms are maximised.

CS, on the other hand, does not identify or acknowledge any difference between photonic and non-photonic EMR, and consistently represents manmade radio waves as being part of an EMR continuum as in the figure 4j.

Another important difference between the CS and STEM approaches to photonic EMR emission is that CS considers that the orbital electron directly absorbs EMR to jump to a higher fixed orbital; and suddenly sheds energy in the form of emitted EMR to move to a lower fixed energy orbital. After significant research and modelling effort, the spectral lines of Hydrogen, the simplest of atomic structures, were split into **fine structures** via Perturbation Theory, allowing the spectral lines for hydrogen to be quantified. However, although the mathematics is well tuned for **Hydrogen**, the theory does not extend very well to other atoms, and represents a major dilemma that suggests something is amiss.
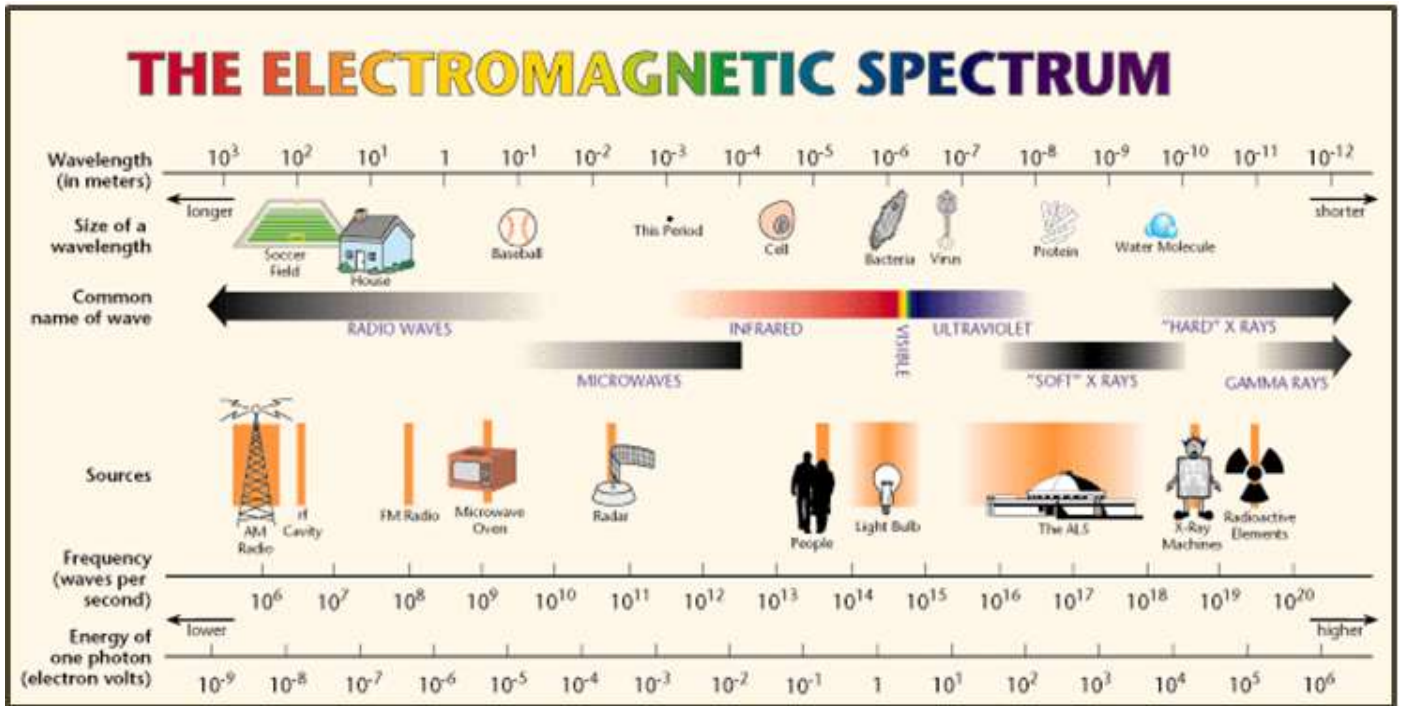

Figure 4j: Conventional Science View of EMR Continuum

STEM, on the other hand, contends that the CES of an atom absorbs or discards energen that, when it results in significant dynamic changes to an ionic EM field, causing or caused by the relocation of the resident orbital electron. With small changes able to be accommodated within the tolerance level of existing orbitals, a significant (or quantum) change of the energisation level of an atom's nucleus is reflected in its ionic EM field, which causes movement of electrons between old and new dynamically generated potential orbitals. This is a subtle but important difference between the two approaches, with being CS locked into fixed orbitals whereas STEM is not.

As the name 'electromagnetic radiation' suggests, CS promotes the idea that EMR consists of **electromagnetic waves**, which are considered to consist of wave-like **pressure-pulses** of electromagnetic energy and momentum moving at the speed of light. However, such electromagnetic pressure-pulses need some type of substrate to sustain them across the vast distances of Space, and one school of thought is that support medium is luminiferous aether. However, despite many high profile attempts such as the Michelson–Morley experiment have failed to provide any evidence supporting the existence of aether. And certainly the STEM approach does not rely upon the existence of aether.

In support for STEM's helix structure for light, H Petek's December 2020 research article titled 'Innovative Experiment Takes Snapshots of Light…', states that '*The team performed an ultrafast microscopy experiment, where they trapped green light pulses of 20 fs (2 x 10^{-14} s) duration as composite light-electron density fluctuation waves, known as surface plasmon polaritons, and imaged their propagation on a silver surface at the speed of light. But they did this with a twist so that the light waves came together from two sides to form a light vortex where **light waves appear to circulate about a stationary common core as a whirlwind of waves**'.

However, perhaps the best endorsement for the FER-based explanation of photonic EMR is STEM's ability to provide direct and reasonably simple feasible explanations for light-related phenomena such as the refractive index of light passing through transparent media; plane, circular and elliptically polarised light; the chromatic dispersion of light; and exotic forms of light such as optical vortex light.
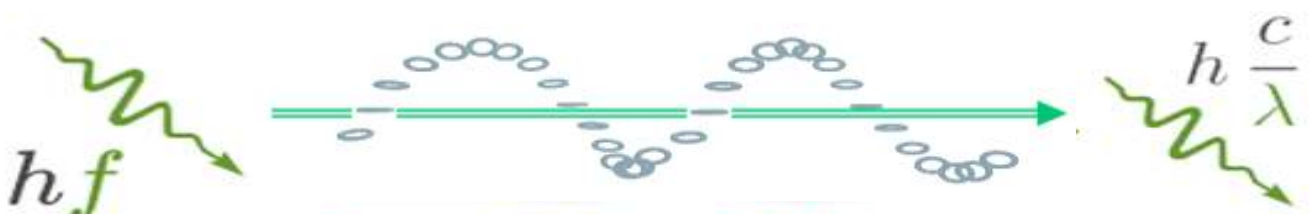
The Photoelectric Effect and Planck's Constant

Photons arriving at the surface of another medium can be variously **scattered** and/or generate **photoelectrons**.

EMR scattering can be **coherent**, which is simple deflection that is analogous to reflection; or it can be **Compton scattering** that causes the emission of an electron and a photon of wavelength greater than (or frequency lower than) the incident photon, which is called the **Compton Effect**.

When an electron (a cetron) is emitted, it is called a **photoelectron**, and the emission process is called the **photoelectric effect**. It represents just one of the possible outcomes for incident EMR as outlined above.

Top in figure 5 shows a simple **solar photocell** incorporating a **stopping-voltage** setup typically used for photoelectric effect demonstrations. The applied stopping voltage negatively charges the photoelectron collection plate and repels photoelectrons; it can be increased to prevent any photoelectrons from reaching the collection plate. The product of the charge of an electron and the minimum stopping voltage provides a measure of photoelectron's kinetic energy. Some more elaborate experimental setups involve light filters that control the wavelength of the incident light.

Such experiments indicate that the kinetic energy of photoelectrons is independent of the **intensity** of the light. Instead, the maximum kinetic energy of photoelectrons s linearly proportional to the **frequency** of the incident light, resulting in the straight-line graphs bottom in figure 5.
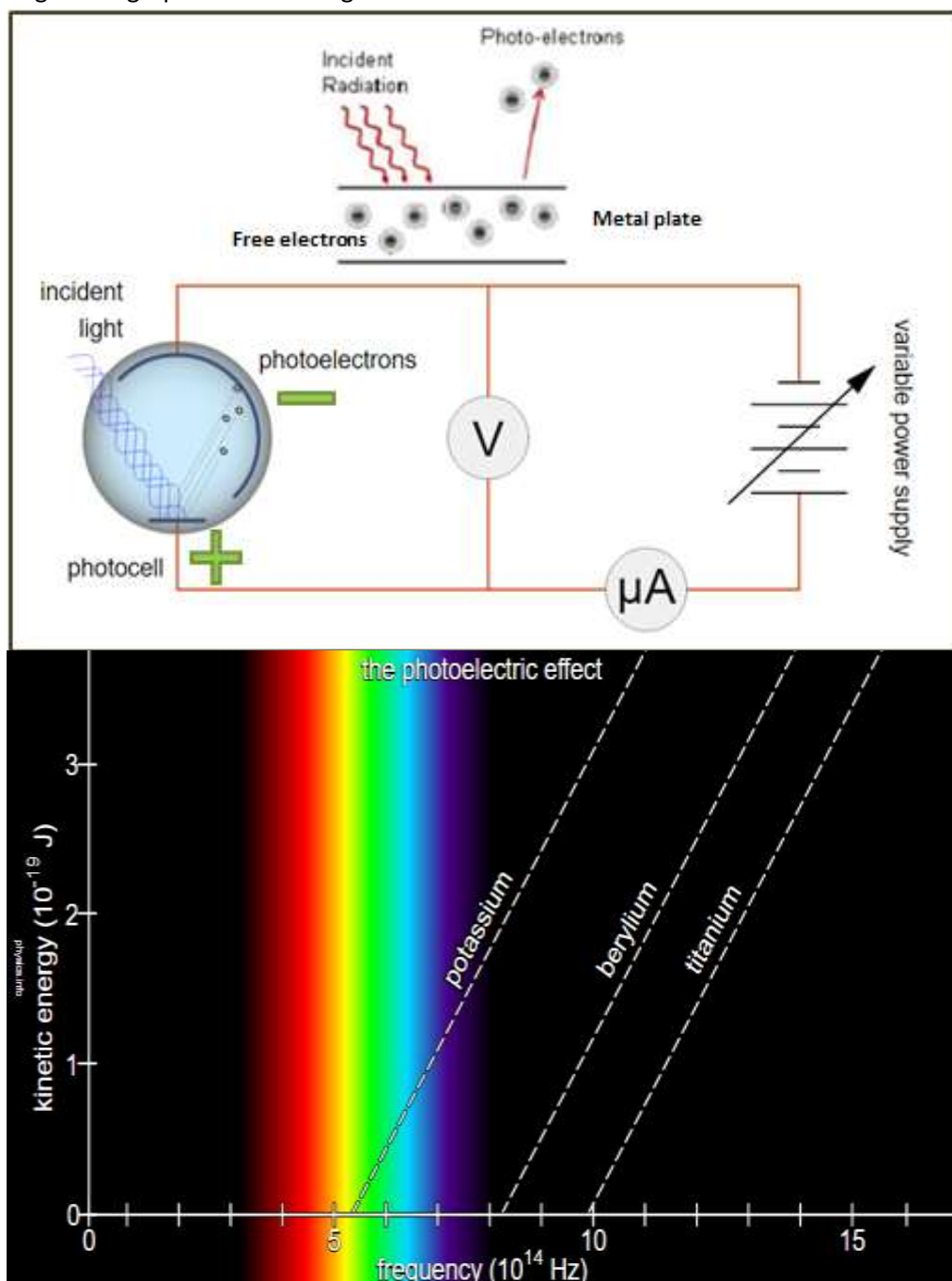

Figure 5: The Photoelectric Effect

Planck's constant is the constant of proportionality as determined by the ratio of the change of kinetic energy change (ΔE) to frequency change (Δf) from experimentally derived graphs such as those shown in figure 5 graph. Planck's constant (**h**) has a value of 6.626 J.s (Joule.sec in SI units) or 4.136 x 10^{-15} eV.s (electron-volt.sec). It may be used to determine the energy of a **photon**, which the amount of kinetic energy that is imparted to an ejected photoelectron as calculated by the equation **E=hf** or **E=hc/λ** using **c** (the speed of light in a vacuum) and the light's wavelength **λ**.

The **threshold frequency f_0** (the frequency for which E=0 in the graphs of figure 5) is the frequency below which no photoelectrons are emitted because they are unable to acquire sufficient kinetic energy to allow them to escape the surface of the incident plate. The **minimum kinetic energy** required to escape the incident plate's surface varies with the composition of the plate, and is called the **work function**. The work function energy is **hf_0**, which also represents the amount of kinetic energy a photoelectron expends in order to escape the surface of the incident metal plate.

The **key aspects** of the photoelectric effect that allegedly cannot be explained in terms of Newtonian (i.e. Classical) Physics are:

1. Photoelectrons are only emitted from incident light with frequency above a threshold frequency.
2. The measured kinetic energy of photoelectrons increases with the frequency of the incident light.
3. The measured kinetic energy of the photoelectrons is independent of the intensity of the incident light.
4. There is essentially no delay between absorption of incident light and the emission of photoelectrons.

With FER-based EMR rather than wave-based EMR, these **four** seemingly inexplicable aspects of the photoelectric effect listed above can be readily explained using Newtonian Physics.

When a light ray is partly or fully absorbed, the recipient atom becomes energised. Should the energisation be sufficient, the atom's ionic EM fields expand with increased energen levels with field energy flow-rates increasing accordingly. For an electron previously in a stable orbit, the increase in the magnetic flux component of the ionic EM field can cause it to experience an increase of the inwardly directed **motor force** (see the inserts of figure 4f), which in turn causes it to accelerate and move laterally inwards. As it moves inwardly, the electron starts to flip and emit low-level EMR as it goes, and should the electron's increasing speed match the increasing inwardly directed motor force, it settles into a stable orbital.

However, should no match between the electron's speed and the motor force be found, the electron eventually encounters the zone in which the motor force suddenly drops to **zero**: this is the zone within the ionic EM field wherein the external magnetic field component (upwards in figure 4f) reverses due to the flow within the inflow vortex. With no motor force to keep it contained, the angular momentum of the now fast-moving electron simply causes it to exit the ionic EM field tangentially and upwards as a free electron. Should the kinetic energy of the free electron be above the **threshold energy** of the incident plate's surface, then it can escape as a **photoelectron**.

The toroidal gradients within the ionic EM field dictate the rate of acceleration, and ultimately the speed, of an unstable electron traversing or orbiting within it; and the poloidal magnetic flux component dictates the inward motor force. However, it is the unique nuclear structure of an atom dictates the geometry and flow patterns of its ionic EM field for any given level of energisation. It ultimately controls the '**critical level of energisation**' at which, for a specific level of energisation, a de-stabilised electron will be unable to find a stable orbital and thus be destined to escape as a free electron.

The energy delivery rate for a specific frequency of light ray dictates the **energisation rate** of a given atom's ionic EM field, and as soon as that 'critical level of energisation' is reached, the orbital electron's journey to exile is sealed. An increase of the intensity of light simply means that many more rays of the same frequency impact that particular atom and, although they will certainly increase its energisation level, once the 'critical level of energisation' is reached, the electron's is programmed to exit the ionic EM field as a free electron. Thus, although the number of atoms hit and able to eject photoelectrons increases, the exit kinetic energy of the photoelectrons is unaffected. This explains key aspect 3 above.

The greater energy of the incident light (as determined by its frequency and FER packing density), the greater is the atom's energisation rate and energisation level achieved; and the greater the energisation level, the more potential orbitals are created and the greater the 'critical level of energisation' becomes. It also means that should 'critical level of energisation' be reached, then the electron's speed at which it encounters the zone in which the motor force drops to zero will be greater, as will its kinetic energy upon exiting as a photoelectron, so explaining key aspect 1 and 2 above.

With FER travelling at close to the speed of light (300,000 Km/sec) as a light ray of appropriate frequency, sufficient FER can be absorbed within nanoseconds to energise an atom's ionic EM field so as to cause photoelectron emission: thus, photoelectron emission is essentially instantaneous, which explains key aspect 4 above.

Increased photoelectron generation means increased levels of ionisation of the target medium due to electron loss. STEM suggests that this is somewhat offset by the release of electrons from b-bonds triggered by collision with newly released photoelectrons and by increased vibration of energised atoms. Unfortunately, CS offers no explanation.

Another problem is that, for the CS approach, a **single photon** is defined purely in terms of delivered energy, but without evidence or consensus as to its physical size, form or composition; or even of how it propagates through Space. Is a photon a single ray or a multiple ray combo; or is it one wavelength long or multiple wavelengths, possibly spanning many metres? There are no real answers to these very fundamental and yet important questions. Certainly, for the photoelectric effect, a single 'photon' is considered to deliver the required amount of kinetic energy to generate a photoelectron. That is not in dispute; however, a photon's physical form and carriage is very unclear, as is the method by which a photon imparts its energy to a single fast-moving orbital electron (or wave-equivalent), so generating a photoelectron.

As a brief summary, according to the STEM approach, EMR energy is due to a combination of FER packing density and associated frequency of each ray's helix structure. Unless they are reflected or scattered, the energen and kinetic energy of the all FER absorbed from an incident light ray, contribute to increase an atom's energisation level. An atom's energisation level consists of the total field energy (energen) stored within its nucleon, and is reflected by the size and strength of its ionic EM fields (each atom, apart from Hydrogen has two fields). FER-based EMR emission provides a radiation-based de-energisation mechanism that is complemented by the reverse process, EMR absorption.

STEM also promotes the concept that, within metal conductors at least, ionic orbits support aptrons (positive CC) as well as cetron electrons (negative CC) and, when a **cetron electron** generates EMR, the helix structure has **left-handed chirality**. Alternatively, should an ionic **aptron electron** generate EMR, the helix structure has **right-handed chirality**.

Should metal conductors provide ionic orbits for both cetron and aptron electrons, an obvious question is 'why are no aptron photoelectrons generated?' The answer to this question relates to the **high work function** of aptron electrons (i.e. positrons) within matter in comparison to the quite **low work function** of cetron electrons. Although the reason why aptron electrons have such a high work function is unclear, there are several possibilities.

One possibility is that, for metal conductors, ionic cetron electron orbits mainly face outwards whereas aptron electron orbits face inwards, which shields them from the relatively low energy levels such as for light. Another possible factor could be that the **motor force**, derived from the electromagnetic fields of atoms within a metallic lattice, push any 'freed' aptrons inwards whereas that acting on 'freed' electrons is outwards. Yet another possibility relates to the dipole nature of cetrons and aptron electrons: for the cetron electron, its (pseudo) positive side would be facing the nucleus as it exits the electromagnetic field of the atom, which gives it an extra push via like-pole repulsion. The reverse would apply to aptron electrons, with their (pseudo) negative side holding them back due to opposite-pole attraction. Notwithstanding these possibilities, there are likely to be other significant factors at play here that have not yet been identified.

Despite the high work factor associated with aptron electrons, they can be released from a metal conductor as free positrons by high-energy EMR. As discussed in STEM's Volume 2 paper on Atomic Structure, one possibility (of three possibilities) is that **electron-positron pair production** might be a high-energy version of the photoelectric effect. Should the incident EMR have an energy level greater than of 1.022 MeV, which is in the **gamma ray frequency** range, then an aptron can gain sufficient kinetic energy to overcome its work function and effectively become a photo-positron. Having a much lower work function, an ionic electron (on the opposite side of the nucleus) would also be freed at the same time, which would appear to be the creation, rather than the release, of an electron-positron pair.

Possibly, to support the wave-particle duality of EMR, pair production has unfortunately been touted as an example of the 'creation of matter from EMR', with matter being in the form of a pair of fundamental particles (the electron and positron). STEM, on the other hand, claims the reverse on two fronts: that atoms can create electrons via b-bonds, and that electrons create EMR, which is, in general terms, more along the lines of 'matter creates everything'. Neither CS or STEM claims to know what created matter or EMR (or energen) in the first place, and will probably never know.

Light Rays and Light Beams

As mentioned previously, should a ray of EMR be derived from an ionic cetron electron, then the helix would have left-handed chirality (left in figure 4c); and should it be derived from an ionic aptron electron, then it would have right-handed chirality (right in figure 4c). It should be noted that, although visually similar in appearance in diagrams, the helix forms of unpolarised light are quite different to left-handed and right-handed circular or elliptical polarised light: the structure of the latter forms of light are covered in the Circular and Elliptically Polarised Light chapter.

When looking towards the EMR source, for right-handed helix EMR rays, the FER would trace a circle that appears to be rotating in a clockwise direction as they arrive and pass by (the order 1-2-3 right in figure 4d); FER of left-handed rays would appear to be rotating in an anti-clockwise direction. When looking in the direction that the EMR is travelling, the clockwise/anti-clockwise orders would be reversed.

The length of a light ray at any point in time depends upon its source, source movement at time of emission, its energy (related to its frequency and FER packing density), and its travel history (such reflection, refraction and deflection by obstacles encountered). Although FER consist of only a small amount of energen (field energy detached from an electron), and are close to massless, their spin and associated angular momentum provides them with more directional stability than could be expected from such a small fragile entity. If unobstructed, FER can travel tremendous distances within the helix structure of photonic EMR.

A **light beam** consists of multiple light rays, variously having left and right-handed chirality and possible even a mix of single and (possibly) double helix forms. The contained rays can have various frequencies (and thus various wavelengths), various lengths and be phase diverse. However, because EMR consists of independent FER, EMR wavelength and phase can readily be modified, which makes EMR so amazing, versatile and chameleon-like.

A beam of **incoherent** (or non-coherent) **light** consists of a mix of rays of different wavelength, physical length and chirality. **Monochrome light** contains only rays of the same wavelength but in a varied range of phases. **Coherent light** is monochrome light bearing a fixed relationship between the phase of the helices of adjacent rays. **Laser light** beams are examples of coherent light wherein the phase of the helix of each ray is approximately the same.

A **collimated beam** of light (or other EMR) consists of parallel rays, which will only spread out minimally as it propagates. A **perfectly collimated beam** of light would be a coherent beam whose rays would all be phase-aligned and unbroken from source to target: it would have no divergence and thus would not disperse over distance. However, with FER coupling within rays being quite weak and easily disrupted or phase-modified, in practice, a collimated beam could only be expected to travel a short distance before ray breakdown starts to occur, and thus a **perfectly collimated beam** is only a theoretical ideal. A typical **laser beam** is a well, but not perfectly, collimated coherent light beam, and thus can maintain its focus and intensity over far greater distances than possible using an incandescent light source.

Unlike more concentrated field-energy of electric and magnetic fields, the low field-energy concentration of FER (possibly in the range 8 to 25 µeV) means that EMR rays can seemingly pass through each other while essentially remaining internally intact and without causing significant disruption to each other. One example of this phenomenon is light interference where, although most FER remain unaffected, their electromagnetic field components combine or cancel each other out partially or totally (see the Constructive and Destructive Interference chapter). Although some FER may be mutually deflected and re-orientated, with the large number of FER involved (about 92,000 per wavelength - see figure 7b), the wave structure remains intact overall.

Another similar example of FER apparently passing through each other is the reflection of unpolarised light by a surface that is close to perpendicular to its travel direction (at angles of incidence less than about 5°). Here, the lateral separation of FER within the helix allows reflected FER to pass with only minor physical interference with each other, and although it does cause a left-handed helix to be reflected as a right-handed helix, and vice versa. For circularly polarised light (see the Circular and Elliptically Polarised Light chapter), a similar reversal of chirality occurs.

The ability of light rays to cross paths with each other, and effectively only interfere with each other in terms of their net electromagnetic field strength, is exploited within the amplification chamber of a laser light source, with the net energy-fields of in-phase FER building to emulate in-chamber standing waves, so producing an intense light source.

Refractive Index and the Changing Speed of Light

The speed of light is often defined as 299,792,458 m/s in a (hypothetical) absolute vacuum (a volume void of any energen) but, for convenience, that is often rounded up to 3×10^8 m/s. Although being a smidgen faster than light's 'official' speed in a vacuum, 3×10^8 m/s is the 'speed of light' in a vacuum assumed for this paper (as it is for most other articles about light).

Although the speed of light is often claimed to be constant, like a cyclist pushing against a head wind, light experiences impedance that reduces its speed. Within any transparent medium, the speed of light is less than 3×10^8 m/s, with its actual speed being dependent upon the physical characteristics of the medium through which it is travelling. The ratio of the speed of light in a vacuum (**c**) to its speed in a particular transparent medium (**v**) is defined as the medium's **refractive index** (**RI** or **n = c/v**). **Light refraction** occurs when light passes from one transparent medium into another that has a different refractive index.

With the refractive index of a (hypothetical) vacuum being 1.0, at STP the RI of air is 1.000273i, which is also usually rounded to 1.0 (i.e. to be the same RI as for a vacuum). The refractive index for light-coloured transparent liquids is in the range of 1.3 to 1.5, with water being 1.33 and the maximum for a dark liquid being 1.9 for Arsenic trisulphide and sulphur in methylene iodide. The range for solids is 1.03 to 4.1, with crown glass being 1.333 and glass-like solids in the 1.5 to 1.76 range. Diamond is 2.417, which means that light is about 2½ times slower in diamond than in air.

There are two main approaches to explain the apparent changes in the speed of light in different media. One explanation is that the speed of light does not change, and that it is simply multiply deflected by the electromagnetic fields of medium's atoms, which cause light rays to randomly meander at the same speed through the medium and so take a longer route, giving the impression that it is travelling slower. Although well-defined different pathways exist within birefringent materials, this proposition, which is usually invoked by those who, for their own purposes, want to believe the speed of light cannot change, is absurdly and blatantly incorrect.

The other main explanation, and the one favoured by STEM, is that electromagnetic fields of atoms in transparent solids, liquids and gases (combined with molecular buffeting for liquids and gases) provide impedance (or resistance), which results in the slowing down of light rays. The higher the host media's RI, the more resistance that light rays encounter with a corresponding reduction in FER speed, and thus in light speed.
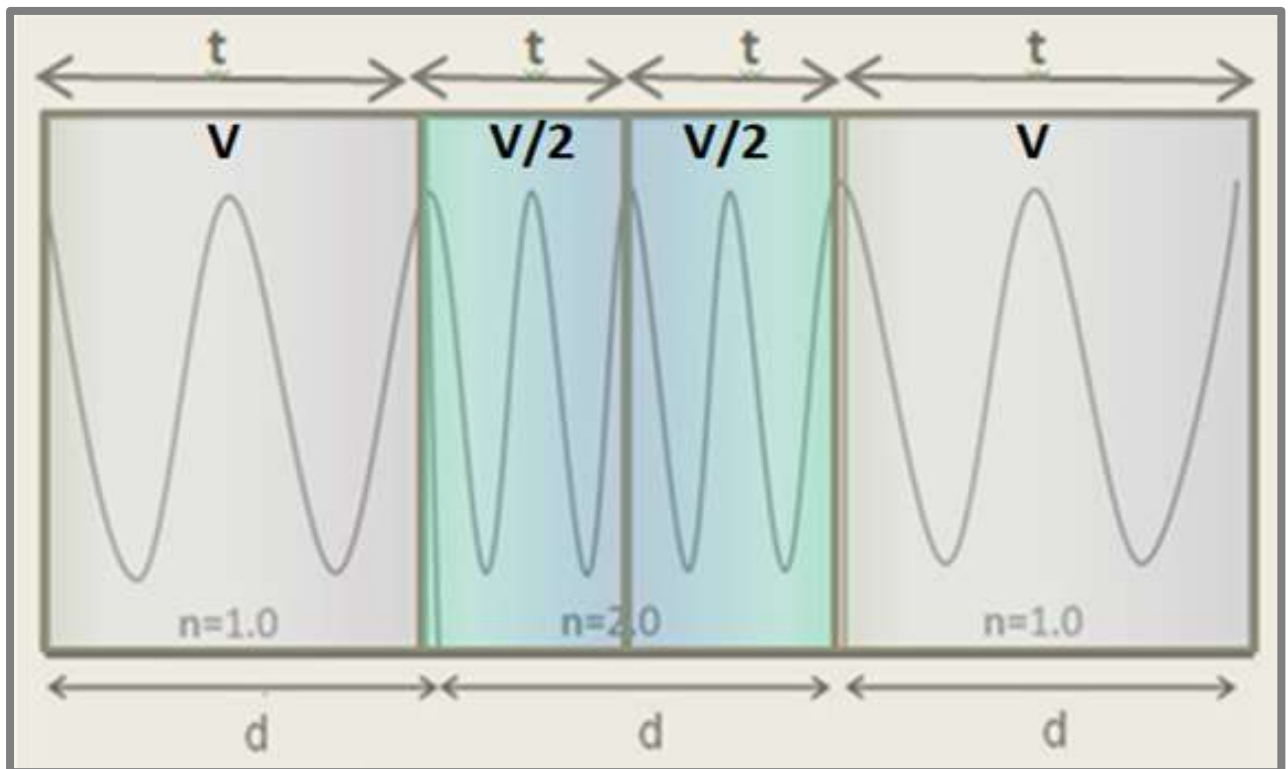

Figure 7a: Light Speed, Frequency and Wavelength

Figure 7a represents a ray of light as represented in terms of its electric field component as it passes from air (RI = 1 rounded) into media with RI = 2, and then back into air. Superficially, it appears that frequency does change with increased RI. However, on closer inspection, you will see that the light's velocity **V** has halved as the RI doubles. Thus, for time **t** in the higher RI medium, the light only travels distance **d/2**, halving its wavelength in the process, but with frequency [f = (V/2)/(d/2) = V/d)] remaining unchanged. So, frequency remains the same but wavelength changes.

With a light ray consisting of FER that all have the same radial orientation within a helix structure, with their spin planes intersecting at the central axis of the helix and separated longitudinally from each other by a gap of one or more FER diameters of separation. When light enters a higher RI medium, the leading FER slow down first, followed by all the others one by one, which reduces their separation gap in their direction of travel, which shortens the helix formation in which they are traveling, and hence the light's wavelength. For the figure 7a example, with FER velocity halving when entering the RI=2 medium, the helix length and thus its wavelength halves: with frequency $f = v/\lambda$, and because both v and λ are halved, there is no change of frequency.

However simple and straightforward the above explanations of how and why light slows down in a medium with a higher RI might be, the more significant question that relates to why FER, and thus the light ray, gains speed upon entering a medium of lower RI. Surely, it would be expected that once slowed down, the 'slow' light ray would continue at the same velocity in the new lower RI medium with its wavelength and frequency remaining unaffected. Why, as in figure 7a, would the light speed up again and its wavelength be restored again as it re-enters the air medium? CS does not address this quite important and perplexing problem: it just seems to be another intrinsic property of light's electromagnetic wave structure with no explanation required or provided.

The STEM explanation for light speeding up as it enters a lower RI medium is that FER are packed quite closely with an estimated longitudinal gap of 6.4×10^{-12} m for light with a wavelength of 5.89×10^{-7} m in air (see the table of figure 7b).

From the STEM perspective, being very close laterally (in the order of 4.4×10^{-15} m), adjacent FER are effectively moving together in a straight line but with a slight lateral offset. However, because all FER have the same electric charge, as represented by the graphic right, they mutually repel each other. As well as keeping the FER equally spaced, the confinement of this mutual repulsive force between each FER by those on either side of it represents the storage of **potential energy** between them.

As the light ray enters a medium with a higher RI, the increased impedance causes FER to slow down and move closer to each other, which increases the repulse-based potential energy: this increase in potential energy between FER is analogous to the increase in potential energy as a spring is compressed. Then, when the light ray enters a medium with a lower RI, that stored potential energy (or part thereof) is released, so accelerating the FER and increasing the speed of the light ray accordingly.

Like Charge
FER Repulsion
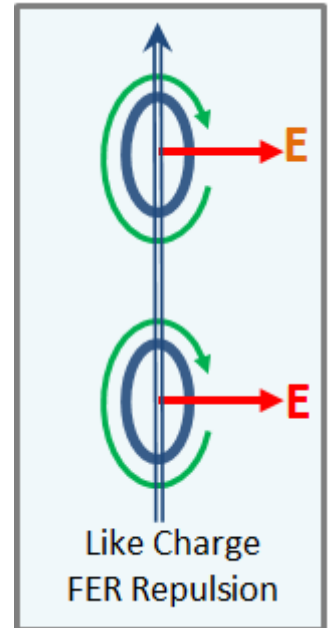
The table of figure 7b represents the modelling statistics used for the development of STEM's FER based helix model for light. The statistics provided relate to **yellow light** based on the **Sodium D line**: it has a wavelength of **589 nm** in air and which, at **509 THz**, is approximately mid-range in the visible light frequency range. The modelling assumes that the source material is a solid rather than being a liquid or a gas, because the dynamics are different for the latter.

Although diagrams such as figures 4c and 10 suggest a wide lateral (S) and longitudinal (L) spacing, the FER within a helix are quite close. A lateral spacing (S) of 4.4×10^{-15} m corresponds to an electron flip period of 2.67×10^{-21} sec, which is far faster than the current-switch times for manmade non-photonic EMR. With a longitudinal spacing (L) of 6.4×10^{-12} m in air and a lateral spacing (S) of only 4.4×10^{-15} m, immediately adjacent FER can be considered to be travelling together in a straight line, with there being about 92,000 FER contained in a wavelength of 589 nm: and that is a lot of FER.

Light Frequency (Sodium D Line)	Number of FER (One Wavelength)	Lateral Spacing (S)	FER Diameter
5.09×10^{14} Hz	92,000	4.4×10^{-15} m	8×10^{-13} m
Electron Orbital Diameter (Octagonal Nucleus)	**Electron Tangential Orbit Speed**	**Electron flip Period**	**Helix Diameter (D)**
5.5×10^{-11} m	1.76×10^5 m/sec	2.67×10^{-21} sec	13×10^{-11} m
Host Material RI	1.0 (air)	2.0	4.0
Light Speed	3×10^8 m/sec	1.5×10^8 m/sec	0.775×10^8 m/sec
Wavelength	5.89×10^{-7} m	2.95×10^{-7} m	1.48×10^{-7} m
Longitudinal Spacing (L)	6.4×10^{-12} m	3.2×10^{-12} m	1.6×10^{-12} m

Figure 7b: Statistics Related to the Modelling of EMR Emission and Change in the Speed of Light

To appreciate the basis of the modelling and related statistics, some understanding of the STEM atomic model, and the electromagnetic ionic field in particular, is first required. As addressed The STEM Approach Volume 2: Atomic Structure paper, the STEM atomic nucleus has a polygonal lattice-like structure of proton and neutron layers consisting of interconnected I-form nucleons. The electromagnetic ionic field of an atom is generated by the combined EM fields of **swivel down quarks** within an atomic nucleus's upper proton or neutron layer, with the inflow EM fields of the swivel quarks combining to form a broad dome-shaped ionic inflow EM field as shown in figures 4f and 7c.
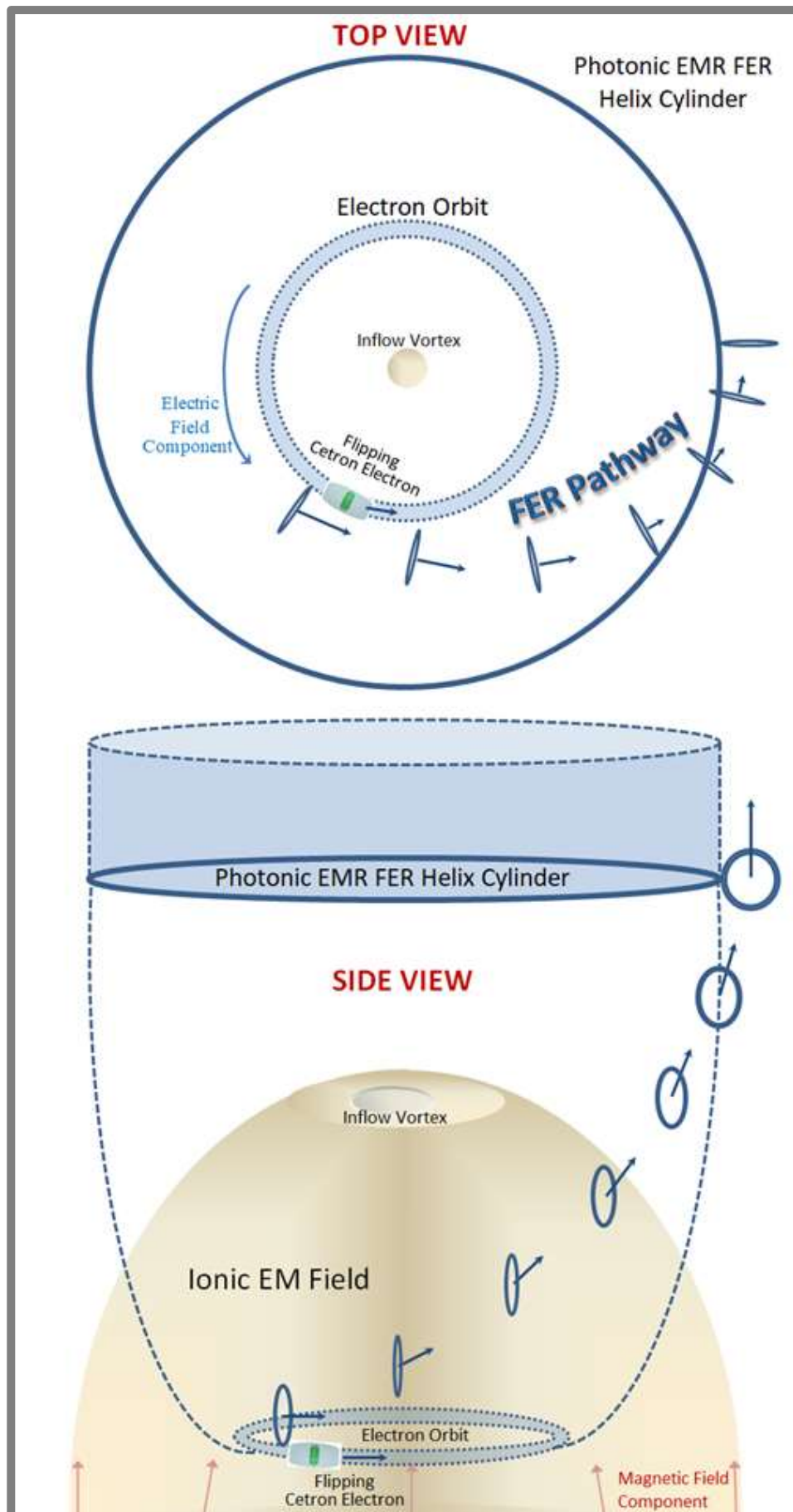

Figure 7c: Generation of FER Helix from an Ionic Orbital Electron

With the ionic electron moving in the toroidal flow direction of the ionic EM field, the left-handed open palm version of Flemings Rule can be used to confirm that the resultant **motor force** would be inwards (as shown in the inserts of figure 4f) and so counter its inertia (i.e. propensity to travel in a straight line). It is worth noting that the inflow vortex of the ionic EM field (as shown in figure 7c and left in figure 4f) serve to draw in (i.e. attract) available free cetron electrons that might in turn become orbital electrons. This is a most important mechanism that homes free electrons that have previously been moving as an electric current before the applied EMF ceases: without the inflow homing-mechanism, such electrons could remain forever homeless and the resulting ionisation of electrical conductors could become a problem. Another aspect of an ionic EM field supporting an orbital cetron electron is that its toroidal field component would serve to repel any approaching free aptron electrons.

The frequency of the light is dictated by the period of the ionic orbital electron (i.e. the time taken for one 360° orbit) as it generates FER. The frequency of yellow light corresponding to the D line of a Sodium atom is 509 THz and the corresponding wavelength in air is 589 nm. The period of both the orbital electron and the light ray is 1.96×10^{-15} sec.

Figure 7c shows how a typical FER is generated and becomes ejected from the source atom's ionic EM field. When the orbiting electron does a rapid 360° flip, its field energy becomes detached from its energy core to form a FER. That newly created FER immediately flies tangentially away from the electron orbital, and is carried upwards by the magnetic component of the ionic EM field, so following a partial spiral pattern. By the time that the FER is free from the influence of the ionic EM field, it is travelling upwards (as shown in figure 7c) at the speed of light. This pattern is repeated for each flip of the orbital electron, with all the FER forming the helix structure of a single ray of light. Importantly, the diameter of the FER helix is greater than the electron's orbital diameter.

According to STEM, the sodium atom's nucleus consists of a double-layered octagonal lattice structure with a diameter of about 8.4×10^{-11} m. The electron's orbit diameter is not accurately known but, considering the diameter of the sodium atom's nucleus, it most likely falls in the 5 to 6×10^{-11} m range. A nominal mid-range value of 5.5×10^{-11} m has been assumed for the electron orbit diameter in the provided modelling statistics: for a period of 1.96×10^{-15} sec, this corresponds to a tangential orbit speed of 1.76×10^5 m/sec.

The helix diameter range is 8.4 to 18.4×10^{-11} m, with the upper limit allowing for b-bond lengths of 10×10^{-11} m between adjacent atoms (assuming that the source material is a solid). A mid-range value of 13×10^{-11} m was used for the helix diameter for the statistics tabulated figure 7b, which is about 2.4 times the diameter of the electron orbit.

Because the diameter of the energy core of an electron is 8×10^{-13} m, the diameter of a FER (which is a shrunken form of the electron's outer energy field) has also been assumed to be 8×10^{-13} m. Within the helix of a light ray travelling through air, a longitudinal centre-to-centre FER spacing of 6.4×10^{-12} m has been used. Thus, one wavelength of the light ray would contain 92,000 FER with a lateral spacing of 4.4×10^{-15} m: closer longitudinal spacing would both increase the number of FER and reduce their lateral spacing. As the light ray passes from air (RI=1) into a RI=2 medium, its speed, wavelength and longitudinal spacing all halve: should it then enter RI=4, they would halve again. (Note that refraction for media with RI 3.4 or greater requires EMR wavelength in the 1200 to 16000 nm range, which is outside the visible light range. Thus the RI=4 statistics are a hypothetical extension to demonstrate the trend).

With a conservative estimate of 92,000 FER contained within the helix of a light ray having a wavelength of only 589 nm, the size scale and numbers of these very small structures is quite astounding. However, atomic Physics is used to ultra-small dimensions, with the CS estimate for proton radius being about 10^{-15} m (compared with the STEM estimates in the order of 10^{-11} m), which is the same order of magnitude as the lateral spacing of FER in a light ray. However, despite the extreme smallness of these intricate structures, and the huge numbers of FER involved, STEM's statistics would seem to be no more outlandish than the statistics suggested for a range of sub-atomic particles by CS.

The fun side of the change of the speed of light with the RI of different media is some of the intriguing visual distortion created by light refraction (such as in figure 8) and the polarisation of reflected and refracted light, all of which is addressed in the next chapter.

Figure 8: Distortion Effect of Light Refraction

Light Refraction, Reflection and Polarisation

When light passes obliquely from a fast medium (e.g. air, RI=1) to a slow medium (e.g. glass, RI=1.5), the **angle of incidence (Θ)** of a light ray is greater than the corresponding **angle of refraction (Φ)** for refracted light in the denser medium. When a light ray is reflected, the **angle of reflection** is equal to the angle of incidence, as shown in figure 9. All three rays (incidence, reflected and refracted) lie in the **Incidence Plane**. Snell's Law (or the **Law of Refraction**) links the angles of incidence and refraction via the RI (n) of the media involved as: n1 * sin (Θ) = n2 * sin (Φ)

Snell's Law is most useful as it can reliably be applied to link the angle of incidence (Θ) and refraction (Φ) to the refractive indices of the two media involved. However, despite the reliability and usefulness of Snell's Law and the **Fresnel Equations** (to be discussed shortly), the mechanics of light refraction and reflection represent some of the least-well explained aspects of EMR transmission.

Light refraction is often explained, quite inadequately, in terms of changes in the speed of a group of light rays within a beam: e.g. in terms of a group of wave-like monochrome light rays or using the analogy with a line of marching soldiers. All such explanations involve a change of direction of a group of in-phase light rays, but fail to explain why single rays of light bend (i.e. refract) rather than simply slowing down and continuing at the new slower speed in the same direction as the incident rays.

To add complications, some light rays, or parts thereof, are refracted while others are reflected, with all refracted and reflected rays undergoing a degree of polarisation. Although 'lines of marching soldiers' analogy falls well short, the STEM approach explains these phenomena quite well. However, first the geometry associated with a FER-helix ray of unpolarised light encountering a medium with a different refractive index needs to be examined.
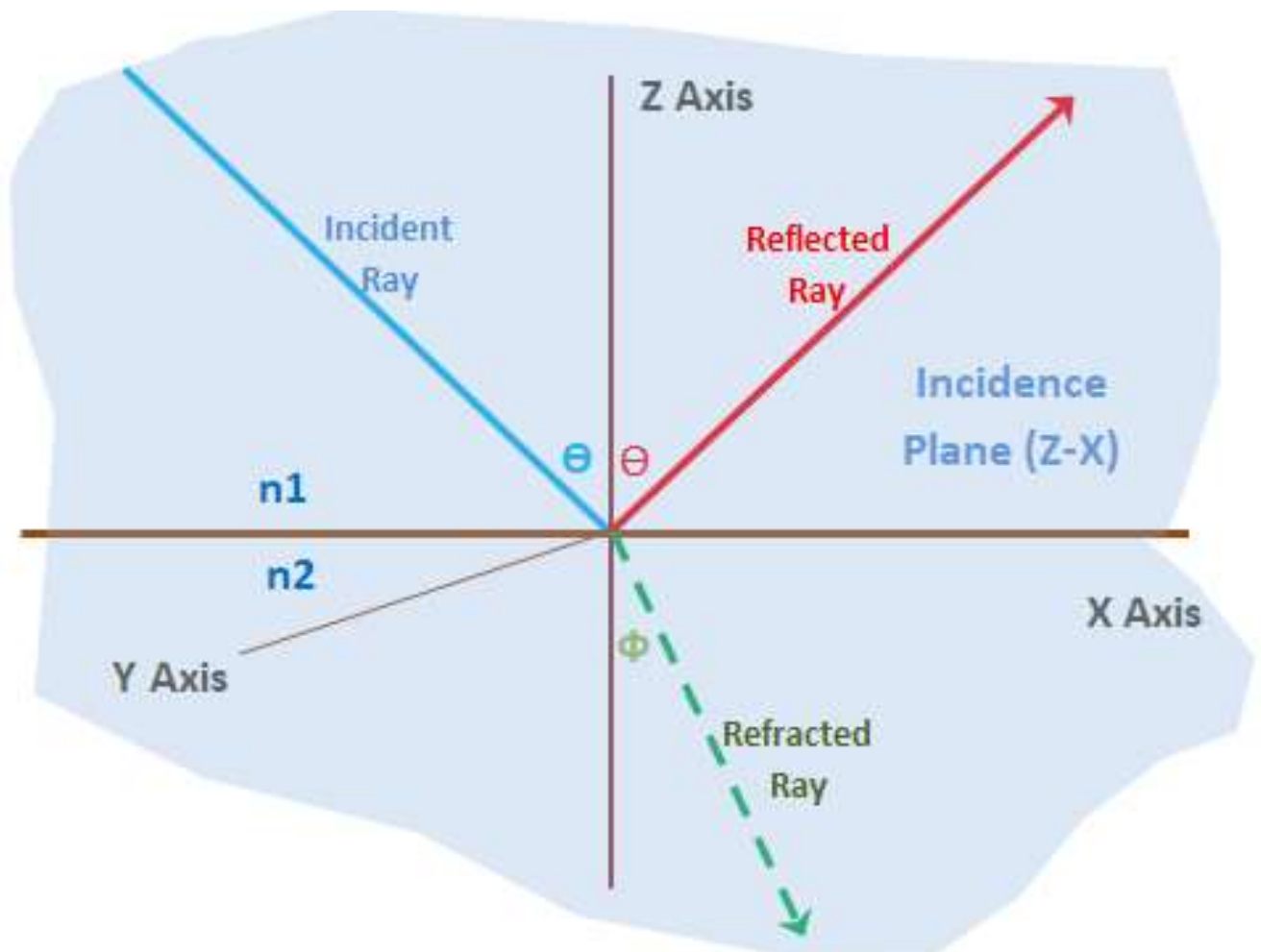

Figure 9: Reflection and Refraction (n1 < n2)

Referring to figure 10, for an unpolarised light ray with left-handed chirality, the FER members of the helix trace an elliptical shape at the interface surface, which is called an **incident-ellipse**, the long axis of which is dictated by the angle of incidence. The FER strike sequence around the incident ellipse is clockwise (A→B→C→D) because the helix is being viewed from above. If viewed from below, or looking towards the direction of the light source, then it would be an anti-clockwise movement as shown in figure 4d. For a right-handed helix the order would be anti-clockwise when looked from above as shown.

The long (or major) and short (or minor) axes of the incident ellipse are labelled AC and DB respectively. Because there is no change in the orientation of FER spin axes for an intact FER helix within the incident helix, the spin planes of all the FER still intersect at the centre of the incident ellipse (compare the top graphic figure 4c with the top-right ABCD graphic of figure 10). With their **electric field** component being parallel to the spin axis direction, the electric field of FER arriving at the interface surface at or close to incident ellipse locations **A** and **C** will be close to perpendicular to the incidence plane and combine to present as **s-polarised** (labelled ⊥) **sub-rays** of the originally unpolarised light. FER arriving at **D** and **B** have electric fields that are parallel to the incidence plane (but are not in it), and combine to present as **p-polarised (‖) sub-rays**.

The **arc zones** centred on the long elliptical axis points A and C thus combine to generate an s-polarised sub-ray; and those centred on the short axis points B and combine to generate p-polarised sub-rays. Because each type of polarised sub-rays can be variously reflected or transmitted, there are four distinct sub-ray types as indicated by the typical CS representations, such as the insert bottom-left in figure 10. However, as the angle of incidence increases, the long axis of the incident ellipse increase, with the A and C arcs becoming sharper and reducing in extent, and the D and B arcs broadening and flattening out. These changes to the geometry of the incidence ellipse have implications for the ratio of p to s polarisation; the reflected to refracted ratio; and amount of poorly polarised light.
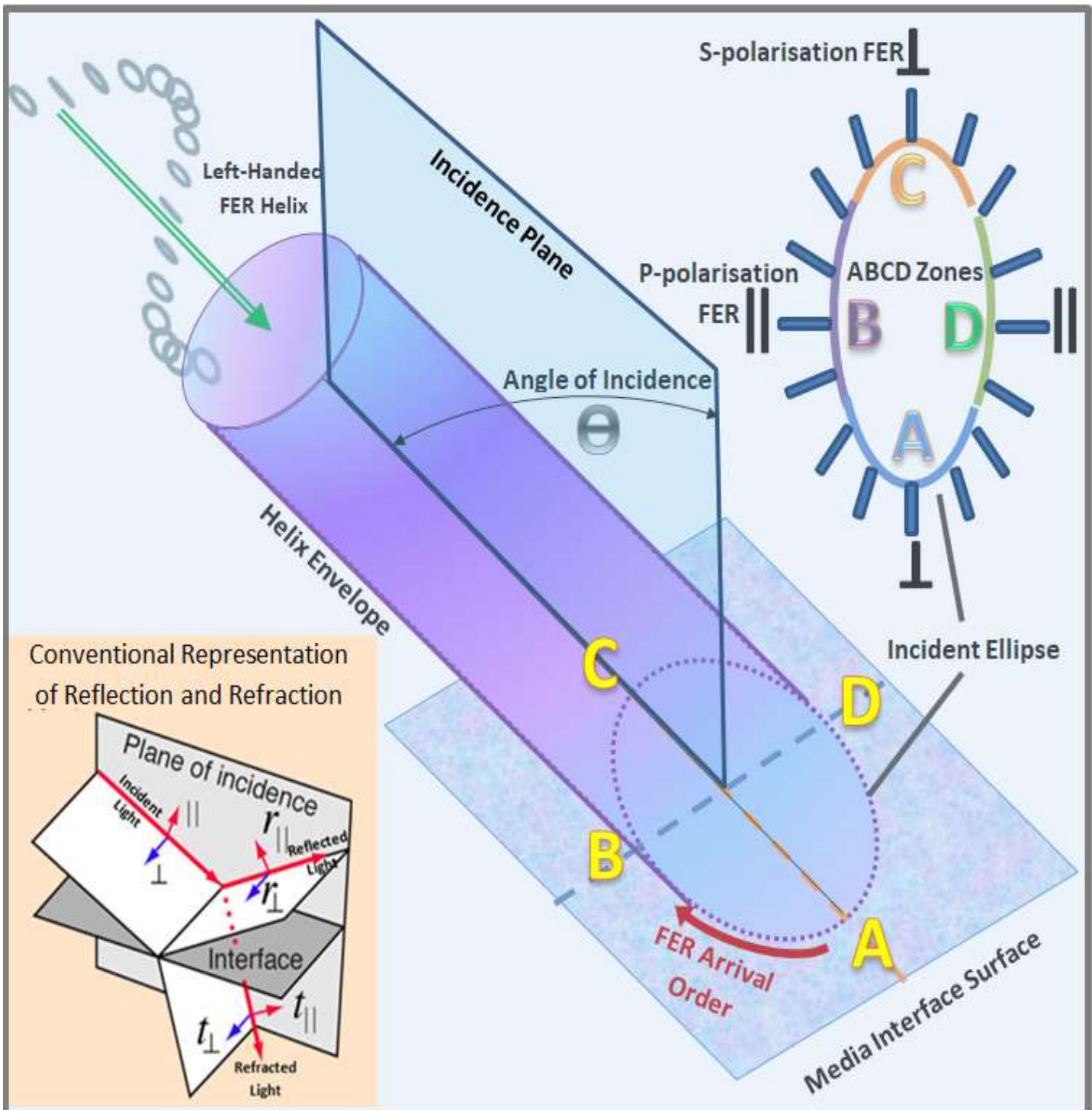

Figure 10: The Incidence Ellipse Implications for P and S-Polarisation of a Light Ray

Figure 11 is the STEM representation of the more conventional reflection and refraction diagram of figure 9. It shows a cross-sectional view of a single incident ray within the incident plane. Point **Q** represents the point at which a FER is encountering the interface plane: it corresponds with point **C** on the ABCD incidence ellipse. Although there is currently no FER at point P, which is diagonally opposite point Q, PQ represents the incident ray's wave front. Point **X** corresponds to point **D** of the ABCD incidence ellipse, with QX equating to AC, the long axis of the incident ellipse.

It should be noted that, although the incidence/refraction angles shown in figures 11 and 16 are true representations (i.e. with no angular distortion), the wavelength of the light ray and the diameter of the FER helix are severely scale-distorted, which can be quite misleading. Specifically, the helix's wavelength (5.89×10^{-7} m) is about 4,500 times its diameter (13×10^{-11} m) whereas, for figure 11, the wavelength is shown as being only 4 times (approximately) the diameter of the helix. To put this into perspective, should the helix diameter be represented by a mid-range human hair thickness (a nominal diameter of 80×10^{-6} m), then that hair would have to be 36 cm long (approximately double the A4 width of this page) to be a true-scale representation of one wavelength.

As FER within a light ray enter a medium with a higher RI, they will slow down due to the increased impedance encountered. The first point of entry around the perimeter of each FER is suddenly slowed down, so creating a temporal pivot point, with some of its linear momentum converting into angular momentum that causes it to change its travel direction, which by convention is the angle of refraction ($\emptyset$). By the time that each transmitted FER is fully immersed in n2, its forward velocity has been reduced appropriately, as it continues to travel in its new direction.

With transmitted FER moving slower (V2) than incoming FER (V1), FER travel closer together in n2 than they were in n1, with the ray's forward moving wavefront direction changing from PQ to XR. Within n2, the helix spire packing density has effectively increased, which results in increased levels of potential energy (due to increased mutual repulsion between adjacent same-charge FER) that can be released should a lower RI medium be encountered (as per the earlier explanation about how light speeds up as it enters a medium with a lower RI).

Referring to figure 11, as it takes the same time for the location P, which is the point diametrically opposite a FER arriving at Q, to travel distance PX that the FER that enters n2 at Q travels the distance QR. By geometry:

$$PX = QX \cdot \sin(\theta) \quad \text{and} \quad QR = QX \cdot \sin(\emptyset)$$
$$\text{Thus } V1/V2 = PX / QR = \sin(\theta) / \sin(\emptyset)$$
$$\text{and, because } V1/V2 = n2/n1 \text{ (by definition of n), we have Snell's Law : } n1 \cdot \sin(\theta) = n2 \cdot \sin(\emptyset)$$
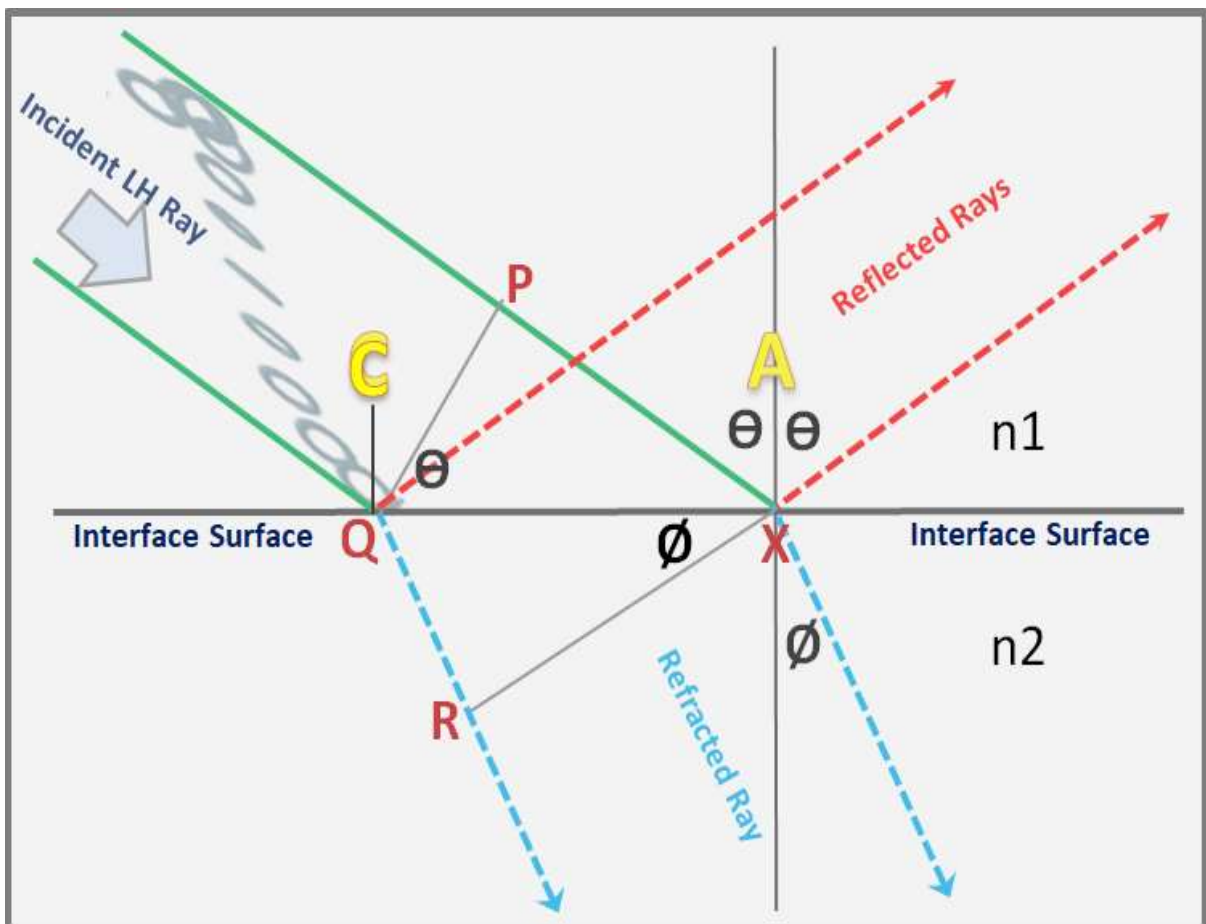

Figure 11: Reflection and Refraction (n1 < n2)

Certainly, compared with an equivalent CS equivalent explanation for refraction of light, the STEM explanation, based upon Newtonian Physics principles, is relatively simple and straightforward without the need for marching soldiers.

Unless it is travelling through a perfect vacuum (i.e. one free of matter and electromagnetic fields), light undergoes minor FER loss and/or slight damage to its structural integrity due to FER scattering and absorption. However, because within the length of one wavelength, a light ray contains about 92,000 FER, such loss and damage is relatively insignificant, with light rays still able to travel mostly intact over vast distances. Furthermore, rather than being fully reflected or fully refracted, when a light ray enters a medium with a different RI, the chaos that ensues results in ray splitting and polarisation, which are behavioural characteristics that are more statistical than prescriptive in nature.

Next, the nature and structure of **plane polarised light** (**PPL**), as derived in the form of p and s-polarised sub-rays, will be discussed, with the mix reflected and transmitted sub-rays will be addressed.

At the point of generation, **unpolarised photonic EMR** consists of FER that are equally spaced and moving together in a fixed-radius non-rotating helix, and whose spin planes intersect at the centre-line of the helix that coincides with the ray's centre of mass. **PPL**, on the other hand, consists of groups of FER whose spins are co-planar, with a fixed gap between groups. Adjacent FER groups have opposite spin direction so that, when the electric field of one group is negative (-E), the fields of the immediate adjacent groups on each side are positive (+E), as shown in figure 12a. When each FER in the PPL is exactly aligned, and each group contains the same number of FER equally spaced and separated by the same gap width, the resulting pure PPL generates a dog-toothed electric field signature as shown in figure 12b.
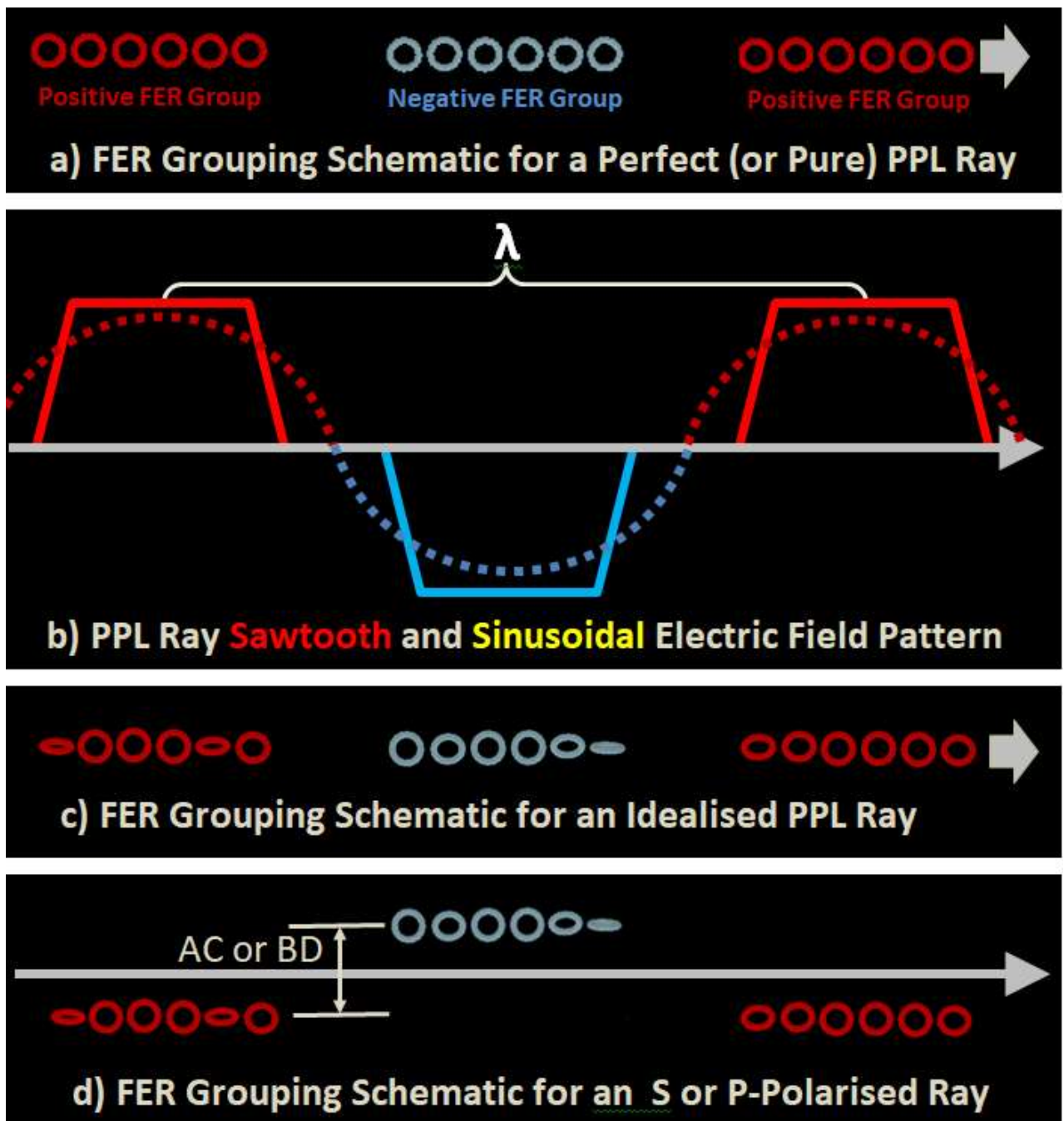

Figure 12: Plane Polarised Light (PPL) Structure and Electric Field Signature

However, **PPL sub-rays** generated by reflection and refraction are usually far from being pure (or perfect) PPL, with the alignment of end-member FER of each group being slightly oblique to the polarisation plane as represented in figure 12c. Such end-member variation does however result in a smoother sinusoidal curve pattern that is reminiscent of the sinusoidal signature of the unpolarised light from which it is derived.

The s-polarised sub-rays derived from the A and D-arcs combine to generate s-polarised sub-rays may be reflected or transmitted dependent upon the RI difference of the media and the orientation of the FER at the interface surface. The p-polarised rays may also be variously reflected or transmitted, which means that a single ray of light can generate up to four separate sub-rays of PPL as represented in the insert bottom-left in figure 10. It is not a case of either being reflected or refracted, s-polarised or p-polarised; with the chaotic nature of the reflection and refraction processes, many sub-rays rays will be partly (or poorly) formed, or even be missing altogether.

As for figure 10, figure 13 represents an incident ray with left-handed chirality. The side graphics labelled ①, ② and ③ show the orientation, spin and thus charge of FER arriving at the interface plane at locations A, B and C around the incident ellipse.

While FER are striking the interface plane in the **arc-A** area as in graphic ①, they have anti-clockwise spin when viewed from the arc B direction, and represent a group of s-polarised light with positive electric charge (+E). Graphic ③, central to **arc-C**, represents a similar process to that operating in graphic ① for arc A, except that the FER spin direction is clockwise and thus the electric field of the group registers as being negative (-E). These two planar-aligned FER groups together represent a sub-ray of s-polarised light: those more central in the A and C arc zones tend to be reflected as R_S (or $R_\perp$), whereas those more to the side of the zones tend to be transmitted T_S (or $T_\perp$). Furthermore, it should be noted that this pair of positive and negative groupings, whether reflected or refracted PPL, are laterally offset from each other by the incident ellipse's large axial length (AC) as represented in figure 12c.

Graphic ② shows the orientation for FER striking the interface plane in the **arc-B** area. These FER represent a group of p-polarised light with a positive electric charge (+E). The same process occurs in the arc-D zone with the electric field of the FER registering as being negative (-E). These two planar-aligned FER groups represent a sub-ray of p-polarised light: those FER more central in the B and D arc zones tend to be refracted (or transmitted) T_P (or $T_{||}$) sub-rays, whereas more to the side of the zones become reflected R_P (or $R_{||}$) sub-rays. In this case the positive and negative groupings are laterally offset by the incident ellipse's small axis length BD as shown in figure 12c.
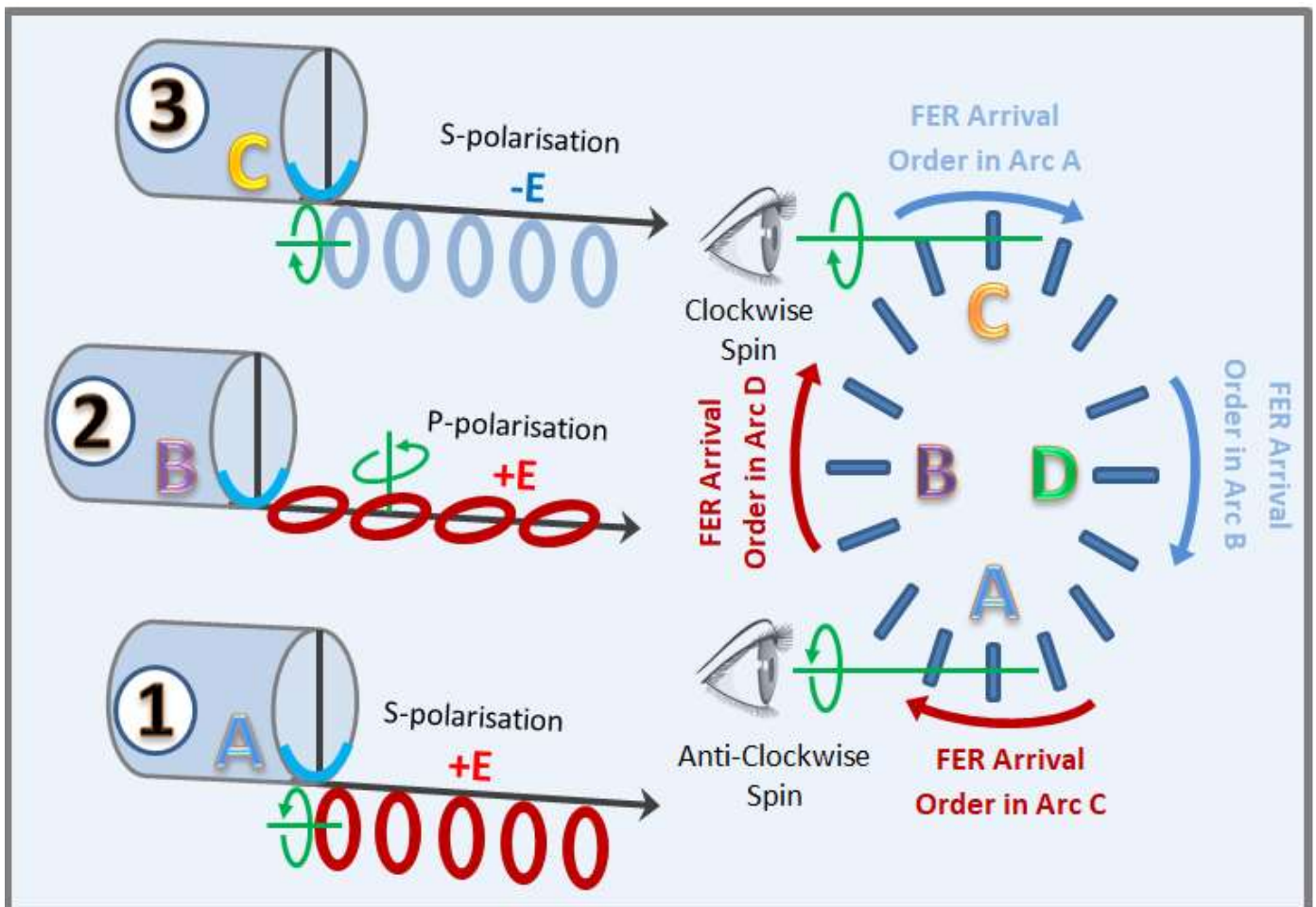

Figure 13: Plane Polarised Light Structure and Pseudo-Sinusoidal Electric Field Pattern

In way of a process summary, as FER from the helix spire enter a specific arc-zone regions of the ABCD incident ellipse, groups of positive or negative charge pulses are asynchronously generated from areas diametrically opposite each other (e.g. the A and C arc areas) of the ellipse to combine as PPL with the same frequency as the incident ray. The orientation of FER determines whether the polarised sub-rays are reflected or refracted, with their intensity being determined by the number and orientation of FER contained in their positive and negative FER groups. This simple geometry-based process converts one ray of unpolarised of light into the four types of polarised light $R_\parallel$, $T_\parallel$, $R_\perp$ and $T_\perp$ as represented in the CS insert graphic of figure 10. A [more complex equivalent mathematical explanation](#) can of course be found in Wikipedia for the CS interpretation.

In the region for which Snell's Law applies (angles of incident greater than about 5°), a mixture of reflected and refracted sub-rays are generated, with the mix of each and the nature of their polarisation being determined by where around the incident ellipse the incident FER encounter the interface surface. For angles of incident greater than the **critical angle**, where the angle of refraction becomes 90°, all light sub-rays are reflected and refraction ceases.

For angles of refraction less than the critical angle, due to their orientation, FER encountering the interface surface very close to A and C points (the long axis incident ellipse points) are always reflected as an s-polarised (R_S) sub-ray; and those and encountering the B and D short axis points are always transmitted as a p-polarised (T_P) sub-ray. These sub-rays are also reasonably well polarised (i.e. are much closer to being pure polarised than the other sub-rays).

The regions in-between the long axis arcs (A and C) and short axis arcs (B and D) represent change-over (or transitional) zones in which p-polarised sub-rays may be reflected (R_P) and s-polarised sub-rays may be transmitted (T_S), as represented by the colour-coded segments in figure 14 for a range of different angles of incidence (15° to 85°).
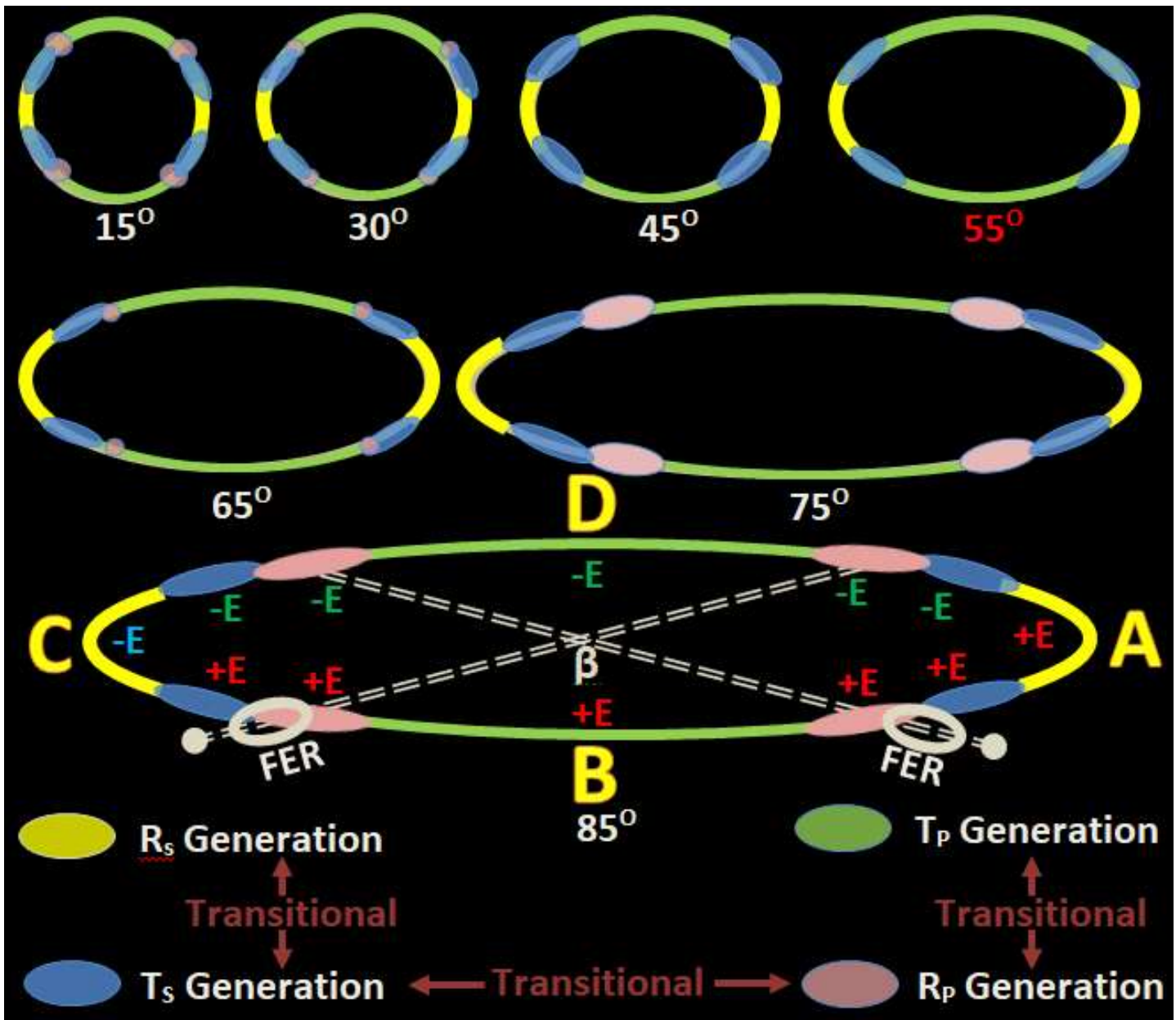

Figure 14: Polarisation Associated with Changes of Major Axis Length with Angle of Incidence

As the long axis AC lengthens, the ellipse becomes sharper (i.e. more pointy), whereas the short axis BD remains fixed-width with the ellipse becoming wider and more flattened in the B and D arc areas. The primary A and C-arc zones in combination are responsible for p-polarised light, with most of the centrally generated sub-rays being R_S, and those on the outer limits of these arc-zones, the so-called **transitional zones**, generate T_S sub-rays. Similarly, the primary B and D-arc zones produce predominantly T_P sub-rays, whereas their adjacent transitional zones produce R_P sub-rays.

Another aspect apparent in figure 14 is that the diagonally opposite pairs of pink zones (those connected by the double dashed lines in the 85° angle of incidence example) combine to produce two separate R_P sub-rays. Similarly, the diagonally opposite pairs of blue zones combine to produce two separate T_S sub-rays. Because of the transitional zones, STEM contends that up to **six sub-rays** may be generated (rather than the four suggested by CS), with three transitional zones (R_S to T_S, T_S to R_P, R_P to T_P) having been identified.

Because the two diagonally opposite transitional zone pairs are not parallel to each other (they are inclined to each other at the interface surface by the obtuse angle **β**, which is dependent upon the angle of incidence), the generation of transitional zone sub-rays is more complex and variable than for primary arc zone sub-rays. For certain lower angles of incidence transitional zones may generate low quantities or even no transient sub-rays: an example of this effect is the absence of R_P sub-rays for angles of incidence between 45° and 60° in figures 14 and 15.

Although there is a degree of natural variation involved in the reflection, refraction and polarisation of light in terms of the six sub-rays regimes, statistically, the Fresnel Equations (also known as the **Fresnel coefficients**) provide a means to quantify the mix of rays for varying angles of incidence, and do so quite reliably. Figure 15 is a mathematically determined idealised plot of Fresnel reflectance and transmittance coefficients for an interface between air and glass (assumed RI = 1.5). The **T** curves represent transmitted refracted light and the **R** curves the reflected light, with the subscripts indicating **S** or **P** type of polarisation.
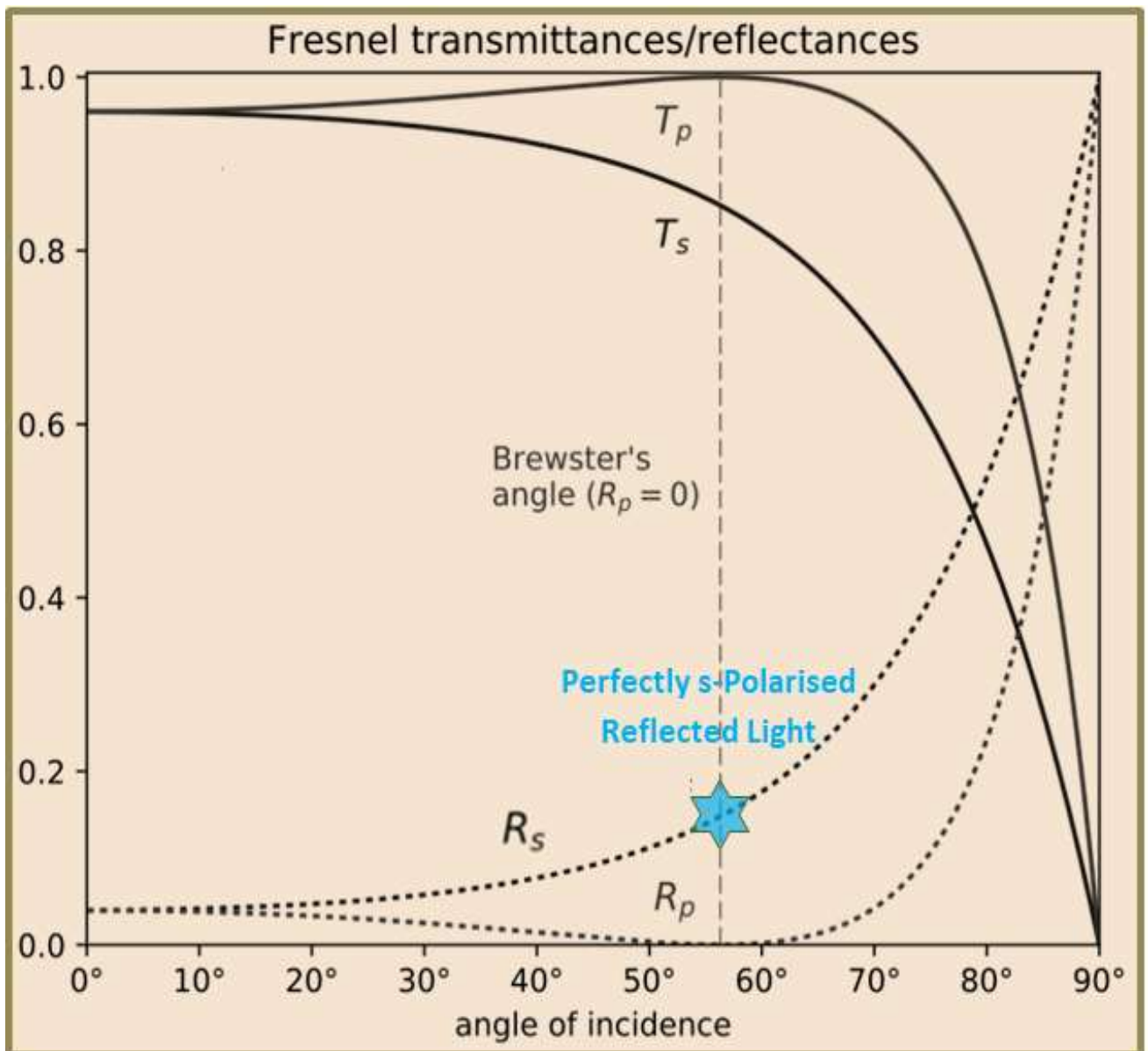

Figure 15: Fresnel Coefficients for an Air-to-Glass (RI = 1.5) Interface

The Fresnel coefficient plots indicate the relative changes of p and s-polarisation within both reflected and refracted light with changing angle of incidence rather than the ratio of p to s-polarisation overall. It is also worth noting that they make the unreasonable assumption that polarisation will be fully and perfectly p-polarised, or fully and perfectly s-polarised rays, with no rays being transitional between these two extremes. There is also no provision randomness or for scattering and absorption losses.

One pair of Fresnel coefficients plots the inverse relationship between R_S and T_S that is consistent with the relationship between the A+C arc zone R_S sub-rays and their immediately adjacent transitional zone T_S sub-rays. They also plot the inverse relationship between T_P and R_P that is consistent with the relationship between the B+D arc zone T_P sub-rays and their adjacent transitional zone R_P sub-rays.

Furthermore, the Fresnel coefficients plots indicate that, at low angles of incidence, only low proportions of R_S and R_P are generated, and that the R_S sub-ray component steadily increasing with the angle of incidence whereas the transitional zone R_P sub-rays steadily reduce to zero and stay zero for the 50° to 60° angle of incidence range.

As the angle of incidence (Θ) is increased, the angle of refraction ($\emptyset$) also increases, but is always less than the angle of incidence when n2 > n1. With both Θ and $\emptyset$ increasing, at some point $\Theta + \emptyset = 90^O$, with Θ being defined as **Brewster's angle (Θ_B)**. By geometry, Brewster's angle can be calculated as arctan(n2/n1), as shown in the derivation bottom-left in figure 16.

 Brewster's angle is important because, as can be seen in figure 15, it is central to a zone for which all the reflected light is R_S because the level of transient sub-rays has become zero. With virtually no contamination by the p-polarised light (i.e. no transitional R_P), reflected light associated with Brewster's angle is as close as possible to pure PPL that can be derived from the reflection/refraction process, and is often referred to as being 'perfectly' polarised.
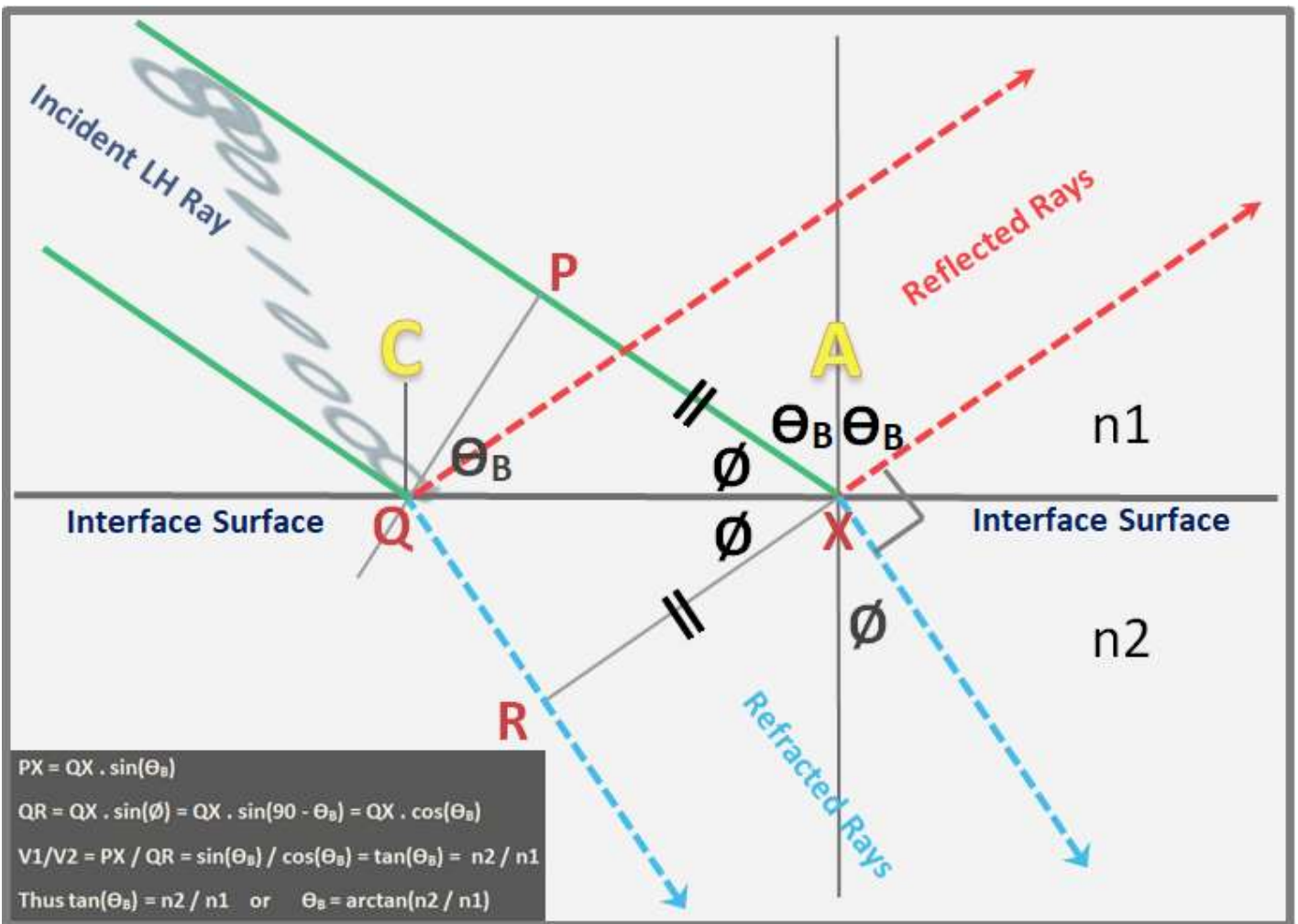

$PX = QX \cdot \sin(\Theta_B)$

$QR = QX \cdot \sin(\emptyset) = QX \cdot \sin(90 - \Theta_B) = QX \cdot \cos(\Theta_B)$

$V1/V2 = PX / QR = \sin(\Theta_B) / \cos(\Theta_B) = \tan(\Theta_B) = n2 / n1$

Thus $\tan(\Theta_B) = n2 / n1$ or $\Theta_B = \arctan(n2 / n1)$

Figure 16: Reflection and Refraction at Brewster's Angle ($\Theta = \Theta_B$)

The figure 17 graph shows Brewster's angle (the angle of incidence θ_B) for a light ray travelling in air (n1 = 1.0) and entering various transparent media with RI in the 1.5 to 4 range in steps of 0.5, as indicated by the dots coloured red, yellow, green, orange, blue and pink. The angle of refraction $\emptyset$ (shown as the lower red graph of figure 17) is the complementary angle of θ_B. These two graphs converge at an angle of incidence of 45° at n2 = 1, which is air-to-air transfer, a situation for which there is no interface and thus no refraction or reflection.
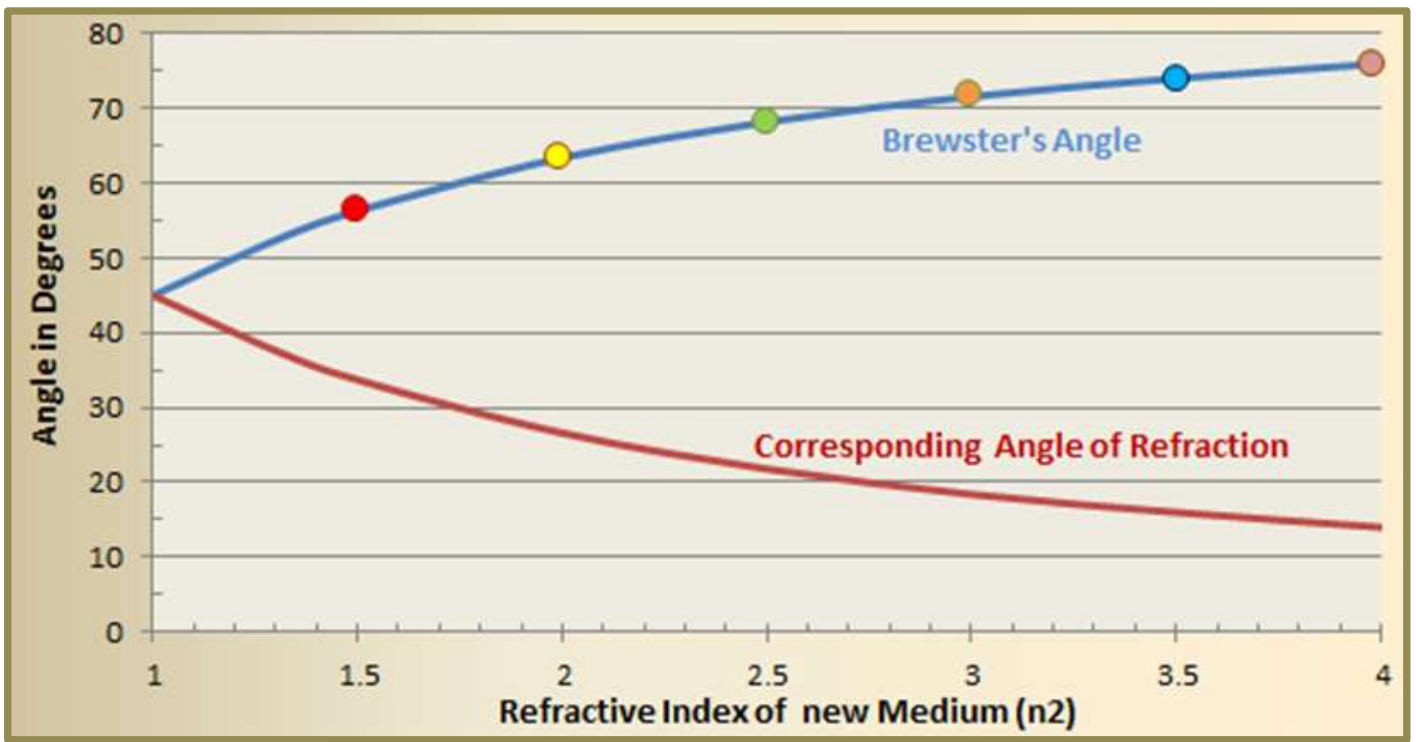
Figure 17: Brewster's Angle Variation with Refractive Index

Figure 18 shows the variation of the length of the incident ellipse's **major axis** in pm (1 pm = 10^{-12} m) for changing angles of incidence. It assumes that the helix diameter of 130 pm (or 13 x 10^{-11} m as per the statistics of figure 7c). The **blue shaded region** highlights Brewster's angle appropriate to RI's in the 1.5 to 4 range (the colour dots corresponding to those on figure 17).
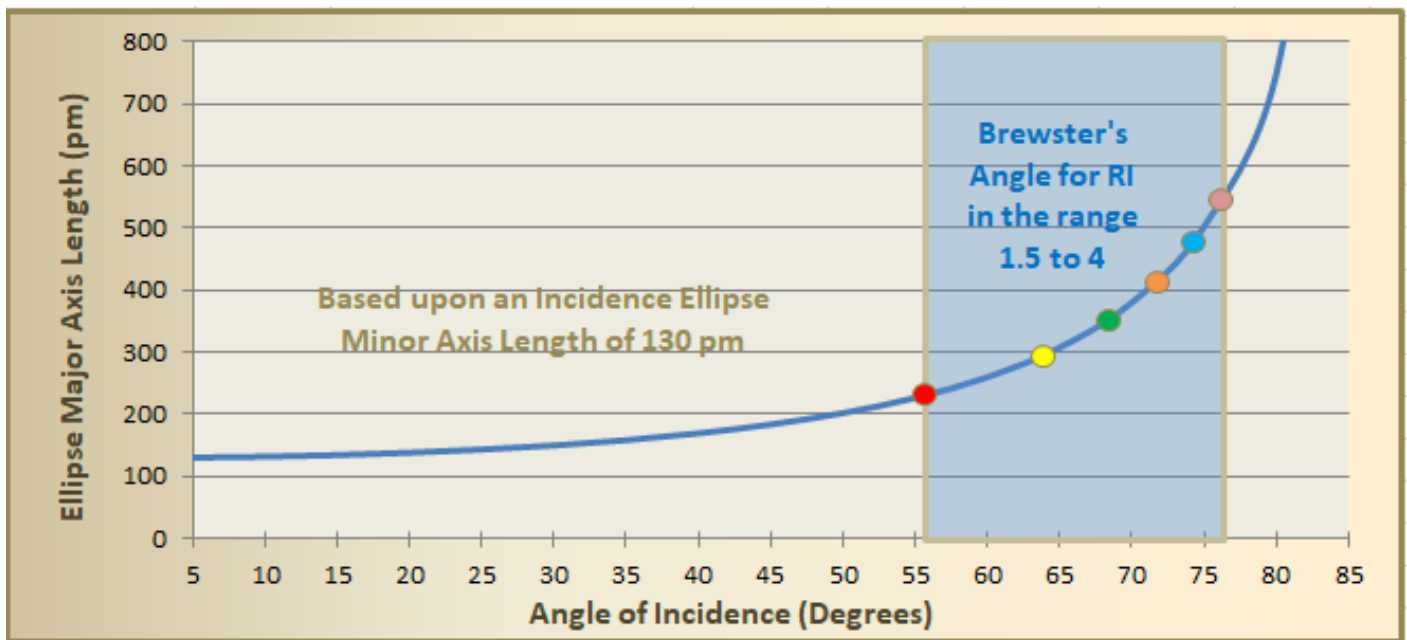

Figure 18: Incident-Ellipse and Brewster's Angle

The Chromatic Dispersion of Light

Within the visible light range, EMR is proportionally refracted dependent upon its frequency (and thus its wavelength). The result of frequency-dependent refraction is [chromatic dispersion](), which can generate beautiful rainbow displays from suspended raindrops or from a prism as in figure 19. Dispersion raises the question as to '*why does the angle of refraction vary with light wavelength?* '
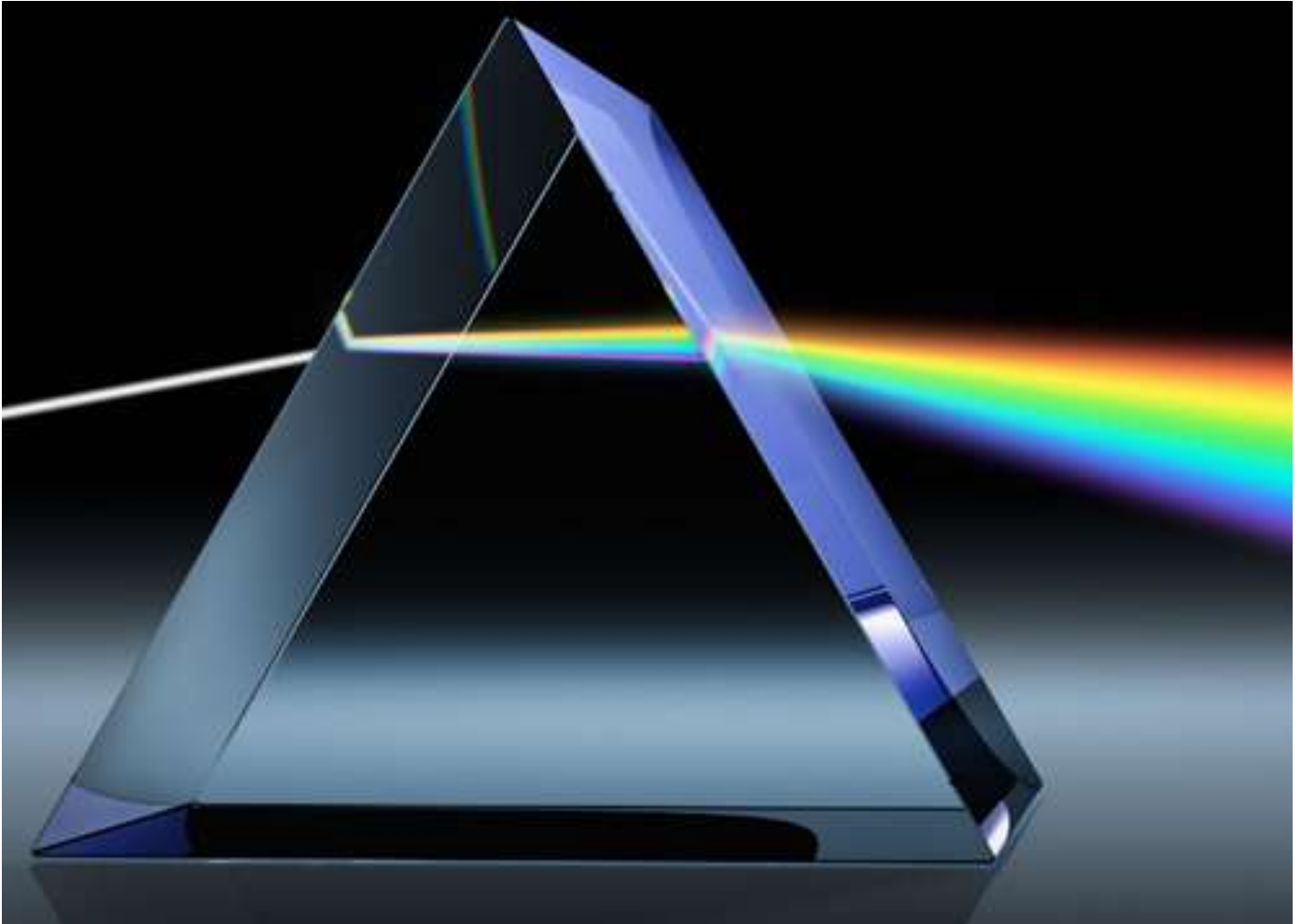

Figure 19: Chromatic Dispersion of a Light Beam

As the energy of light (and other forms of photonic EMR) increases, its frequency increases and its wavelength decreases, which results in an increase of FER packing density within light rays. The increase of FER packing density of higher frequency light produces increased stored potential energy between adjacent like-charge FER, which in turn marginally increases the angular momentum around the temporal pivot point as each FER enters n2, so increasing the pivotal swing and causing a slight reduction in the angle of refraction.

The net result is that, with increasing frequency of light, there is a corresponding **decrease in the angle of refraction** as it enters any given medium, which can be interpreted as being an **increase in n2** (i.e. the RI of the medium 2). As can be seen in the graphs of figure 20, within the visible spectrum, the apparent refractive index (RI) of transparent media reduces marginally as the wavelength of EMR increases (i.e. the apparent RI increases as frequency increases). Light rays having different wavelengths are thus refracted with different angles of refraction, which in turn causes a rainbow-like chromatic separation and dispersion.

Within the visible light range, the change of the angle of refraction with a change of frequency is only in the order of 1%, which is quite small. It is amazing that such small percentage change of the angle of refraction can create brilliant rainbows that can arch across the sky or the beautiful colour separation by a prism such as shown in figure 19.

FER are derived from an electron's field energy that becomes detached as the electron undergoes a series of rapid 360° flips as it moves and settles into a new stable orbital. When an atom becomes energised its the ionic EM field becomes stronger, which increases the inwardly directed motor force that an orbital electron experiences, and it moves inwards, spining rapidly and gaining speed until a sweet point is found and its new orbital can be established. Its new dynamically defined orbital has a reduced radius and the electron continues to spin as the fine adjustment of

its orbital takes place leading to stability being established.The more the atom is energised, the smaller the new orbital radius and thus the higher the frequency of the emitted EMR.

Higher frequency EMR thus has higher FER packing density and a smaller FER helix diameter, which means that it is more focussed with a higher energy density. Higher frequency EMR can thus deliver more enrgy more quickly as exemplified by the kinetic energy of photoelectrons by light frequency plots of figure 5 (see the Photoelectric Effect and Planck's Constant chapter). For lower frequency light, the width of its FER helix is often greater than the the target area so that, even for a direct hit with an atom, less of its FER energy can or will be absorbed.
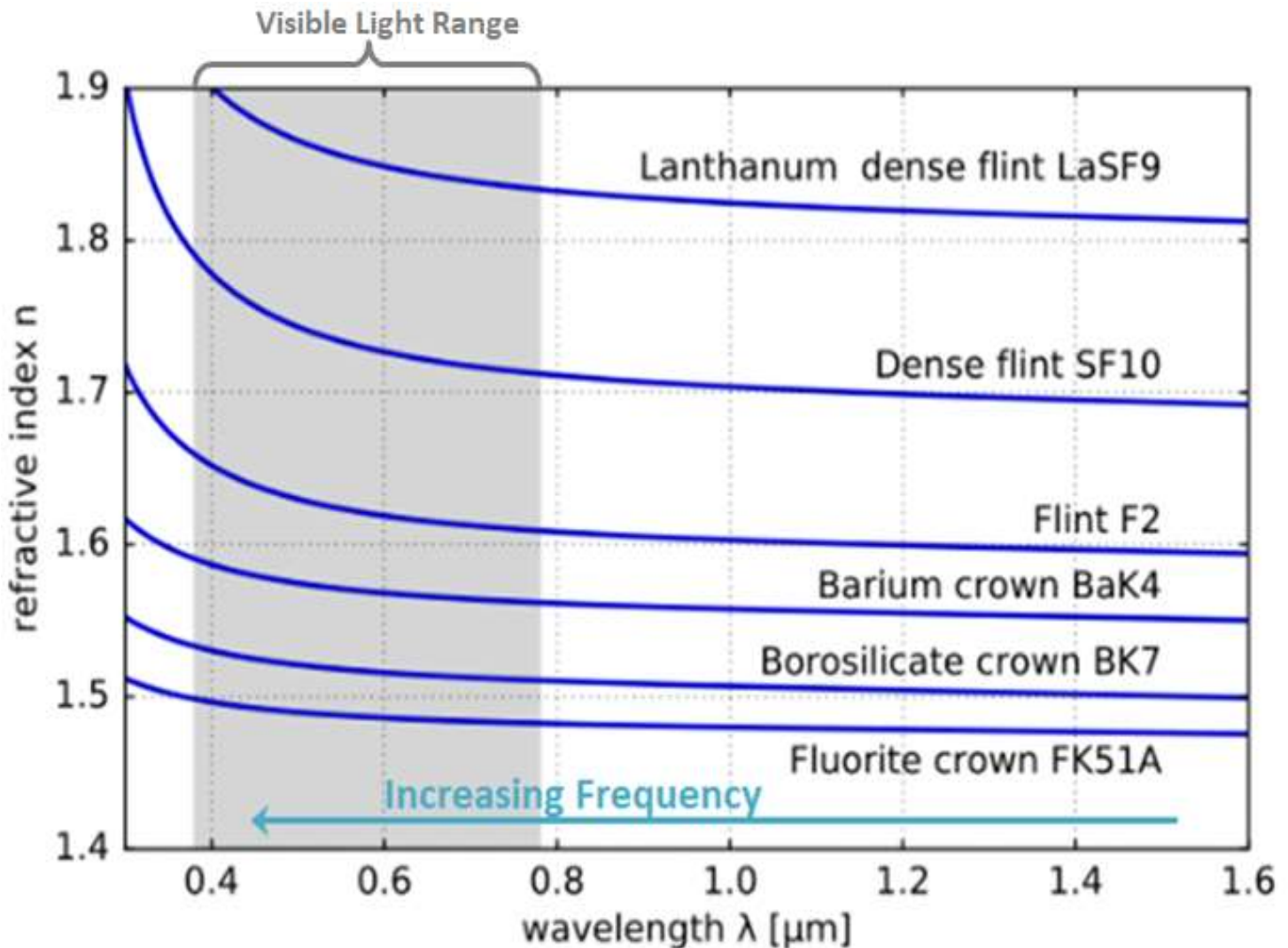

Figure 20: Change in Refractive Index by Wavelength (and Frequency)

As evident in figure 20 for a range of transparent material, with increasing frequency of light, there is a corresponding an apparent increase in n (the refractive index) that is related to the stored potential energy between FER rather than just the change in the speed of the light. However, across all frequencies there are several **regions of anomalous dispersion**, as shown in figure 21. There are three anomalous dispersion regions, each involving a sudden reduction in the RI, with the RI steadily increasing in between the anomalous zones.

Figure 21 is an idealised representation of anomalous dispersion across the entire EMR frequency range, drawing together results from various experiments involving a range of transmission media and environments: the variations are far from well defined in reality and, as such, the graph should only be considered to show broad trends. Within the visible light region (the V-region), the trend is for RI to increase with frequency, but the rate of increase more in keeping with 1% increases of figure 20 which is considerably less than those suggested by figure 21.

STEM, however, suggests that while **V** , **U** and **X** ranges are photonic EMR, the **I**-range spans and encapsulates non-photonic EMR (i.e. manmade radio waves as addressed in the Micro and Radio Waves chapter) which could contribute to the the ω_{IR} anomaly.

For the start of the U and X regions, the anomalous dispersion regions cause the RI to drop below 1, but only fractionally so. For example, the drop below 1 of X-rays for water is in the order of 2.5 x 10^{-7}, which is very small (well below the 1% level) but is still detectable.
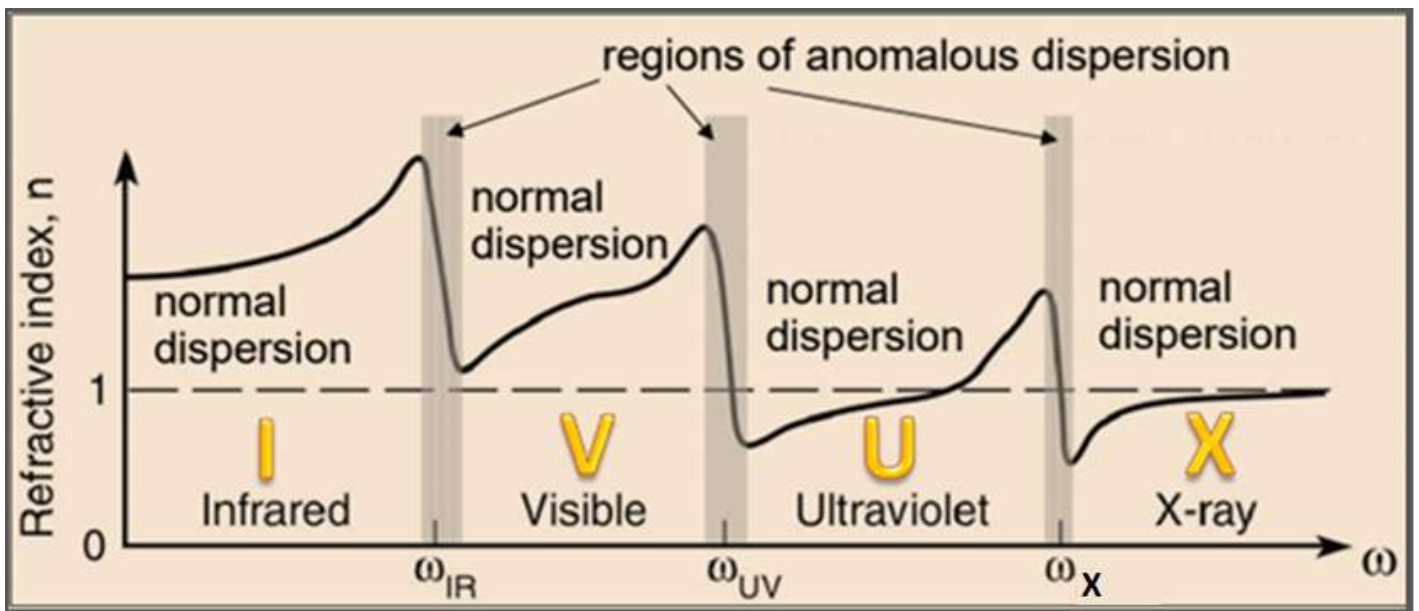
Figure 21: Light-Frequency Dependent Angle of Refraction

X-rays (the **X**-range) are commonly produced in X-ray tubes or synchrotrons by accelerating cetrons (negative CC) through a potential difference to strike a target such as a tungsten plate. As the kinetically-energised electrons enter the plate they start to tumble and slow down, they generate X-rays by the braking effect (bremsstrahlung) of the metal's atoms. X-rays are thus considered to be concentrations of field energy released as energised tumbling electrons violently rip into and are deflected by the electromagnetic field of the target medium's atoms.

Thus, although compatible to FER-based photonic EMR generated by generated from ionic electrons, a compreeion and reduction in FER size (but not FER energy) could be expected for X-rays, which would accommodate very high packing density levels. Also, should a highly energised electron make a direct hit of an atomic nucleus, it can generate spikes corresponding to one or more of that atom's spectral emission lines. CS contends that dispersion anomalies are due to when EMR frequency corresponds to natural frequency resonance points of particular electron orbit frequencies (unspecified), which could well be true.

X region gamma rays are thus possibly a product of radionuclide decay or, in smaller amounts, by the electron–positron annihilation phenomenon. The result in RI close to or possibly marginally less than 1 like X-rays.

Similarly ultraviolet light generation technologies are different to the generation of light in the visible light frequency range. There are various gas discharge lamps (e.g. xenon lamps and xenon/mercury lamps), excimer lamps, laser-induced plasmas as well as a range of ultraviolet lasers. Thus the structure of the U-Zone EMR would have a different physical structure and related statistics, including its own range of RI as shown.

Circular and Elliptically Polarised Light

Each positive and negative pulse within a plane polarised light (PPL) ray consists of a group of same-charge FER and, for perfectly polarised PPL, the spin axis of each FER is commonly aligned, with the toroidal spin of their field-energy helping to keep them all aligned as they move as a ray. For diagrammatic and discussion purposes related to circular and elliptically of polarised light, it is convenient to represent each positive and negative electric pulse within a PPL ray as a larger composite **FER group** called a **g-FER**, as represented in figure 22. The g-FER is fictional and used to simplify diagrams: it considered to have an electric and magnetic field strength equal to the sum of all its FER-group members.
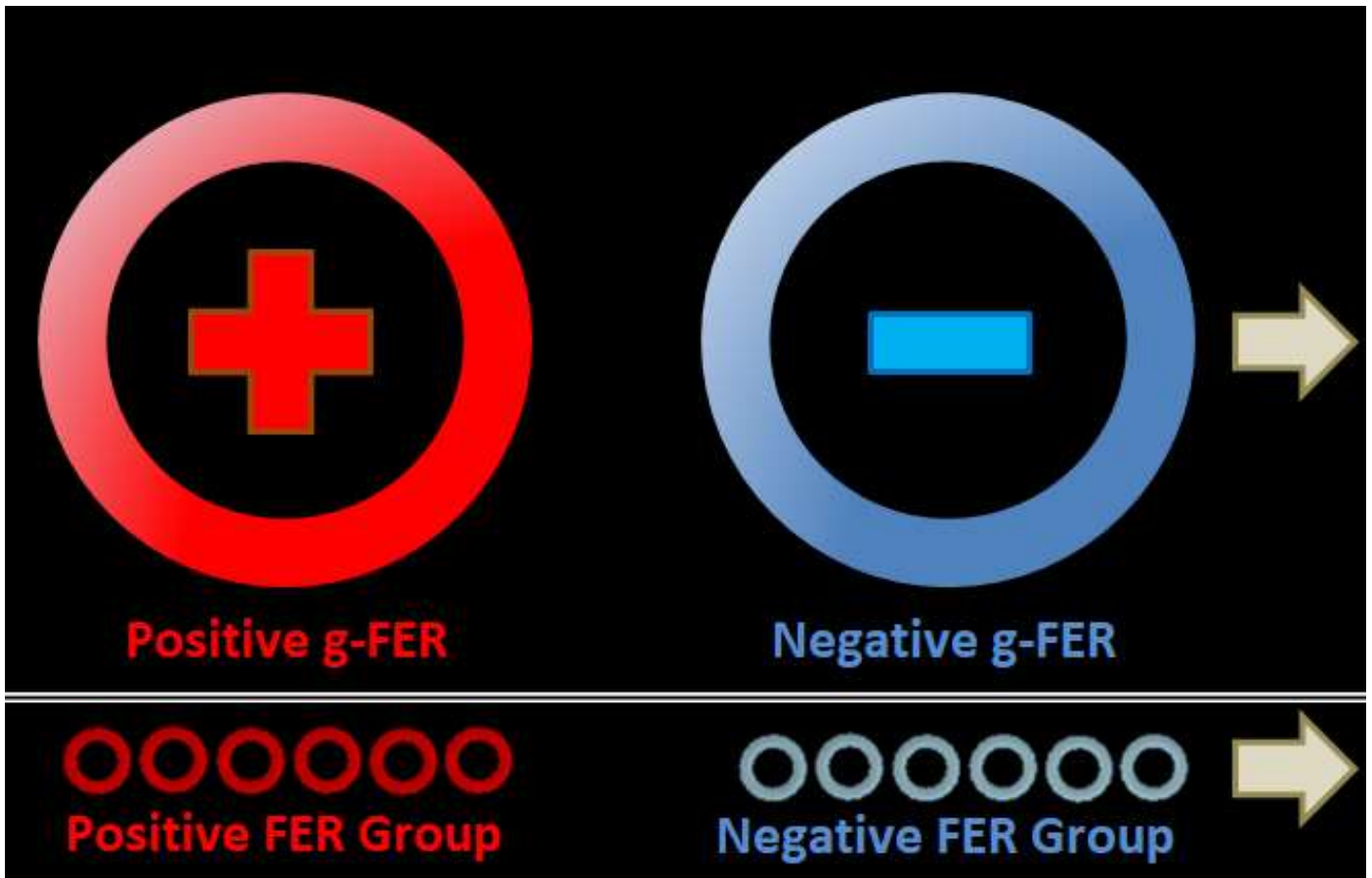

Figure 22: g-FER Representation of a FER Groups within a PPL Ray

When a ray of unpolarised light propagates through a [birefringent medium](#) (e.g. a Calcite crystal), it is split into two polarised rays whose polarised electric field planes are orthogonal, as shown in figure 23a. **Birefringence** is due to an **anisotropic** atomic structure within the lattice-like structure of a crystal that, for a calcite rhomb crystal, can generate a double image such as shown in the image right.

One of the split rays, the **ordinary ray**, acts as if it is passing through an **isotropic** medium, and its exit point is unaffected by rotation of the medium around the direction if the incident ray. The other ray, the **extraordinary ray**, is locked into the one structural plane, and thus its pathway moves circularly as the crystal is rotated around the direction if the incident ray.

For such optically anisotropic materials, the atomic structure dictates the direction of travel and the polarisation process, with FER being stripping off an incident ray's helix to create **two sub-rays** (T_S and T_P) in which FER orientation is restricted to two orthogonal planes. With the refractive index being slightly different for each direction of travel, there is a **phase offset** of the two emerging sub-rays dependent upon the distance travelled. The ordinary ray is defined as the sub-ray that takes the shortest direct route. By carefully selecting the thickness of a birefringent material, a **quarter-wave plate** can be created that will produce a **$\pi/2$ phase difference** between the ordinary and extraordinary rays which, when the rays are merged as shown in figure 23b, present as a **left circular polarised light** (see figure 23c).

A wave plate that produces a phase difference of 3*π/2 generates **right circular polarised light** (see figure 23d).

Circularly polarised light develops sufficient **Spin Angular Momentum** (**SAM**) to cause nanoparticles to spin as shown in figure 32a, with left-handed CPL spinning them anti-clockwise and right-handed CPL spinning them clockwise.

For phase differences other than π/2 or 3*π/2, **elliptically polarised light** (EPL) is generated. EPL can also be produced with light with phase differences of π/2 or 3*π/2 but with different electric field amplitude. As for CPL, EPL may be left or right-handed.

When PPL passes through a quarter-wave plate with its axes at 45° to the polarization plane, the PPL converts into CPL; and for angles other than 45°, EPL results. The reverse process applies when CPL is passed through a quarter-wave plate, it becomes (re)converted into PPL.

Polarised light make so much sense when considered in terms of g-FER (re)packaging. With each PPL ray consisting of equispaced g-FER groups, when two PPLs with their electric fields perpendicular to each other and an appropriate phase difference are merged, with their FER spacing and orientation within g-FER remaining largely intact. However, their electric fields combine with the other g-FER to generate a left or right-handed helix shaped electric field.

Excellent animations of the electric fields that define PPL, CPL and EPL can be found at this [Edmund Optics site](#).
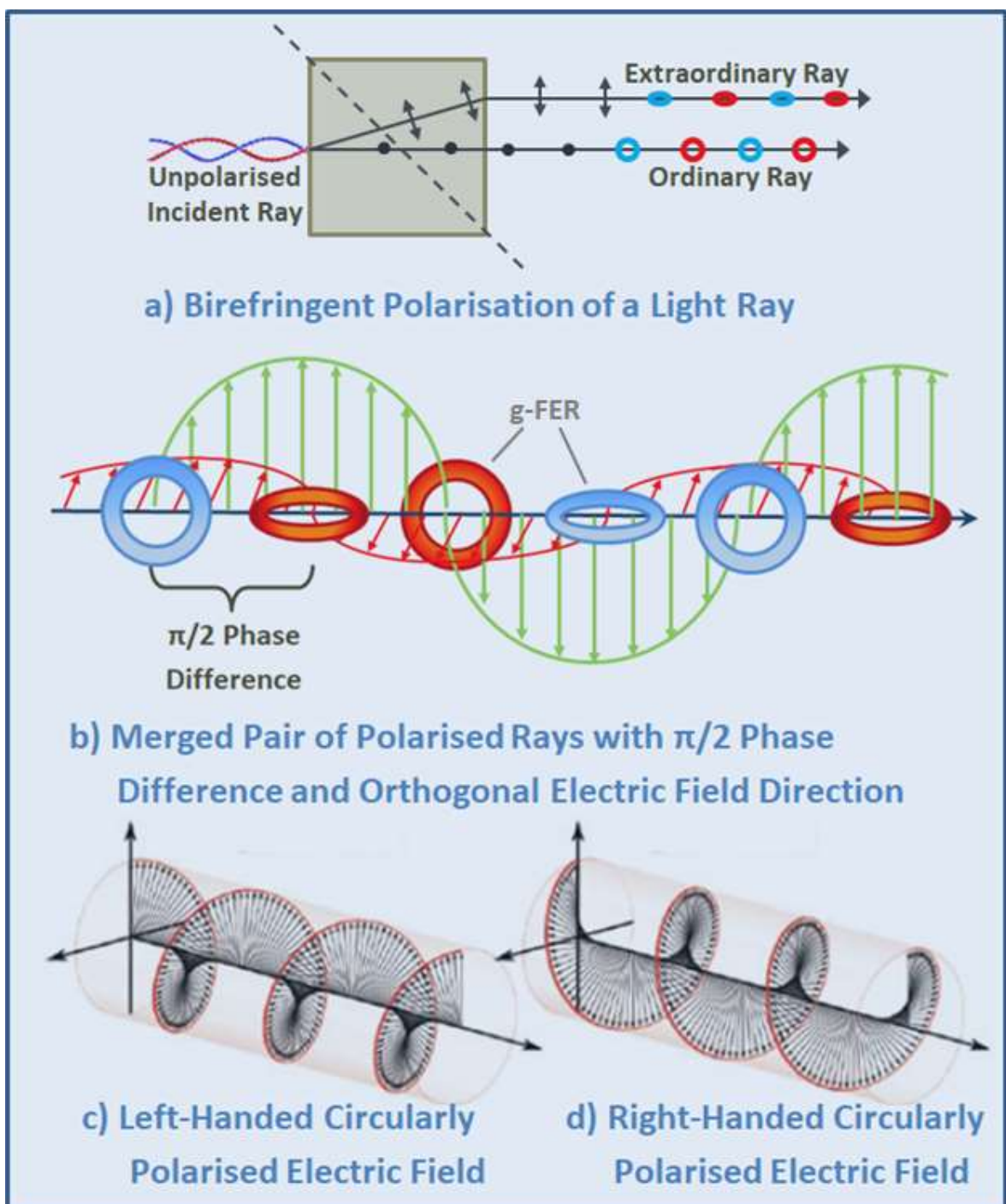

Figure 23: Birefringence and the Creation of Circularly Polarised Light

In figure 24, the separation between adjacent g-FER has been purposively increased for clarity, and electric field component lines have been added for g-FER and between g-FER to emphasise the spiral and chiral nature of the electric field components. As for figure 23b, figure 24a shows how a π/2 phase difference generates left-handed CPL rays; and figure 24b shows how a 3*π/2 phase difference generates right-handed CPL rays.

The **chirality** of circularly polarised light is **reversed upon reflection** from a reflective surface such as a regular metal/glass mirror. The reason why this occurs is that, should g-FER labelled A, B, C and D in the left-handed CPL of figure 24a be reflected by a mirrored surface (vertical double orange line), the reverse-direction sequence of the reflected ray is that of right-handed CPL as shown in figure 24b.
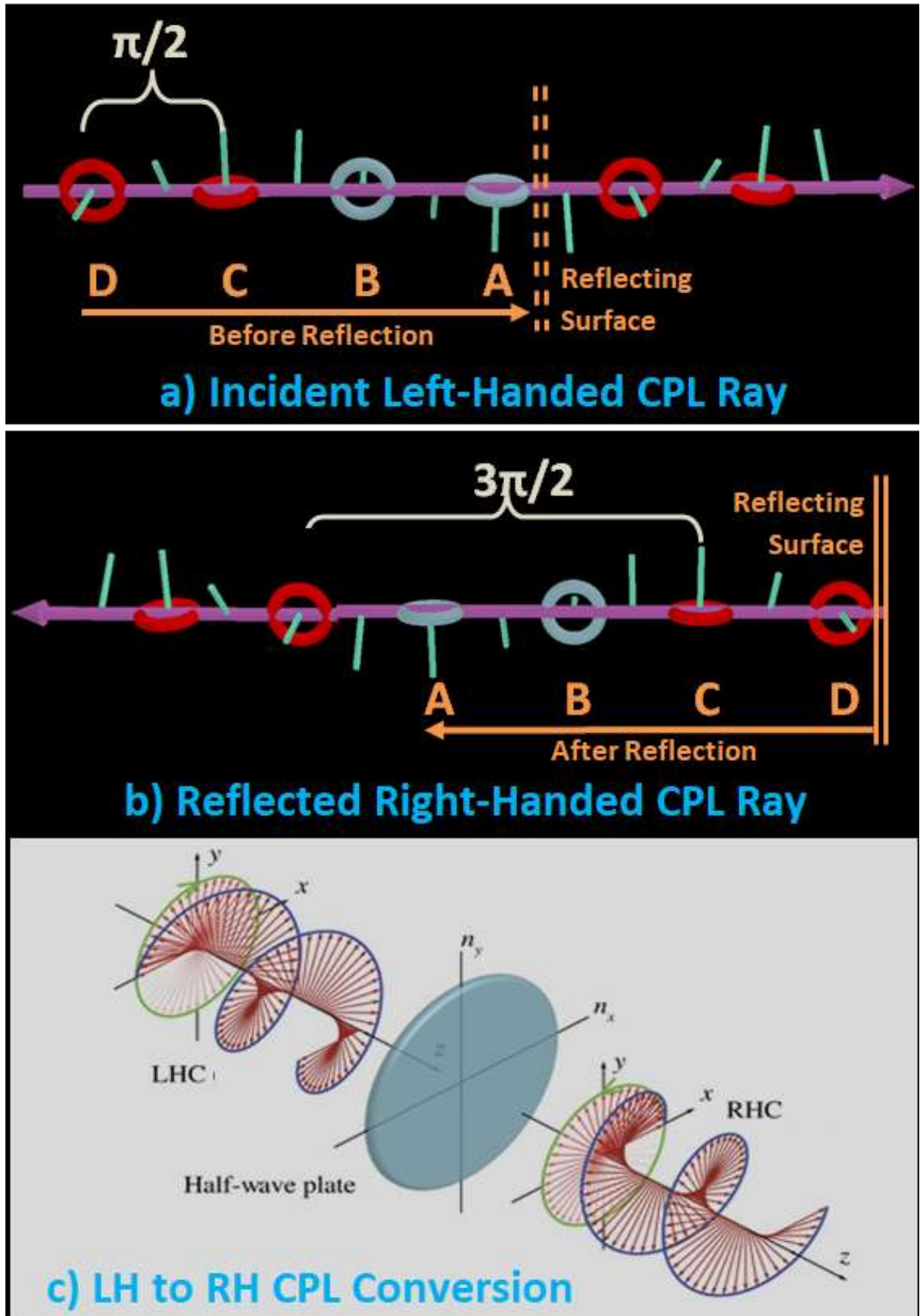

Figure 24: Left and Right-Handed Circularly Polarised Light

In addition, when left-handed circularly polarised light passes through a **half-wave plate**, it is converted into right-handed circularly polarised light as in figure 24c. Similarly, RH circularly polarised light can be converted into LH circularly polarised light. This is because the difference between LH and RH circularly polarised light is ±π. With the STEM g-FER approach, such transformations are mechanical and thus quite easy to describe and understand.

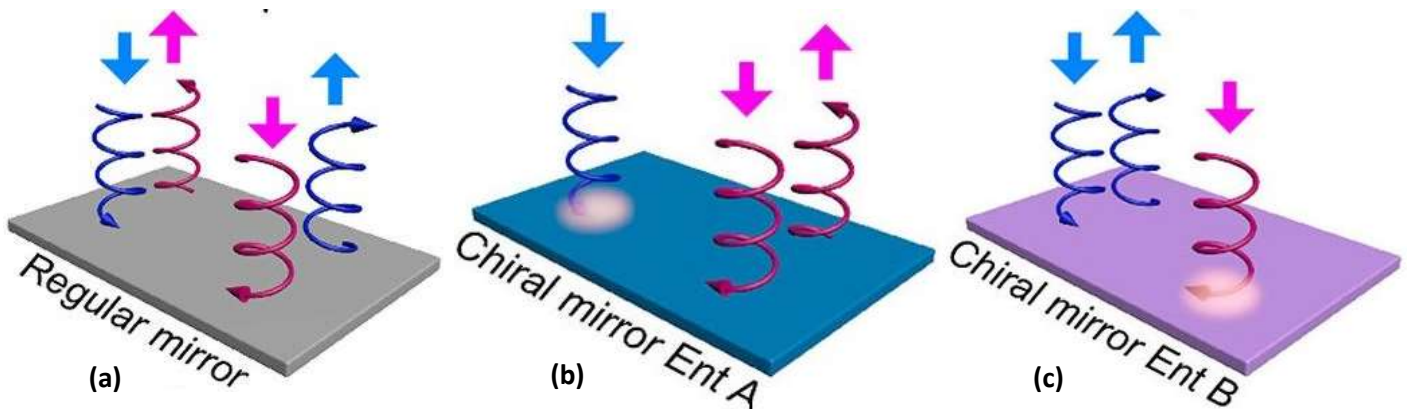*Figure 25: Reflection of Circular Polarised Light*

It is also worth noting that chiral meta-mirrors have been developed that reflect circular polarized light with the same spin of the incident beam, but only for one spin state; rays of circularly polarised light with the opposite spin are completely absorbed. Chiral meta-mirrors are available to reflect either right (figure 25b) or left (figure 25c) circularly polarized light, and do so without a change of chirality.

Constructive and Destructive Interference

As evidenced by the reflection of a light beam perpendicular to a non-chiral mirror, when light rays cross paths with each other, albeit obliquely or passing completely through each other travelling in opposite directions, due to their relatively low field-energy concentration, FER remain remarkably intact. Although the FER remain intact, the electric field components of FER combine to produce what is called **interference**. Interference occurs on a FER-by-FER basis, but because FER are evenly spaced within light rays, regular patterns of increased (constructive) and reduced (destructive) electric field interference develop, which is well understood and documented.

As shown in figure 26, simply, when the electric field signatures (W1 and W2) of two light rays, each with the same wavelength and phase, overlap, **constructive interference** occurs wherein the amplitude (R) of their net electrical field strength increases. When the phase difference of the rays is π (180°), they are completely out of phase and the net electric field is zero, which is called **destructive interference**. For any other phase difference, an irregular net electric field pattern, called **mixed interference**, results.
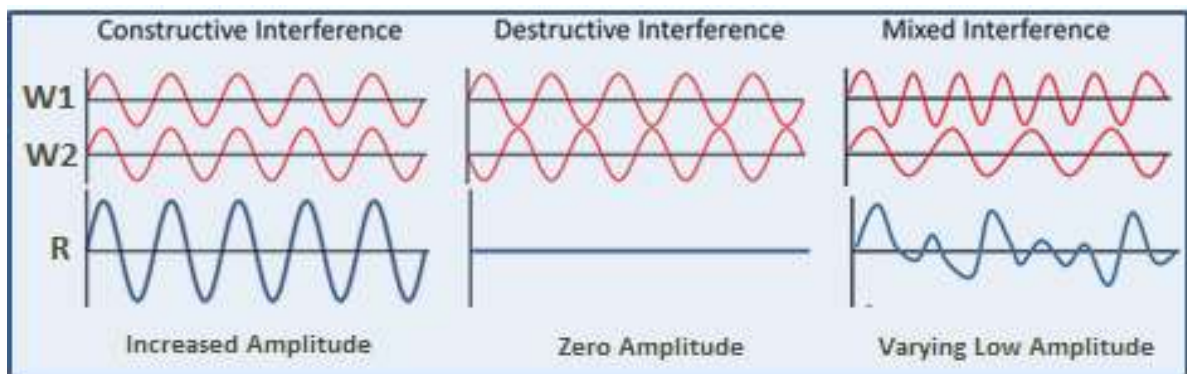

Figure 26: Constructive and Destructive Interference

The interference outcome is the same whether the light rays are travelling in the same or opposite directions. Thus, when light rays cross paths obliquely or head-on from any direction, multiple non-impact FER collisions occur without causing any significant physical change to any of the FER or the light rays involved. The only evidence of such

interaction is electric-field interference, which is temporal and only persists while the rays within light beams continue to cross each other's path in the same directional pattern.

Constructive and destructive interference is well demonstrated with the **Michelson Interferometer** setup for parallel merged beams as shown in figure 27. A single beam of **coherent light** (i.e. light with the same frequency and a constant phase difference) is split into two identical beams by a partially reflecting mirror beam splitter. Each of the split beams travels a different path to be re-combined before arriving at a detector, with their path length difference creating a phase difference between them, so producing a characteristic concentric interference pattern (figure 27a).
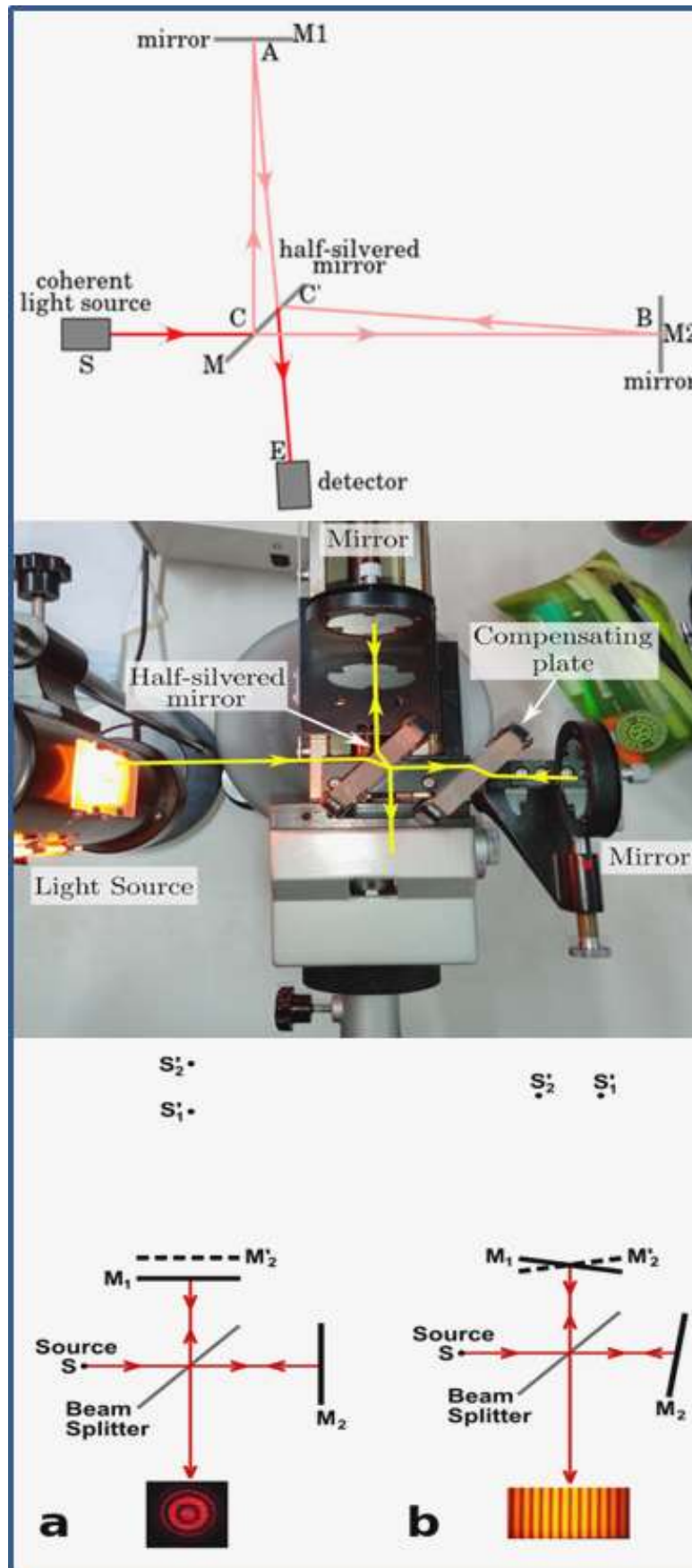

Figure 27: Michelson Interferometer for parallel merged beams

At the beam-splitting mirror M, approximately half the light is reflected towards reflecting mirror M1, where it is reflected towards the detector E. The rest of the beam split by M strikes reflecting mirror M2 and sent to the reverse side of mirror M (C[1]) where it is reflected towards the detector E. The interference patterns formed (figure 27a) are circular because the virtual images S1' and S2'of the light source form with one behind the other, and photons further from the centre of the beam travel fractionally further distances causing the interfere to vary radially. (Note that the mirrors used are metallic-backed which, even at angles of incidence of 45°, only generate small levels of polarisation).

For the inclined Michelson Interferometer setup, a slight angle between the two returning beams caused by the inclined mirrors M1 and M2 results in a bar pattern as in Figure 27b formed by the side-by-side virtual image (S1' and S2') being offset.

Whereas the way in which light rays are superimposed by the Michelson Interferometer are easy to explain, an explanation of the interference patterns generated for the single, 2-slit and multi-slit experiments is less obvious. The CS theory relevant to single slit interference is underpinned by the Huygens principle, which considers that each part of the slit opening can be treated as if it were an emitter of mini-wavelets. While the Huygens principle provides a mathematical basis for the development of the Fraunhofer diffraction and Fresnel diffraction equations, which help to quantifying the interference patterns for a narrow slit, there is no factual evidence or explanation relating to the existence of such wavelets: they are, literally and metaphorically, a gap-filler.

The material used to form the slit that is usually close to or slightly greater than, but certainly not less than, the wavelength of the incident light. The slit is usually machined into a metal plate, or into a stable substrate that is coated with an inert metal (often gold) to minimise surface chemical reaction and to ensure a smooth slit edging.

Localized Surface Plasmon Resonances (**LSPR**s) are collective electrical oscillations in metallic nanoparticles, especially gold, that are excited by light, and which exhibit light scattering peaks and strong electromagnetic near-field enhancement. LSPR fields are highly localized and decay away from the gold/air interface. A very important aspect of LSPRs is their light-intensity enhancement and localization means they have very high spatial resolution, and effects such as the magneto-optical effect (the Faraday Effect) are enhanced by LSPRs.
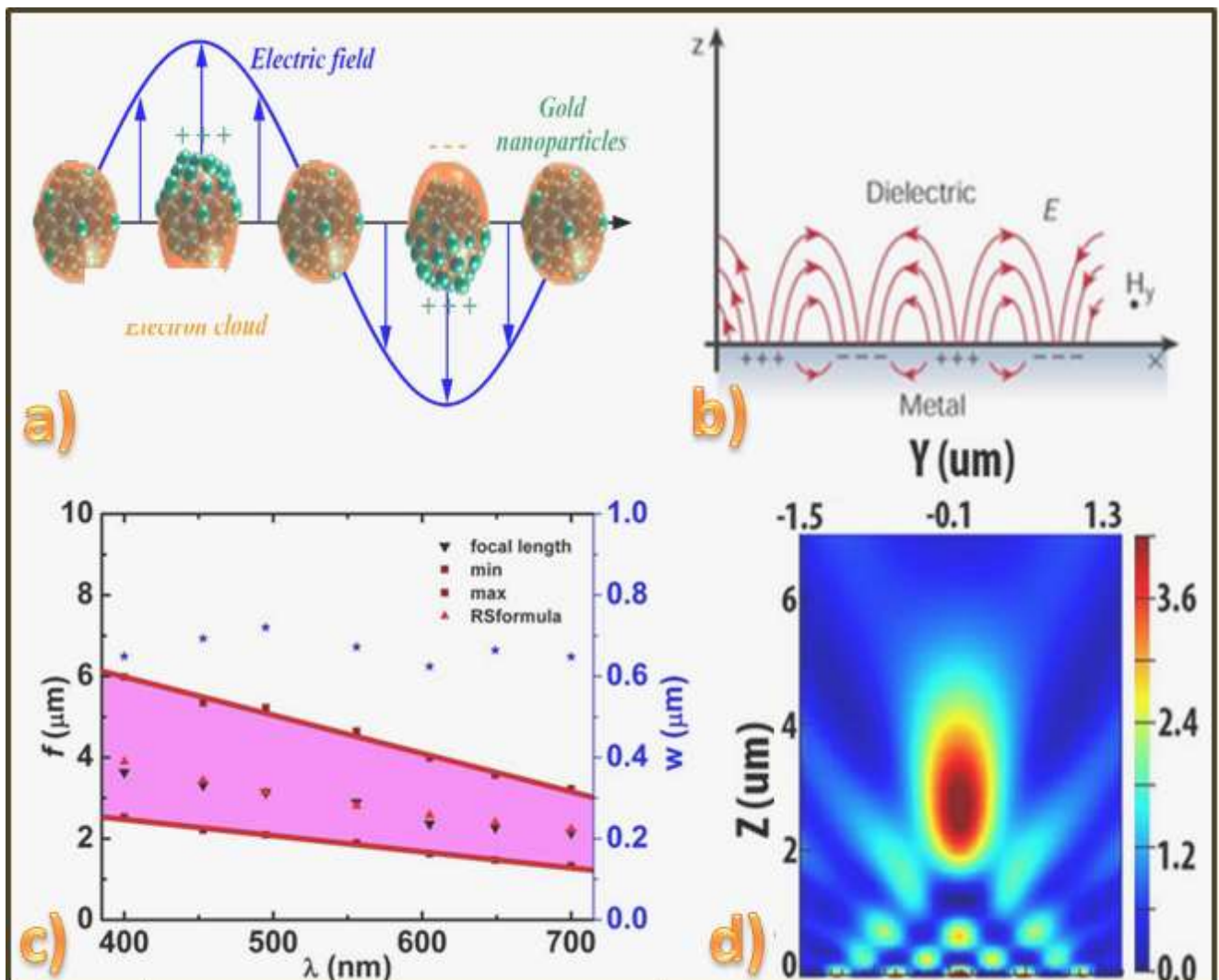

Figure 28: Surface Plasmons and Far-Field Scatter Effects

Surface plasmon polaritons (**SPP**s) are electromagnetic waves in the visible-frequency range that travel along a metal–dielectric (e.g. metal–air) interface. SPPs involve charge-motion in the metal (the surface plasmons) and electromagnetic waves in the air (the polariton aspect). SPPs are thus a type of surface wave, and are shorter in wavelength than incident light photons. Some SPP energy is lost to absorption in the metal with the rest scattering into free space. And importantly, when a SPP wave interacts with an irregularity, such as a surface corner or edge, part of the energy can be re-emitted as light.

Figures 28a and 28b are visualisations of surface plasmon electric fields. Figure 28c shows an emission profile at λ = 580 nm of a micro-hole lens using FDTD simulation from the 2014 paper by S. Saxena et al on Plasmonic Micro Lens ; and figure 28d a depth of focus plot (pink area) for wavelength ranging from 400 nm to 700 nm from the same paper. The micro-hole lens uses both the phenomenon of diffraction as well as surface plasmons to focus the incident light. It exploits the principle of superposition of the incident planar wavefronts and the diffracted non-planar wavefronts coupled to surface plasmon waves to generate high-energy concentration at the focal spot. This technology demonstrates the ability of SPPs to diffract (i.e. bend) and manipulate light and is thus very relevant to the slit experiments.

The diffractive effect of SPPs as FER pass through the slits is possibly related to electro-optic effects such as the Kerr Electro-Optic Effect; the electromagnetic drag on FER helices of light rays moving close to the sides of the slits; and the **far-field scattering** effect. All are factors that could contribute to the creation of curved wavefronts (figure 29) for light passing through a narrow **single slit**; particularly those coated with a metallic skin such as gold film.

LSPRs and SSPs were discovered in the 1960s, with well-established research available since 1970 leading to their widespread use for surface plasmon resonance spectroscopy and related nano-technologies. It is rather disappointing that the single and double-slit experiments have not been re-visited and re-interpreted, taking them into account.
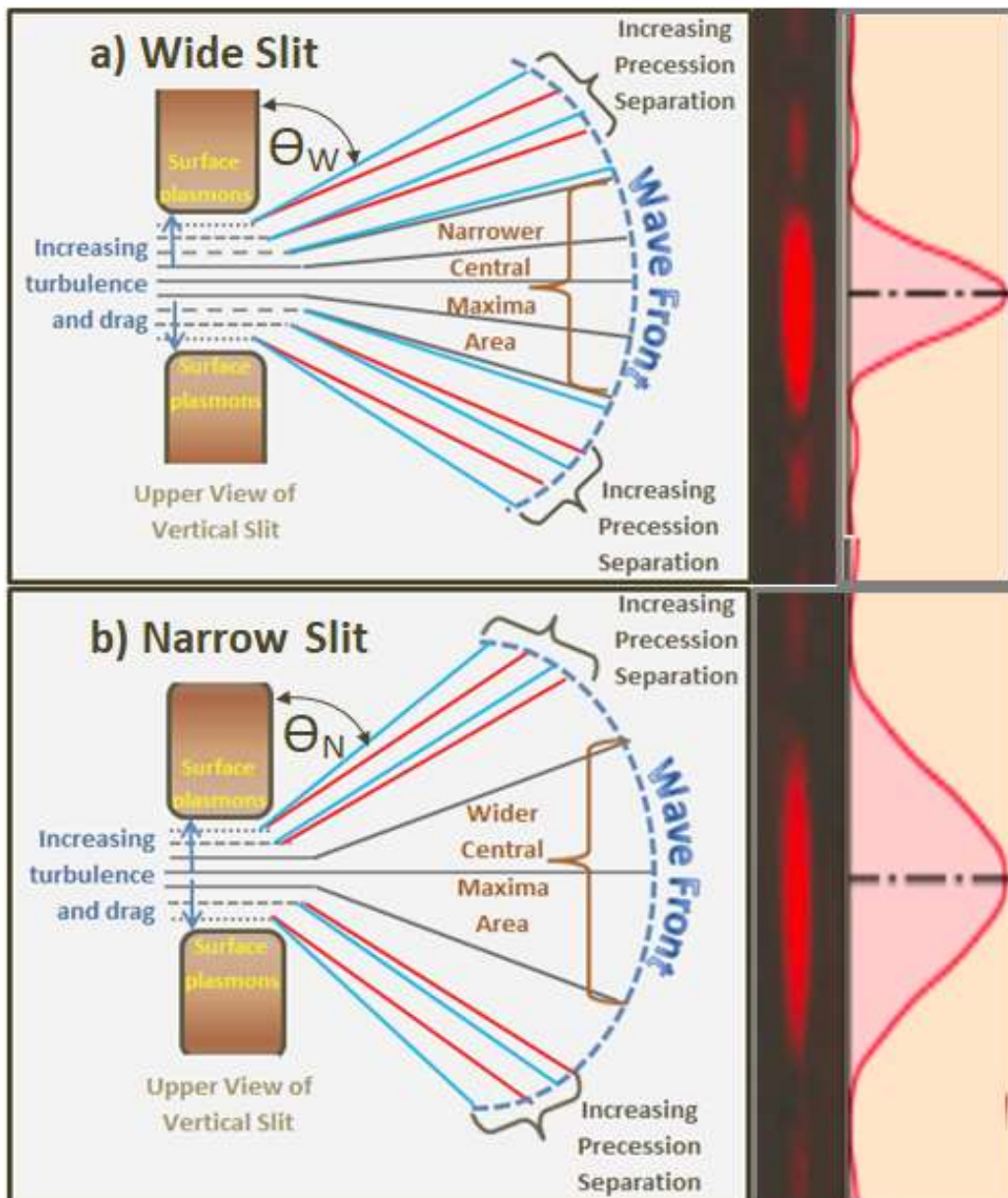

Figure 29: Single Slit Interference

Even without the possibility of significant light emission from SPPs, the LSPR fields create increased resistance to light rays passing close to the slit surface, which would progressively diminish towards the centre of the slit. In figure 29, the increased resistance, analogous to an increase in refractive index, is annotated as '*Increasing turbulence and drag*' and, closer to the slit surface it would cause the rays to spread and spread fan-like so as to generate a curved wave-front such as shown in figure 29.

The resistance increases closer to the sides of the slit a ray passes, increasing the bending and the chromatic splitting of non-monochrome light, and separation of the rays as shown in figure 29. The resultant interference pattern, either projected onto a screen or detected by light sensors, is an intense central band of light, and several diminishing repeat bands separated by dark, each separated by dark bands caused by destructive interference.

The minimum slit width to create banding is the wavelength of the light. The more narrow the slit, the larger the proportion of the rays that are diffracted and split, which widens the spread (i.e. widens the wave front, with $\Theta_N < \Theta_W$ in figure 29) to produce a wider central band.

As discussed earlier this chapter, several significant factors (LSPR fields, SPPs and surface irregularities) can contribute to the bending and splitting of rays passing through a slit. Huygens wavelet are assumed to be evenly distributed across the slit opening, whereas STEM contends that increased resistance provided by the sides of the slit, causes rays to slow down which, analogous to encountering a medium of higher refractive index, bends and splits the rays moreso the closer they are to the slit walls. Furthermore, the Huygens-Fresnel and Fraunhofer diffraction equations (referenced earlier) are considered to apply to both approaches despite these different initial assumptions.

Two-slit interference patterns (figure 30a) involve the interaction of two curved wavefronts (figure 29) from two separate slits intersecting and causing well-defined stipe-like interference patterns. The ray splitting associated with each slit still takes place, added to which are refracted rays from the other hole. Thus, the explanation of two-slit and n- strip interference patterns (figure 31b) logically follow from the single slit interference explanation, with the rays being deflected by the outer surfaces of the slits.
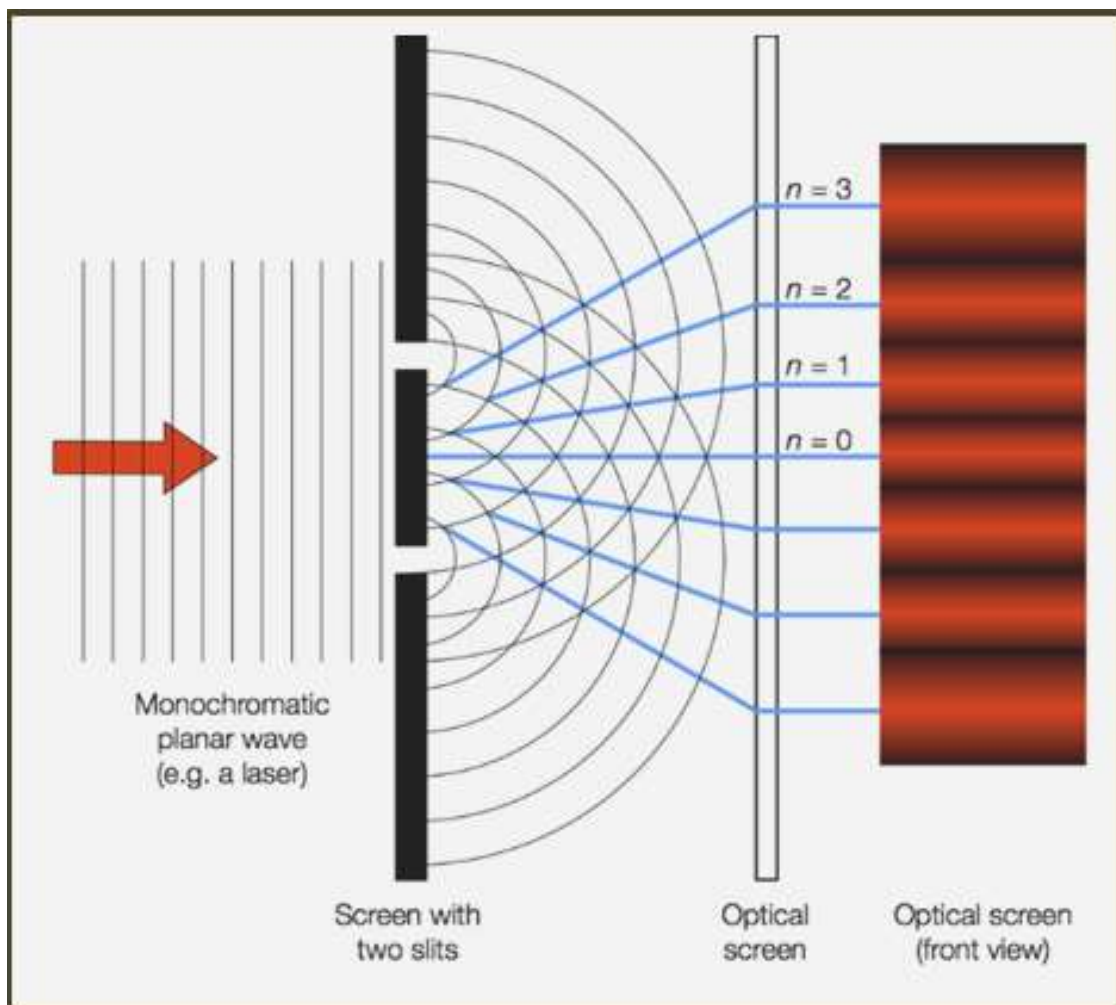

Figure 30a: Two Slit Interference

Many sites provide detail of the multiple slit experiments and the mathematics that has been developed for them. As the number of slits increase, the constructive interference patterns stabilise in size and intensity, as can be seen in the

seven slit example of figure 31b. As the number of slits increases, the interference patterns mimic the interference patterns produced by **diffraction grating**, which are formed by striations or fine ridges on a transparent medium.
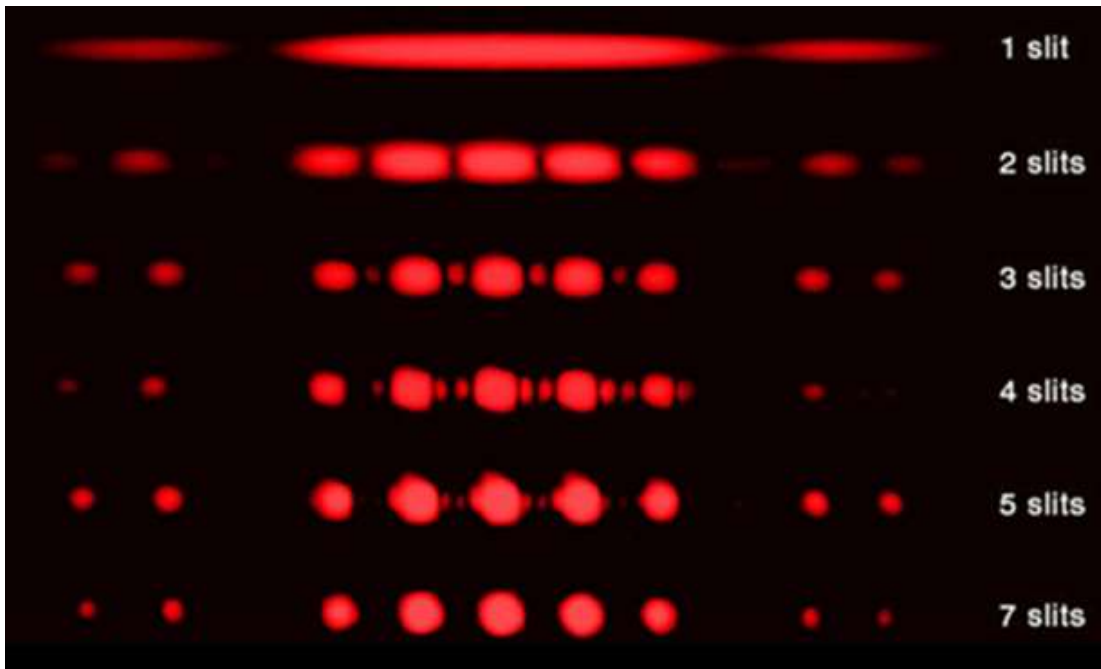

Figure 30b: Monochromatic Interference Patterns by Number of Slits

Due to **chromatic dispersion**, the interference pattern for **white light** is a series of rainbows as in figure 30c.
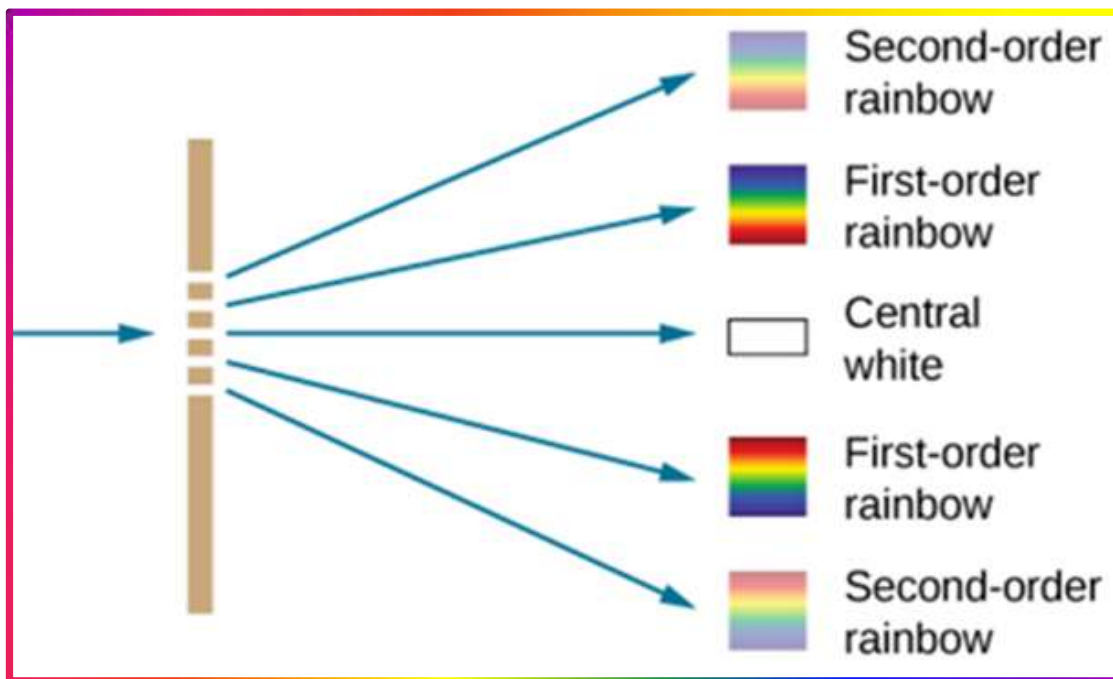

Figure 30c: White Light Dispersive Interference Patterns for a 5-Striation Diffraction Grating

The double and single slit experiments have been modified to include electrons and atoms as Quantum Mechanics seeks to extend wave–particle duality characteristics to other fundamental particles and atoms (i.e. matter).

An example of the single and 2-slit experiments involving electrons is the 2013 paper titled 'Controlled double-slit electron diffraction', by Roger Bach et al. This paper provides an excellent historical overview of the most significant experimental evidence on the subject since Richard Feynman's thought experiment concept. It is one of the few papers to provide full details (although the backstop distance is missing) of the setup for continual electron and single electron-by-electron accumulation, together with good clear presentation of the results.

The wall and mask (bottom right of figure 31) were constructed from 100 nm thin silicon-nitride membrane coated with approximately 2 nm of gold (which is an ideal medium for SSP generation), and the slits are 62nM wide and separated by 272nM.

100 nm

62 nm

272 nm

Distribution for
209 Electrons

Distribution for
1004 Electrons

Distribution for
6235 Electrons

**Experiment's Single Electron
Cumulative Distributions**

**Theoretical
Net Electron
Distribution**

**Experiment's
Enhanced Measured
Electron Distribution
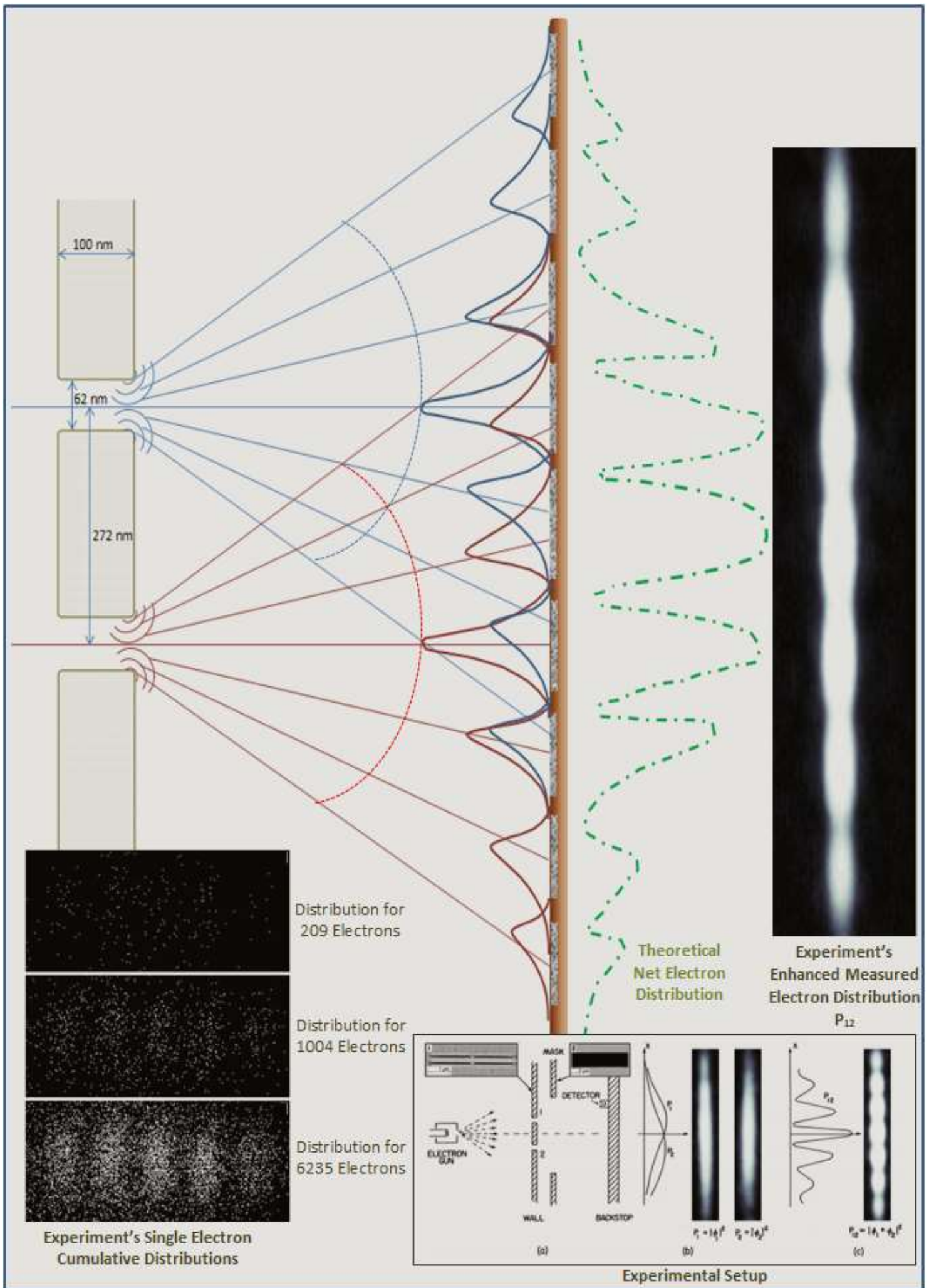P_{12}**

Experimental Setup

Figure 31: 2-Slit Electron Electromagnetic Deflection and Distribution Pattern

STEM contends that a combination of light and electrons passing through the narrow slots generate SSPs that cause a scattering of the electrons, forming a curved wavefront pattern analogous to the far-field scattering for light. Such curved wavefront patterns, which would in turn produce a series of overlapping skewed distributions of electrons striking the backstop as shown in figure 31, wherein the electron contribution from each slit is shown in blue for the upper slit and red for the other. The net distribution of electron hits is shown by the dashed green line plot: it corresponds well to the banded pattern P_{12} to the right of figure 31, and is quite similar to that of figure 30a.

The banded pattern P_{12} of figure 14 is an intensity-enhanced version of the electron distribution at the backstop. With progressive plots by single electron, there is no chance that electrons might interference with each other because, although their paths may cross, they are never in the same place at a given point in time. However, using the 6235 single electron distribution, as shown bottom left in figure 31, by projecting the hit points to a central axis and then represent the projected plot as an intensity enhanced plot, the result are almost identical to that of P_{12}, and without any possibility of constructive and destructive interference being a factor.

For the continuous streaming of electrons (as opposed to the single electron firings), It is probable that some electron pairs will deflect each other should their paths cross, but such deflection, and related electrical interference between the pair, is far removed from them destructively eliminating each other.

For light the 2-slit experiment is easily duplicated, with the banding being explained by the constructive and destructive interference of intersecting curved wavefronts of light. The story for 2-slit experiments using electrons, atoms and molecules is different: the patterns observed here represent a statistical distribution of deflected particles on the target screen or sensors. It is the author's opinion that the 2-slit experiments do not demonstrate, confirm or bestow particle-wave duality characteristics to electrons, atoms, molecules or, by logical extension, to matter, even though such wave-like characteristics can be accommodated by Dirac's wave equations. Protagonists of this approach would do well to understand that a satisfied theory equation does not equate to a satisfying practical explanation.

Optical Vortex Light

The kinetic energy of FER provide light with a minute amount of **linear momentum** (viz. **radiation pressure**). For circularly polarised light (CPL), the pair of overlapping orthogonal PPL rays phase offset by $\pi/2$ or $3\pi/2$, generate a net electric field that has the form of a single rotating helix that produces angular momentum called **spin angular momentum** (**SAM**). CPL generates sufficient SAM to cause nanoparticles to **spin** clockwise or anti-clockwise (as in figure 32a), depending upon the helicity of the CPL.

Optical Vortex Light (**OVL**) occurs when the wavefront from a collimated beam is made to follow a helical (or cylindrical-spiral) path, with the helix's central axial direction being the direction of travel of the light beam. As for CPL, OVL is chiral (i.e. can be a left-handed helix or a right-handed helix) and can develop sufficient angular momentum, called **Orbit Angular Momentum** (**OAM**), to cause nanoparticles in solution to **rotate** clockwise or anti-clockwise (as in figure 32b), depending upon the helicity of the OVL.
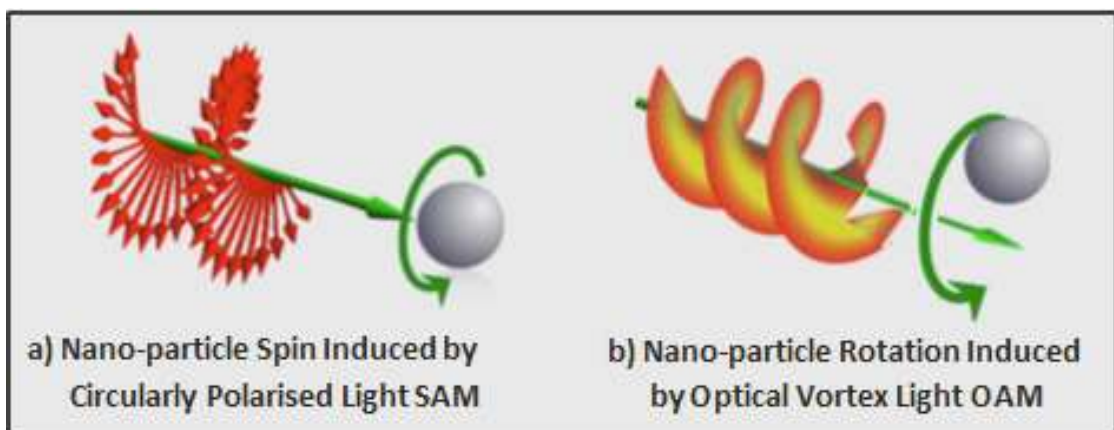

Figure 32: SAM versus OAM

OVL came into prominence with a well-received [paper by L Allen et al in 1992](#), and since 2005 there has been considerable research into OVL and its extension to other areas such as vortex electron streams and radio signal encoding. OVL can be [produced by a range of techniques](#) (3 shown in figure 33) including Spiral Phase Plates (SPP), Q-plates, pitchfork diffraction gratings (often called computer-based holograms) and cylindrical mode converters.
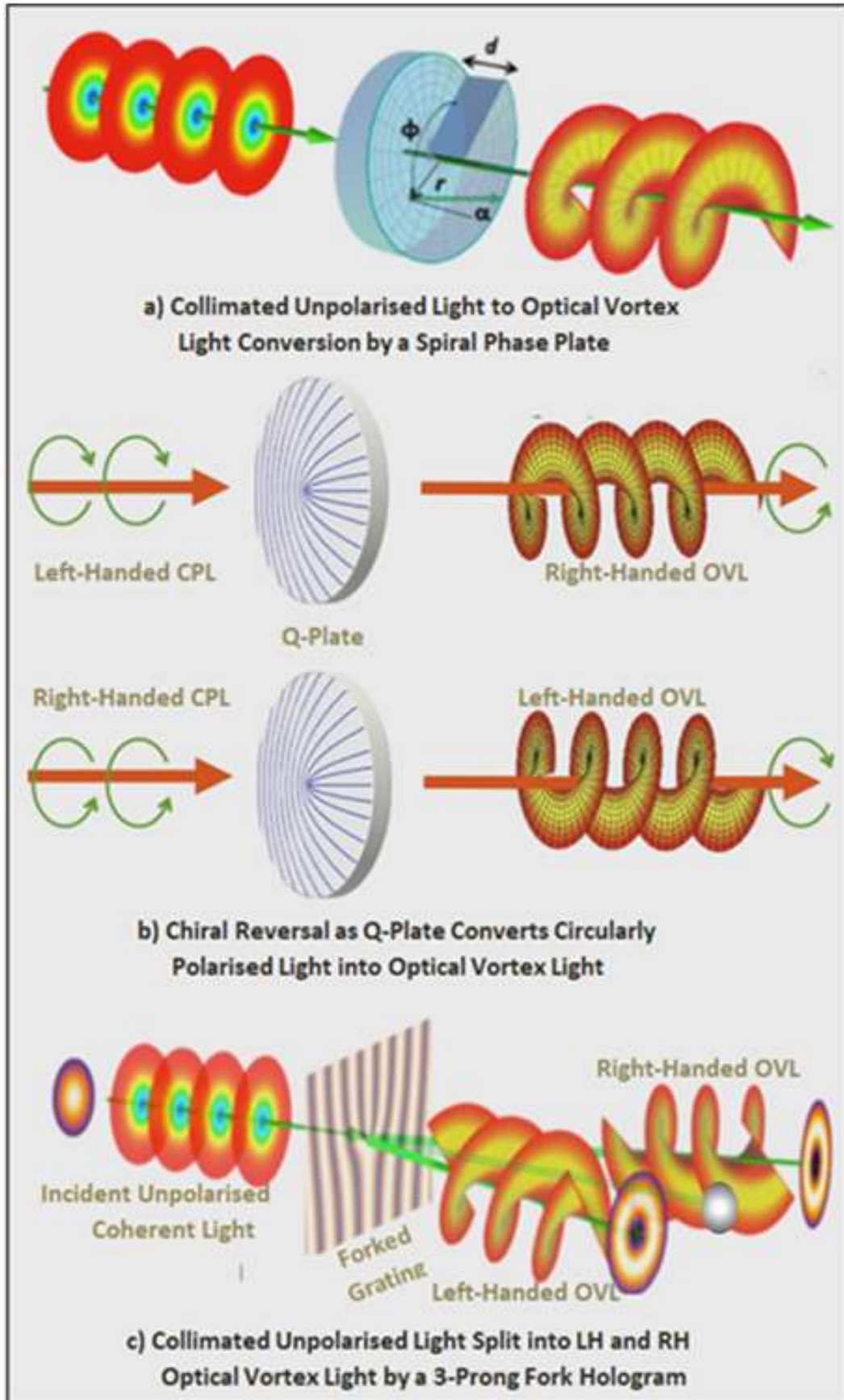

a) Collimated Unpolarised Light to Optical Vortex Light Conversion by a Spiral Phase Plate

b) Chiral Reversal as Q-Plate Converts Circularly Polarised Light into Optical Vortex Light

c) Collimated Unpolarised Light Split into LH and RH Optical Vortex Light by a 3-Prong Fork Hologram

Figure 33: Generation Techniques for Optical Vortex Light

Because of OVL's left and right-handed helical forms, diagrams such as those in figure 33 superficially appear to be similar to left and right-handed circularly polarised light (CPL). However, the single helix form of CPL's electric field is generated from the combination of a pair of orthogonal PPL rays: and it can only generate SAM. For an OVL beam, the rays are physically grouped with their phase fronts taking on a helix form that rotates or precesses to generate OAM.

A Q-plate is a **variable spiral plate** (VSP) consisting of a passive liquid crystal optical element that is capable to modify a simple laser beam or a circularly polarised light beam into a vortex beam. **Pitchfork diffraction gratings** and **spiral phase plates** are passive devices that convert unpolarised light into OVL. The simplest, and arguably the most flexible, technique for generating the various forms of OVL is a pitchfork diffraction grating containing a striated fork (a so-called pitchfork) which creates a pair of left and right-handed OVL beams.
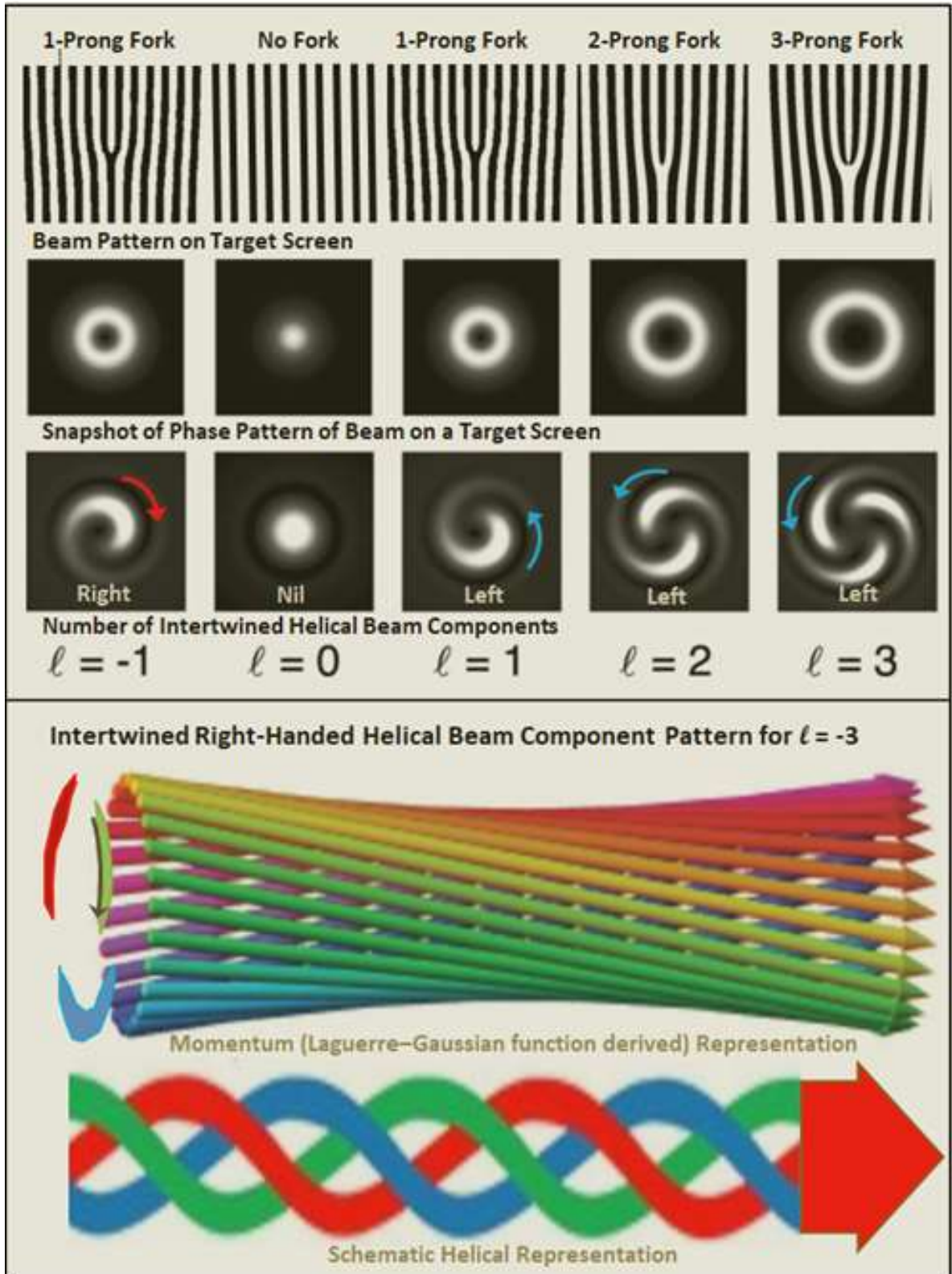

Figure 34: OVL Characteristics for Multi-Prong Fork Interference

A striated single fork (such as the 1-prong fork of figure 34) produces a pair of single-spiral helical beams, with one having right-hand chirality (ℓ = -1), and the other left-hand chirality (ℓ = +1) as in figure 34. An interesting feature of the pitchfork approach is that, should another transparent prong be added, splitting the central solid fork prong, the number of spirals within each helical beam increases by 1, as for the 1 to 3-prong forks of figure 34 and the corresponding ℓ = 1 to 3 beam patterns. More detailed 3D representations of a 3 intertwined spirals of a right-handed helical OVL beam (ℓ = -3) from a 3-prong fork are shown at the bottom of figure 34. Note that the RH OVL beam forms to the left of the fork, whereas the LH OVL beam forms to its right, as shown in figure 33c.
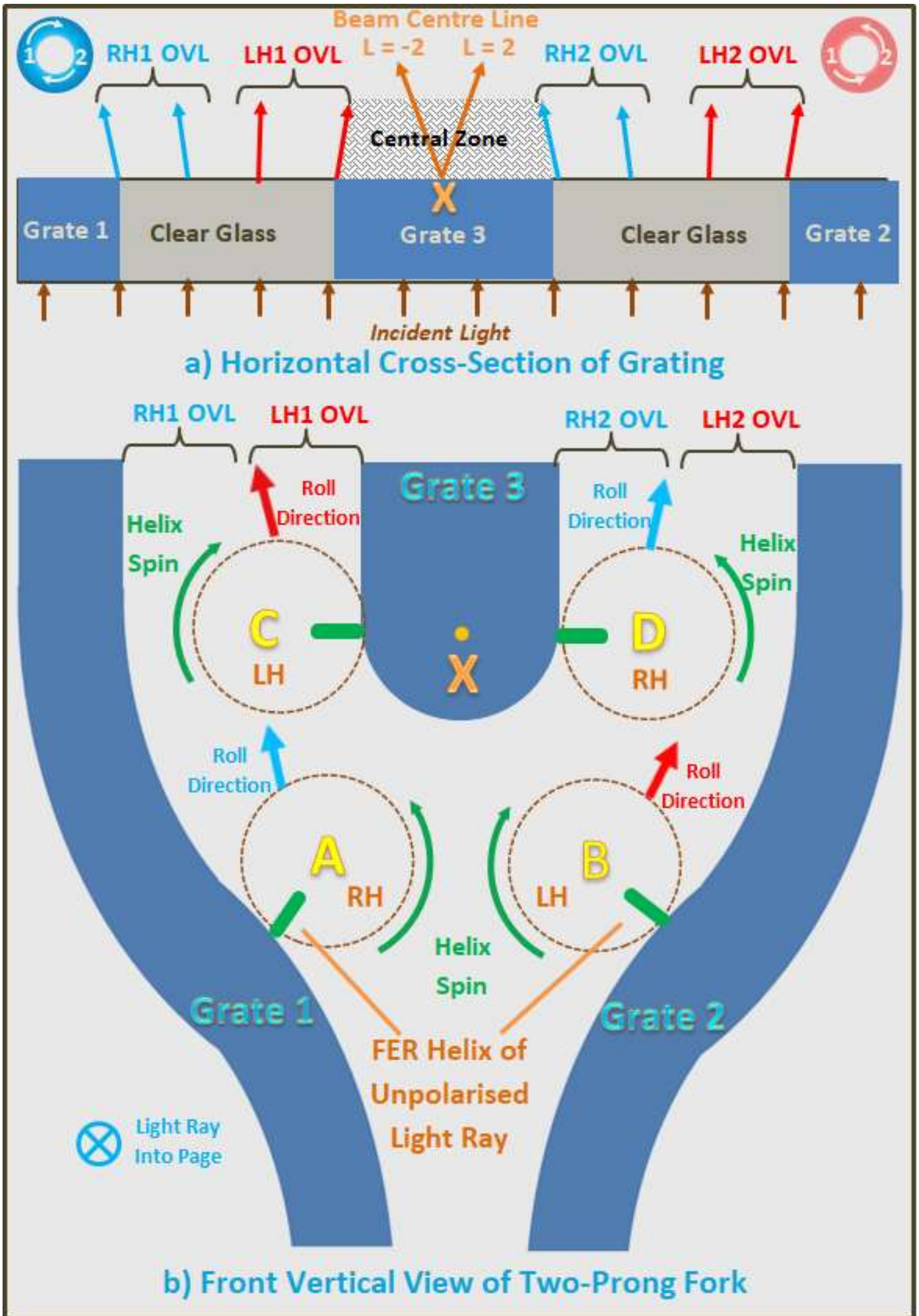
Figure 35: Left- and Right-Handed OVL Beam Generation by a Two-Prong Fork Grating

The parameter ℓ appears in the equation representing the phase of OVL, which is exp($i\ell\phi$). The absolute value of ℓ indicates the number of spirals within each helical beam and corresponds to number of prongs in a fork; it is negative for the RH OVL beam generated to the left of the fork, and positive for the LH OVL beam to the right.

Figure 35 is a stylised diagram representing a 2-prong fork, defined by grates labelled 1 to 3 of a pitchfork grating. Figure 35b shows the FER helix of four representative incident rays (A, B, C and D) of unpolarised light when viewing the grating in the direction of the incident light. Light rays A and D have left-handed chirality; and B and C have right-handed chirality. (Note that rays A, B, C and D are not related to the similarly labelled arc-zones of the incident ellipse of the Light Refraction, Reflection and Polarisation chapter).

For an incident ray that makes close contact with the grates (solid bits) in the pitchfork diffraction grating, its FER push against the grate surface with the FER arrival order causing its helix, whilst maintaining its structural integrity, to commence to rotate and roll laterally along the grate-wall. The induced helix rotation (or spin) direction corresponds to the FER arrival order at the outer surface of the diffraction grating. The result is that the right-handed helix rays commence a rolling action along and away from the grate **1** and grate **3** walls as exemplified by helix **A** and **D**. Similarly, the left-handed helix rays commence a rolling action along the grate **3** and grate **2** walls as exemplified by helix **C** and **B**.

When a light ray's helix starts to rotate and move laterally, it interferes with other rays within the beam. Should that other ray the same chirality, and the two rays are not exactly 180° out of phase with each other, then they can combine with their helices becoming entwined, and then continue to rotate as a nested pair of OVL. Should the rays be exactly be exactly 180° out of phase with each other or have opposite chirality, they push each other away with the other ray possibly being caused to start rotating in the opposite direction.

As for reflection and refraction processes, the ray entanglement processes of OVL generation are chaotic and the outcomes more statistical than prescriptive in nature. As those rays squeezed close to the fork prongs start rotating and interfering with adjacent rays, the concentration of multiply entwined helices of the same chirality occur along the fork prongs causing a split along the length of the prongs shown as the RH1 and LH1, and as RH2 and LH2 in figure 35b, and in cross-section as figure 35a.

The two main groupings exiting to the left of the 2-prong fork are RH1 and LH1 generated from rays like **A** and **C**. These entwined rays maintain their groupings after exiting but, due to their reverse rotational direction, they circle around each other in a rotational embrace evident in the $\ell=2$ phase snapshot of figure 34. The centremost rays contains a a mix of helices with left and right-handed chirality, whose electric field components cancel each other out. When projected on a screen, as shown $\ell=2$ beam pattern of figure 34 and in colour as figure 33c) the rotating groups appear as a bright annulus with a central circular black hole caused by the cancelled rays.

It is truly a remarkable order arising from chaos that produces entwined helices as shown bottom-most in figure 34 and generating momentum patterns that are well described by the Laguerre-Gaussian function.

STEM contends that FER have a similar toroidal form to electrons in that both consist of a torus of concentrated field-energy surrounded by less concentrated field-energy that provides their electromagnetic characteristics. Although FER contain significantly less field-energy, and thus a correspondingly small rest mass, it would be feasible for a beam of ray-like electrons could also be transformed into a **vortex beam of electrons**. Using a chiral plasmon (similar to Q-plate) as shown in figure 36, Vanacore et al team, in their 2019 research paper 'Ultrafast generation and control of an electron vortex beam via chiral plasmonic near fields', claim to have generated an electron equivalent to OVL.
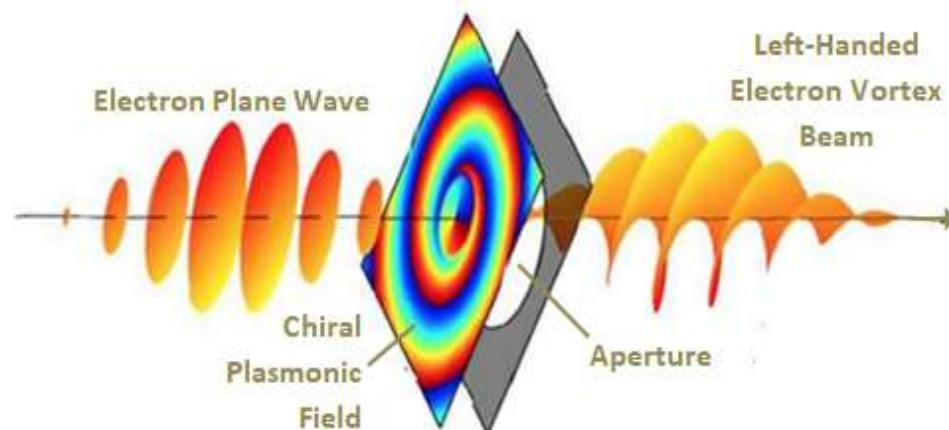

Figure 36: Electron Vortex Beam Generation

The vortex beam of electrons generated from a collimated and coherent incident electon beam has left-handed helicity, as shown in figure 36. The STEM would expect that, for a similar setup involving an aptron electron (positron) rather than a cetron electron beam, a right-handed positron vortex beam would be generated .

The Vanacore research paper is supported by the 'twisting whirlpools of electrons' video, which provides the background and supportive graphics explaining chiral electron vortex generation. The video is quite an interesting and amusing by making strange, yet appropriate, visual analogies, in a distnctly Italian-American way about vortices and a stirred cup of coffee, and between different vortex forms and various pasta styles and bagel shapes.

Optic Vortex light is hoped to lead to an increase the band width of optic fibres for data communications, and to assist with nanoparticle manipulation. In a similar vein it is hoped that vortex beams of electrons (and possibly aptrons) may lead to ultrafast electron vortex beams, with significant implications for fundamental physics, quantum computing, future data-storage, the study of chiral molecules and chiral plasmon resonances, and possibly certain specialised medical treatments.

Overview of EMR

STEM distinguishes between **photonic** and **non-photonic EMR** and contends that a monochromatic light ray of unpolarised light consists of **Field-Energy Rings** (**FER**) generated by the flip-action of cetron (or aptron) electrons relocating to other a lower-radius orbital. As an unpolarised ray of light, FER travel in a helix formation that has either left-handed or right-handed chirality, with the ray's wavelength (**λ**) being defined by the wavelength of its FER spirals, which can vary according to the FER packing density within any given transport medium.

Both CS and STEM consider that photonic EMR is generated by an orbit electron jumping from a higher to a lower energy level and, for EMR absorption, by an electron jumping from a lower to higher orbit. The main difference being that CS considers the orbits to be fixed, whereas STEM considers them to be dynamically defined and are associated with radial **tolerance limits** that produce a quantum-like effect for electron jumps between orbitals.

The other main difference is that CS considers that EMR consists of electromagnetic waveforms that, as a photon (which is itself an ill-defined concept), can behave particle-like; but struggles to explain how EMR can travel through empty Space (or a vacuum) as an EM waveform. STEM, on the other hand, contends that, due to their speed and field-energy spin and content, FER have angular and linear momentum, which explains the **particle nature** of light, and why a luminiferous aether (or Aether) is not required for light to travel for vast distances through near-to-vacuum conditions of outer Space.

As unpolarised light passes into a transparent medium with different refractive index (RI), its speed changes, and its FER packing density and wavelength adjust accordingly; however, its frequency remains unchanged. A light **beam** consists of multiple light rays with approximately equal numbers of left-handed and right-handed chiral helix rays of various frequencies, various lengths and, usually, in various phases.

A ray of unpolarised light is readily re-organised and, upon encountering a medium with a different refractive index, its helix structure can split into up to six **sub-rays** that are variously reflected and refracted. The number and composition of the sub-rays depends upon a combination of the angle of incidence and the phase of the light, that together determine the **arc-zone** location around the **incident-ellipse** at which each FER encounters the **interface plane**. Each sub-ray generated contains alternating groups of positive and negative FER with the same frequency as the incident light, and with the degree and type of polarisation being related to the FER arc-zone location within the incident-ellipse.

Plane polarised light (**PPL**) occurs when the FER within light rays are re-grouped and orientated so that their toroidal spin planes are coplanar and parallel to the light's travel direction. FER within PPL are concentrated into positive and negative groups (called **g-FER**) that define the positive and negative pulse frequency of a PPL ray. Such pulses have the same frequency as that of the unpolarised light from which it was derived. **Circularly polarised light** (**CPL**) and **Elliptical polarised light** (**EPL**) are created when two separate PPL rays, with polarisation planes that are orthogonal to each other, are merged. For same-frequency, same amplitude orthogonal PPL rays that have a π/2 phase difference,

left-handed CPL is generated; with a 3π/2 phase difference, **right-handed CPL** is generated. For all other amplitude and phase offset combinations, left-handed or right-handed EPL results.

Optical vortex light (**OVL**) is a light beam with helically rotating phase fronts which generate **orbit angular momentum** (**OAM**). OVL can be created from unpolarised or circularly polarised light using passive (e.g. a pitchfork grating) or electro-mechanical devices (e.g. a variable spiral plate). When created from unpolarised coherent light using a pitchfork grating, the curved grate of a fork grating selectively causes the helix of the incident light to rotate to create ring-like beams of OVL on each side of the fork, with right-handed chirality emerging left of the fork and left-handed to the right. The number of pitchfork prongs determines the number OVL spirals rotating in unison within each beam.

The **laws of optics** (a combination of Maxwell's equations, Snell's law, Malus' law and the Fresnel equations) allow the electromagnetic attributes and associated behaviour of light to be mathematically described and quantified. STEM, on the other hand, provides a **physical model** for light in terms of FER configurations, which generate electromagnetic fields that conform to the laws of optics, and are compatible with Maxwell's equations and the probabilistic nature of the wave equations of Quantum Mechanics.

The STEM approach to EMR provides logical feasible explanations regarding the attributes and behaviour of light, including that:

1. Light exhibits both particle and wave-like characteristics (its apparent wave-particle duality).
2. For a carrier with a different refractive index, light's wavelength and speed of change, but not its frequency.
3. For angles of incidence for which Snell's law is applicable, some light within a light beam is reflected while some is refracted.
4. The mix of s- and p-polarisation varies with the angle of incidence for transmitted and reflected light, as is indicated by the Fresnel transmittance and reflectance coefficients.
5. Only s-polarised light is reflected at **Brewster's angle** of incidence, whereas all transmitted light contains a mix of s- and p- polarised light.
6. Transmitted light's angle of refraction varies with both the angle of incidence and light frequency.
7. Left-handed CPL is created by merging a pair of orthogonal PPL rays having the same amplitude but a phase offset of π/2; and right-handed CPL is created when the phase offset is 3π/2.
8. The formation of optic vortex light from unpolarised light and CPL, and the OAM associated with OVL.

STEM provides reasonably simple Newtonian Physics explanations for light-related phenomena such as the refractive index of light passing through transparent media; plane, circular and elliptically polarised light; the chromatic dispersion of light; and exotic forms of light such as optical vortex light. And with STEM's helix structure for photonic EMR, observed particle-wave duality characteristics would be expected rather than considered to be enigmatic.